Università di Pisa

**Facoltà di Scienze Matematiche,
Fisiche e Naturali**

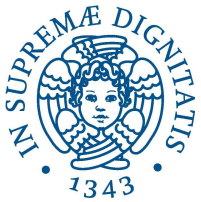

School of Graduate Studies "Galileo Galilei"

Applied Physics

Ph.D. Thesis

Relaxation, short time dynamics and elastic properties in glass-forming liquids

Candidate
Francesco Puosi

Tutor
Prof. Dino Leporini

Director of Ph.D. in Applied Physics
Prof. Francesco Pegoraro

May 2012
(SSD FIS/03)

A Silvia e Giulia

Abstract

When they are cooled or compressed, several systems such as liquids, mixtures, polymers, biomaterials, metals, and molten salts may avoid the crystallization, resulting in a metastable supercooled phase. A full understanding of the extremely complex phenomenology in supercooled liquids is still missing. First there is the issue of how crystallization can be prevented and how deeply the liquid can be supercooled. However by far the most interesting feature of supercooled liquids is the glass transition (GT): following a huge increase in the viscosity as the temperature decreases, the liquid freezes into a glass, a microscopically disordered solid-like state. Understanding the extraordinary viscous slow-down that accompanies glass formation is one of the major open challenges in condensed matter physics.

During my Ph.D. period (January 2009 - December 2011), I worked on several projects, all connected with the aim of understanding from microscopic basis the relaxation processes in glass-forming liquids. In the light of recent works, particular attention has been addressed to the connection between fast vibrational dynamics on picosecond time scales and the slow relaxation. The first part of my work has been devote to deepen some interesting aspects of this result and to discuss its implications on other aspects of the supercooled liquid phenomenology such as the diffusion and the violation of the Stokes-Einstein relation. Then I focused on the issue of the repulsive interactions controlling the static and dynamics in viscous liquids, and the related topic of the density-temperature scaling. In the last part of my research activity, investigated the elastic models of the GT, which relate the huge slowing down of glass-forming systems with the increasing solidity.

The study of supercooled liquids is approached here from a numerical point of view. Due to these huge potentialities, in the last years, computer experiments played an increasingly important role in glass transition studies. By performing Molecular Dynamics (MD) simulations, we were able to study the dynamics on the microscopic level and to collect informations on every observable of interest with quite a high level of precision, while the same process in experiments would require much more effort. MD simulations allow us to test the validity of theoretical models, as in the case of the elastic models, in a fully controlled environment. During all the study, we have maintained a close connection with the "real world", by comparing, whenever possible, MD results with experimental ones.

To study the complex glassy phenomenology, the chosen prototype of viscous liquid is the simple beads and springs model for polymeric chains. Polymers play a central role in several studies on the GT because of their natural

inclination to disorder: in most cases a polymer liquid, rather than crystallize in a regular lattice, reaches the amorphous glassy state.

As far, as the outlook of the Thesis is concerned, I have to point out that, because of the limited time of my research activity, some open questions remain, especially in the discussion of elastic models. Accordingly, further investigations, generalizations and improvements of these results could be useful.

The research activity of this Thesis has resulted in the following papers:

- ⋆ F. Puosi and D. Leporini, *Scaling between relaxation, transport, and caged dynamics in polymers: from cage restructuring to diffusion*, J. Phys. Chem. B **115** 14046-14051 (2011).
- ⋆ F. Puosi and D. Leporini, *Communication: Correlation of the instantaneous and the intermediate-time elasticity with the structural relaxation in glassforming systems*, J. Chem. Phys. **136** 041104 (2012).
  Also selected for publication on the Virtual journal of Biological Physics Research, February 1, 2012 (http://www.vjbio.org).
- ⋆ F. Puosi and D. Leporini, *Spatial displacement correlations in polymeric systems*, J. Chem. Phys. **136** 164901 (2012).
- ⋆ F. Puosi and D. Leporini, *Fast and local predictors of the violation of the Stokes-Einstein law in polymers and supercooled liquids*, submitted.
- ⋆ F. Puosi and D. Leporini, *Universal elastic and plastic effects in the particle caging of polymers and glass-forming liquids*, arXiv:1108.4629v1.

Contents

Chapter 1

Introduction

1.1 Supercooled liquids and glasses

1.1.1 Basic phenomenology

When a liquid is cooled below its melting temperature T_m a first order phase transition usually takes place and the liquid turn into a crystal. However, under certain conditions it is possible to avoid crystallization and to keep the system in a metastable phase, named the supercooled phase. Supercooled liquids have very rich phenomenology which is still far from being completely understood (see Figure 1.1). For a comprehensive discussion on this topic see refs [1–5].

In the supercooled phase typical time scales increase sharply, and they end up being larger than the experimental time at T_g, the glass transition temperature. Around the melting temperature T_m, the typical time scale τ_α on which density fluctuations relax is of the order of picosecond; at T_g the typical time scale has become of the order of $100\,s$, 14 orders of magnitude larger. This increase is even more impressive because the corresponding decrease in temperature is about $\frac{1}{3}T_m$ (T_g usually occurs around $\frac{2}{3}T_m$). The increasing of τ_α is accompanied by an increase of the shear viscosity η [1]. This can be understood if one considers a simple Maxwell model: η and τ_α are related by $\eta = G_\infty \tau_\alpha$, being G_∞ the instantaneous shear modulus, which changes little in the supercooled phase. For a glass-forming liquid the viscosity is typically of order $10^{12}\,Pa\,s$ just above the glass transition (GT). To understand how large this value is, recall that at the melting point a liquid's viscosity seldom exceeds $\eta \sim 10^{-3} - 10^{-2}\,Pa\,s$. A system with $\eta \sim 10^{12}\,Pa\,s$ appears mechanically solid (on the experimental time scale, as solidity is a time-scale-dependent notion [6]), but it is still a liquid as it lacks long-range order. Such a system is called

[1] The viscosity is generally defined via shear flow. Consider a liquid placed between two parallel solid plates of area A. Assuming that the plates are very large such that edge effects may be ignored, and that the lower plate is fixed, let a force F be applied to the upper plate that causes the liquid to undergo shear flow with a velocity gradient u/y. The applied force is proportional to the area and velocity gradient in the fluid $F = \eta A \frac{u}{y}$ where the proportionality factor η is given by the shear viscosity.

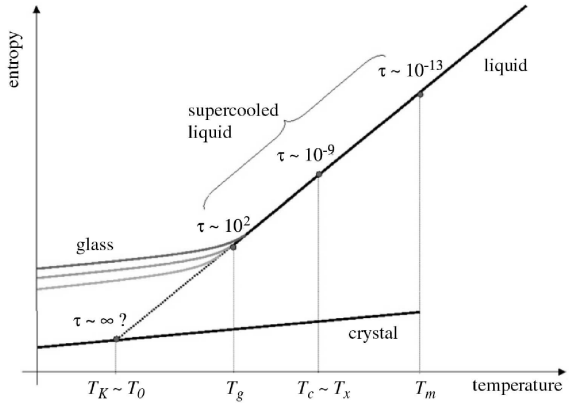

Figure 1.1: Schematic representation of the entropy versus the temperature in a liquid, from the high-T phase, down to the deeply supercooled phase. Relevant temperatures are marked: T_m is the melting temperature, at which a first-order phase transition between liquid and crystal occurs; T_c is the temperature where the mode coupling theory locate a dynamic transition; T_x is Goldstein's crossover temperature from a high-T non-activated dynamics to a low-T activated one; T_g is the dynamic glass transition temperature, where the relaxation time exceeds the experimental time $10^2\,s$; the longer the available experimental time, the lower the temperature where the system falls out of equilibrium forming a glass (different line); T_k is the Kauzmann's entropy crisis temperature, where the extrapolated liquid entropy equals the crystal entropy and where, according to some theories, there is a thermodynamic phase transition; T_0 is the temperature where the Vogel-Fulcher-Tamman fit locates a divergence of the relaxation time. Above each temperature we report the approximate value of the relaxation time in seconds. (Reprinted from [5])

glass.

The glass transition temperature T_g marks the point at which the relaxation time of the liquid τ_R exceeds the available experimental time t_{exp}: $\tau_R(T < T_g) > t_{exp}$. This looks as an odd definition for a "transition": by the fact T_g depends on the experimental protocol and in particular on the cooling rate and experimental time. However, in many systems the value T_g does not depend strongly on the experimental time: the increase in the relaxation time is so sharp (at least exponential) to make it very hard to move significantly the position of T_g even by a substantial change in the cooling rate. For this reason, it is sensible to define T_g as the temperature at which the relaxation time is equal to $10^2\,s$. By using the Maxwell relation, this is equivalent to define T_g via the following classic relation $\eta(T_g) = 10^{12}\,Pa\,s$.

The most important effect of going off-equilibrium is the loss of ergodicity as the system does not have enough time to properly explore the phase space and remains trapped in one local energy minimum . This results in a reduction of the number of degrees of freedom accessible to the system and a consequent drop in the constant pressure specific heat at T_g to a value very close to that of the crystalline phase [1] (both the crystal and the glass are non-ergodic states, but, while the crystal is in a thermodynamic equilibrium state, the glass is

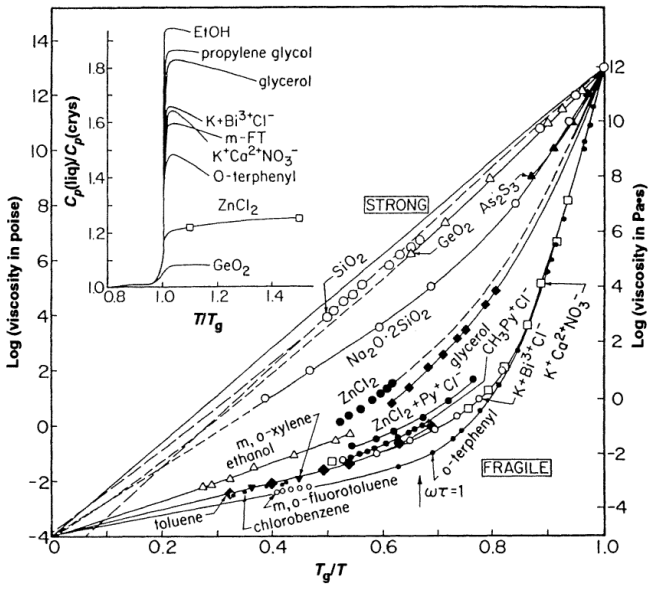

Figure 1.2: The Angell plot showing the viscosity as a function of inverse temperature normalized at T_g for different substances. An Arrhenius behavior gives a straight line in this plot. This is typical of strong glass-formers. Super-Arrhenius increase of η corresponds to fragile glass-formers. If one define the apparent activation energy as $E = d\ln(\eta)/d(1/T)$, than in strong liquids the activation energy is independent of T, while it increases when T decreases for fragile liquids. Inset shows the changes in the heat capacity across the glass transition for several liquids. (Reprinted from [9])

not).

The ability to form glasses is a universal properties: once the highly viscous liquid state is reached, glass formation is unavoidable upon continued cooling. In many cases a rapid cooling is necessary to avoid crystallization (cooling rate $\sim 10^6\, K/s$ in the case of metallic glasses). A good glass former is a liquid which is easily supercooled, i.e., characterized by very low rates of crystal nucleation and growth at all temperatures [7]. Good glass formers are organic and ionic liquids, silicates, polymers and also some metallic glasses [4].

1.1.2 Fragile and strong liquids

The increase of the viscosity in supercooled liquids is remarkable not only because of its magnitude but also because of its temperature dependence. Figure 1.2 shows a T_g-scaled Arrhenius plot of liquid viscosities called Angell plot [8]. This plot is useful in classifying supercooled liquids. If dynamics are dominated by barriers to be overcome by thermal fluctuations, one expects an Arrhenius behavior $\eta \sim \exp(\Delta E/k_B T)$, resulting in a straight line in the plot. On the contrary, some systems show a stronger than Arrhenius increase of the viscosity upon cooling toward the glass transition. Such super-Arrhenius liquids are called "fragile", while those close to Arrhenius behavior are termed

"strong" [8]. Silica (SiO_2) is the prototypical strong liquid whereas o-terphenyl (OTP) and toluene are the canonical fragile glass-formers. The terminology strong and fragile is not related to the mechanical properties of the glass but was introduced in relation to the evolution of the short-range order close to T_g. Strong liquids, like SiO_2, typically have a locally tetrahedric structure which persist both below and above the glass transition, in contrast to fragile liquids. The structural stability is reflected in the small heat capacity and thermal expansion coefficient changes across the glass transition in strong liquids with respect to fragile liquids (see inset of Figure 1.2).

Non-Arrhenius data are often fitted by the so-called Vogel-Fulcher-Tammann (VFT) expression $\tau = \tau_0 \exp(\frac{A}{T-T_0})$ which suggests a divergence of the relaxation time at a finite temperature T_0, a prediction that cannot be verified because the system is supposed to fall out of equilibrium as T_0 is approached. Note that there are other comparably good fits of these curves [10–12].

1.2 Computer simulation of liquids

Numerical simulations are a powerful tool for studying liquids and supercooled liquids at a microscopic level (see [13–16] for extensive treatments on this subject). The most outstanding advantage of simulations is that they provide an extremely large degree of freedom regarding the systems that can be studied. In principle, any Hamiltonian that is of interest can be investigated. By selecting an appropriate Hamiltonian, it is possible to study molecules or polymers with an exactly specified shape and size [17–19], to investigate the system in thermodynamic states which are difficult to realize experimentally - such as under negative pressures [20, 21] or to study the dependence of the structure and the dynamics of a system in a small pore of a well-defined size and shape [22]. An important role is played by simulations, also because a large variety of dynamic and static quantities can be simultaneously measured in a single model system. A large number of different theoretical approaches exist to describe the physics of glass formers and all of them have their own set of predictions that can be readily tested by numerical work. For example a large number of papers have been dedicated to testing the predictions formulated by the mode-coupling theory of the glass transition [23].

In numerical simulations the trajectory of each particle in the system can be followed at all times. This allow to easily analyze single-particle dynamics, as shown in Figure 1.3, where the mean squared displacement $\langle r^2(t)\rangle = \langle 1/N \sum_i |\mathbf{r}_i(t) - \mathbf{r}_i(0)|^2\rangle$ of a glass-forming liquids is shown. The main observation from Figure 1.3 is that single-particle dynamics considerably slow down when the temperature is decreased. Additionally, a rich dynamics is apparent, with the presence of several different regime corresponding, in order to ballistic, cage, Rouse and diffusive regime (all these behavior are discussed in details in the following chapter).

At the present time, it is possible to follow the dynamics of a simple glass-forming liquids over more than eight decades of time and over a temperature window in which average relaxation time scales increase by more than five decades. Even if at the lowest temperatures considered in numerical simula-

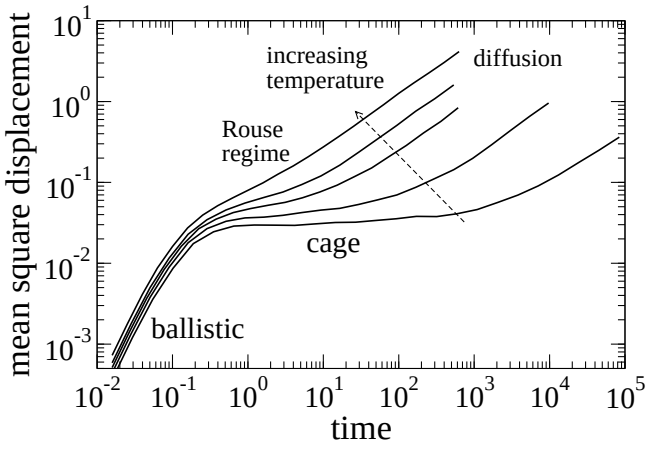

Figure 1.3: Mean square displacement in a simple model of a glass-forming liquid composed of fully flexible linear chains interacting with a Lennard-Jones potential. When temperature decreases, the monomers displacements become increasingly slow and some distinct regimes become apparent.

tions, the relaxation time scales are orders of magnitude faster than in experiment performed close to T_g, many features associated with the glass transition physics can be observed such as strong decoupling phenomena and crossovers toward activated dynamics.

Classical computer simulations of supercooled liquids proceed by numerically solving a discretized version of Hamilton's equation for the particles' positions and momenta and a given interaction potential [13, 14]. Equations of motion are energy conserving, they describe the dynamics of the system in the micro-canonical ensemble. Constant temperature and constant pressure schemes exist which allow to perform simulations in any desired statistical ensemble. Newtonian dynamics is mainly used in numerical work on supercooled liquids. Alternative dynamics, that are not deterministic or that do not conserve the energy, can be considered. It is the case of colloids where particles undergo Brownian motion due to collisions with molecules in the solvent, and then a stochastic dynamics is more appropriate.

Simulations can be directly compared to experiments, by computing quantities that are experimentally accessible such as the intermediate scattering function or the static structure factor or thermodynamic quantities such as specific heat or configurational entropy. In this perspective, the model must be carefully chosen in order to be able to qualitatively reproduce the phenomenology of real glass formers, while being considerably simpler to study. A common and strong hypothesis is that molecular and chemical details are not relevant to explain the behavior of supercooled liquids. A considerable amount of work has therefore been dedicated to study Lennard-Jones model, soft or hard spheres. If the system is too simple, the glass transition cannot be studied because crystallization occurs when the temperature is lowered. Some frustration must be introduced: common solution is to use mixtures of

different atoms [24] or systems with connectivity [18]. It should be noted that whether or not a model is realistic depends on the properties one is interested in. For example, there exist many different model os silica, many of which can be considered structurally equivalent as they give a quite realistic representation of the structure of amorphous SiO_2. If, however, dynamics is considered, the various model leads to very different prediction.

1.3 Motivations and outline of the thesis

In this paragraph we briefly introduce the research context and the related open problems that motivated the work of this thesis.

Understanding the extraordinary viscous slow-down that accompanies glass formation is one of the major open challenges in condensed matter physics. On approaching the glass transition (GT) the microscopic kinetic unit spends increasing time rattling in the cage of the first neighbors, whereas its average escape time, the structural relaxation time τ_α increases from a few picoseconds up to thousands of seconds. Due to the extreme time-scale separation between rattling ($\sim 10^{-12}\,s$) and relaxation ($\sim 10^{2}\,s$ at GT), it is natural to think that this two motions are completely independent. Nonetheless, several authors investigated their correlations (for a review see ref. [4]). In this framework, an interesting advance is represented by the universal scaling between fast dynamics on the picosecond time scale and the structural relaxation which was reported for several numerical models and was seen to fit with the existing experimental data from supercooled liquids, polymers and metallic glasses over about eighteen decades of relaxation times and a very wide range of fragilities [25, 26]. The main purpose of this thesis is to achieve a deeper understanding of the connection between fast dynamics and slow relaxation.

New aspect of the scaling between fast dynamics and relaxation are discussed in Chapter 2. The robustness of the scaling is discussed, namely the fact that it does not depend on the quantities characterizing the fast dynamics and the relaxation. The scaling is then extended in the diffusive regime of the polymer chain, as in the case of binary mixtures, after that the chain length effects are appropriately treated. In this framework, the violation of the Stokes-Einstein (SE) relation and dynamic heterogeneity (DH) are investigated. It is shown that the SE breakdown, as well as the onset of DH, is signaled in a precise way by the monomer picosecond displacement.

In Chapter 3 the search for a purely repulsive reference for the Lennard-Jones potential is shown in a linear polymer model. This is motivated by the famous Weeks-Chandler-Andersen (WCA) picture of dense liquids in which the harsh repulsion between molecule mainly determine the structure of the liquid. To the best of our knowledge, at present time, this scheme has been applied only to atomic liquids while a discussion in molecular system is missing. This study, in particular how dynamics is affected by the range of the interaction potential, is even more useful in the light of the finding that the dynamics is well described in terms of single-particle quantity, the picosecond mean square displacement $\langle u^2 \rangle$ [25], with a local character (see the discussion of displacement-displacement correlations in Chapter 2).

In the last few years an increasing interest has been devoted to the so called "thermodynamic scaling" (or "density scaling"), namely the possibility to express dynamical quantity, like the relaxation time or the diffusion coefficient, as a function of an appropriate combination of temperature and density (for a review see ref. [27]). This topic is discussed in Chapter 4 for a model of fully flexible linear chains. It is shown that picosecond MSD $\langle u^2 \rangle$ obeys thermodynamic scaling with the same scaling exponent of the relaxation dynamics. The fact that thermodynamic scaling roots in the picosecond dynamics represents a connection of this topic with the scaling between fast dynamics and relaxation, suggesting that both are different aspects of a more fundamental phenomenon.

Then, the issue of how dynamics is determined by a quantity that can be measured at very short time is approached from a different perspective. In Chapter 5 we present a MD simulation study of the elastic models for the glass transition which relate the increasing solidity of the glass forming systems with the huge slowing down of the structural relaxation and the viscous flow (see ref. [4]). A well-defined scaling is evidenced by considering the elastic response observed at intermediate times after the initial fast stress relaxation. It is shown that an extended version of the standard elastic models, accounting for heterogeneity, is able to reproduce the simulation results. The proposed master curve is compared with the available experimental data on several different systems, resulting in a good agreement.

Chapter 2

Scaling between caged dynamics and diffusion in polymers

2.1 The research context

2.1.1 Polymers

Polymers [28, 29] are macromolecules characterized by the repetition of one or more species of atoms or groups of atoms, constitutional repeating units named monomers, linked each other by covalent bonds. Polymeric materials are ubiquitous and, in some cases, essential for everyday life. Their presence extends from familiar synthetic plastics and elastomers to natural biopolymers such as nucleic acid and proteins. One reason for the abundance of applications of polymeric materials is the diversity in the chemical structure and composition ranging from simple linear homopolymers to branched polymers, hyper-branched polymers, stars, H-shaped polymers and copolymers which have random or block sequences (see Figure 2.1).

Polymer physics is the field of physics, born in 1930s, that deal with structure, dynamics and mechanical properties of polymers [28, 30, 31]. Being very large molecules, polymers are very complicated for solving using a deterministic method. So, statistical approaches, based on an analogy between a polymer and either a Brownian motion or other type of random walk, are often used.

In the following, we will be concerned with the simplest and most common polymer chemical structure, namely linear polymers, in a molten phase. In a melt monomers pack densely, leading to an amorphous short range order and to an overall low compressibility of the melt. Both features are characteristic of the liquid state. Qualitatively, the collective structure of the melt thus agrees with that of non-polymeric liquids [18] (simple and molecular liquids). On the length scale of a chain, however, additional features appear. The structure of a polymer chain in a dense melt is that of a random walk, with

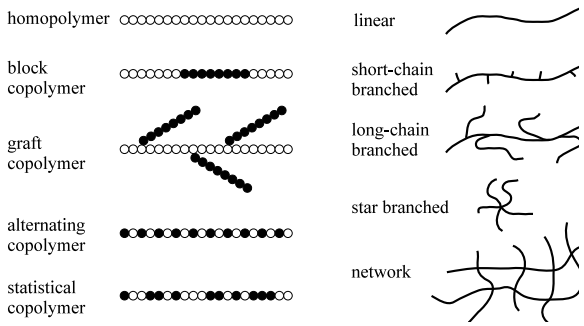

Figure 2.1: Left: homopolymers and different classes of copolymers (unit A (○) and B (●)). Right: schematic representation of structures of polymers with different molecular architecture.

a statistical segment length controlled by the detailed chemistry of the chain. However, chemical detail does not affect many static and dynamic properties of chains which exhibit universal features, controlled by the connectivity [31]. If we denote the chain length by N, the size of the random coil structure scales as $R_g \propto \sqrt{N}$, where R_g is the radius of gyration of the chain. On average, a polymer experiences $\sqrt{N}$ intermolecular contacts with other chains, a huge number in the large N limit. This might explain why the single chain dynamics in dense melts is usually described by an effective medium type approximation. It is the case of the Rouse model [32] (see Appendix B), which describes the dynamics of sufficiently short chains, where entanglement effects are not present.

Polymers are good glass formers, with a few notable exceptions [2]. For some polymers, such as atactic homopolymers or random copolymers, no possible crystalline state is known at all. Even when an ordered ground state (crystalline or liquid crystalline) is possible, ordering is kinetically hindered. In order to crystallize, due to packing constraints, a chain have to change its conformation from a random-coil one to an ordered one, in a synchronized fashion with the surrounding chains. At low temperature such kind of motions are strongly inhibited, and a crystalline phase is difficult to be obtained.

2.1.2 Scaling between caged dynamics and relaxation

Understanding the extraordinary viscous slow-down that accompanies glass formation is a major scientific challenge [3, 8, 9]. On approaching the glass transition (GT) trapping effects are more and more prominent. The average escape time from the cage of the first neighbors, i.e., the structural relaxation time τ_α, increases from a few picoseconds up to thousands of seconds. The rattling motion inside the cage occurs on picosecond time scales with amplitude $\langle u^2 \rangle^{1/2}$. This quantity is related to the Debye-Waller factor which, assuming harmonicity of thermal motion, takes the form $\exp\left(-q^2 \langle u^2 \rangle / 3\right)$ where q is the absolute value of the scattering vector. At first sight, due to extreme time scale

separation between the rattling motion ($\sim 10^{-12}s$) and the relaxation ($\sim 10^{2}s$ at GT), one expects the complete independence of the two motions.

A firm basis to connect fast and slow degrees of freedom was developed by Hall and Wolynes [33], who assuming that atomic motion is restricted to cells, pictured the GT as a freezing in an aperiodic crystal structure (ACS) modeled by the density functional theory. As a result, the viscous flow is described in terms of activated jumps over energy barriers $\Delta E \propto k_B T a^2/\langle u^2\rangle$, where a is the displacement to reach the transition state and k_B the Boltzmann constant. The usual rate theory leads to Hall-Wolynes equation (HW):

$$\tau^{(HW)}, \eta^{(HW)} \propto \exp\left(\frac{a^2}{2\langle u^2\rangle}\right) \tag{2.1}$$

The ACS model is expected to fail when τ_α becomes comparable to the typical rattling times of each atom in the cage, corresponding to picosecond time scales.

Several test of the HW equation have been carried out (for a review see [4]). However, either the crystal or the glass contributions after extrapolation in the liquid regime are usually subtracted from $\langle u^2\rangle$. In selenium, the curve log η versus $1/\langle u^2\rangle$ is concave, whereas if the glass or the crystal contribution is removed a convex curve or a straight line, the latter agreeing with the HW equation, is seen, respectively [34]. The fact that many glass-formers have no underlying crystalline phases, as well as the fact that in many studies removing the glass contribution, unlike selenium, leads to the HW equation, raises some ambiguities about the above subtractions.

Other studies noted a relation between the fast vibrational dynamics and the long-time relaxation both far [35, 36] and close to the glass transition[7, 9, 37–39]. With a distinct approach further studies established correlations between the vibrational dynamics and the relaxation close to the glass transition, as quantified by the fragility [40–44], a steepness index of how fast η or τ_α increase close to T_g, but with controversies [45].

In a recent paper Larini et al. [25] reported extensive molecular-dynamics (MD) simulations evidencing the universal scaling between the structural relaxation time and $\langle u^2\rangle$. The findings shows that trapping in space (small $\langle u^2\rangle$), resulting in localized fast dynamics, correlates with the slow dynamics (long τ_α). The master curve revealed by MD simulations is a generalization of HW equation, eq 2.1:

$$\tau_\alpha = \tau_0 \exp\left(\frac{\overline{a^2}}{2\langle u^2\rangle} + \frac{\sigma^2_{a^2}}{8\langle u^2\rangle^2}\right) \tag{2.2}$$

where $\overline{a^2}$ and $\sigma^2_{a^2}$ are the average and the variance of the truncated Gaussian distribution of the square displacements to overcome the energy barriers, respectively. Equation 2.2, when considered in terms of reduced $\langle u^2\rangle$, was initially seen to fit with the existing experimental data from supercooled liquids, polymers and metallic glasses over about eighteen decades of relaxation times and very wide range o fragilities (see Figure 2.2). Later, the scaling was evidenced in experiments on ionic liquids [46], as well as simulations of atomic liquids [26] and colloidal gels [47], the latter being very diluted systems. More

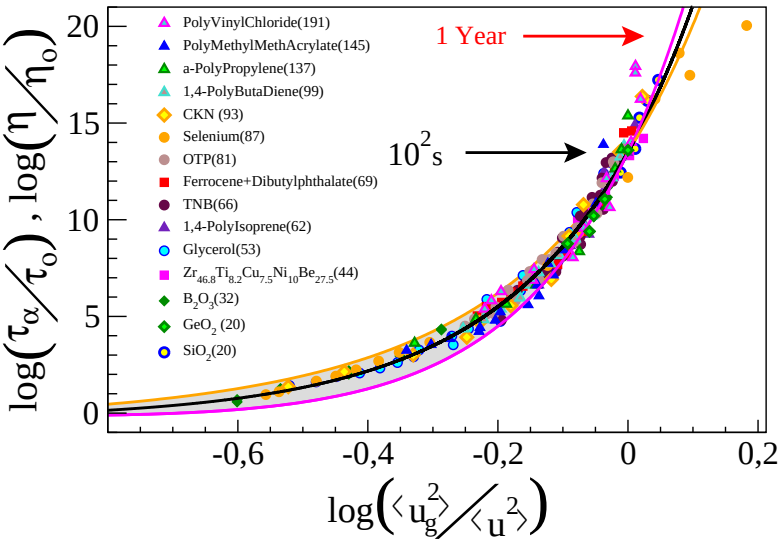

Figure 2.2: Reduced relaxation time and viscosity versus reduced cage-rattling amplitude ($\langle u_g^2 \rangle = \langle u^2(T_g) \rangle$). The numbers in parenthesis denote the fragility m. The black curve is a parabolic law. The colored curves bound the accuracy of the scaling [26]. Adapted from [48] where details about the experiments are given.

recently, the influence of free volume and the proper time scales to observe the genuine fast dynamics have been considered [46, 48].

2.2 The numerical model

A coarse-grained model of a melt of linear, fully flexible, unentangled polymer chains with M monomers each is used. The system has $N = 2000$ monomers in all cases, but $M = 3$, where $N = 2001$. Nonbonded monomers interact via a truncated parametric potential, whose attractive and repulsive steepness can be modulated. Bonded monomers interact with a potential that is the sum of the finitely extendible nonlinear elastic (FENE) potential and the Lennard-Jones (LJ) potential, resulting in a fluctuation of a few percent in the bond length.

All the polymer data are in reduced units: length in units of σ, temperature in units of ϵ/k_B and time in units of $\sigma(\mu/\epsilon)^{1/2}$, where σ and ϵ are given by nonbonding potential and μ is the monomer mass. We set $\mu = k_B = 1$.

States with different values of the temperature T, the density ρ, the chain length M, and the steepness p, q of the monomer-monomer interaction potential are studied. Each state is labelled by the multiplet $\{M, \rho, T, p, q\}$.

Full details about the model, the considered states and the simulation technique are given in Appendix A.

2.3 Results and discussion

2.3.1 General aspect of the scaling

First the monomer dynamics is presented. To this aim, the mean square displacement (MSD) $\langle r^2(t)\rangle$ is defined as:

$$\langle r^2(t)\rangle = \frac{1}{N}\sum_i^N \langle \|\mathbf{r}_i(t) - \mathbf{r}_i(0)\|^2\rangle \tag{2.3}$$

where $\mathbf{r}_i(t)$ is the position of the i-th monomer at time t. In addition to MSD the self part of the intermediate scattering function (ISF) is considered:

$$F_s(q_{max}) = \frac{1}{N}\langle \sum_i^N \exp\{i\mathbf{q}[\mathbf{r}_i(t) - \mathbf{r}_i(0)]\}\rangle \tag{2.4}$$

ISF was evaluated at $q = q_{max}$, the maximum of the static structure factor (for the polymer system $7.13 \leqslant q_{max} \leqslant 7.55$).

Figure 2.3 shows typical MSD and ISF curves of the polymer monomers.

At very short times (ballistic regime) MSD increases according to $\langle r^2(t)\rangle \cong (3k_BT/m)t^2$ and ISF starts to decay. The repeated collisions with the other monomers slow the displacement of the tagged one, as evinced by the knee of MSD at $t \sim \sqrt{12}/\Omega_0 \sim 0.17$, where Ω_0 is an effective collision frequency, i.e., it is the mean small-oscillation frequency of the monomer in the potential well produced by the surrounding ones kept at their equilibrium positions [49]. At later times a quasi-plateau region, also found in ISF, occurs when the temperature is lowered and/or the density increased. This signals the increased caging of the particle. The latter is released after an average time τ_α, defined by the relation $F_s(q_{max}, \tau_\alpha) = e^{-1}$ (for future purposes one also defines the quantity $\tau_\alpha^{(0.1)}$ via the relation $F_s(q_{max}, \tau_\alpha^{(0.1)}) = 0.1$). For $t \gtrsim \tau_\alpha$ MSD increases more steeply. The monomers of short chains ($M \lesssim 3$) undergo diffusive motion, $\langle r^2(t)\rangle = 6Dt$ with D the chain diffusion coefficient. For longer chains, owing to the increased connectivity, the onset of the diffusion is preceded by a sub diffusive region ($\langle r^2(t)\rangle \propto t^\delta$ with $\delta < 1$, Rouse regime) [28].

The monomer dynamics depends in a complex way on the state parameters. Nonetheless, if two states (labelled by multiplets $\{M, \rho, T, p, q\}$) have equal relaxation time τ_α, the corresponding MSD and ISF curves coincide from times fairly longer than τ_α down to the crossover to the ballistic regime (picosecond timescale) and even at shorter times if the states have equal temperatures. Examples are shown in Figure 2.3. The finding evidences a clear correlation between the caged dynamics and the relaxation behavior. Figure 2.3 shows that MSD of states with equal τ_α does not collapse for times $t \gg \tau_\alpha$. This is due to the onset of the polymer connectivity effects and the subsequent dependence of the monomer dynamics on the chain length M [28].

In order to characterize the cage fast dynamics of a given state we consider MSD evaluated at a characteristic time scale $t^\star$ of the rattling motion inside the cage defined by the condition that the log-log derivative $\partial \log\langle r^2(t)\rangle / \partial \log t|_{t=t^\star}$

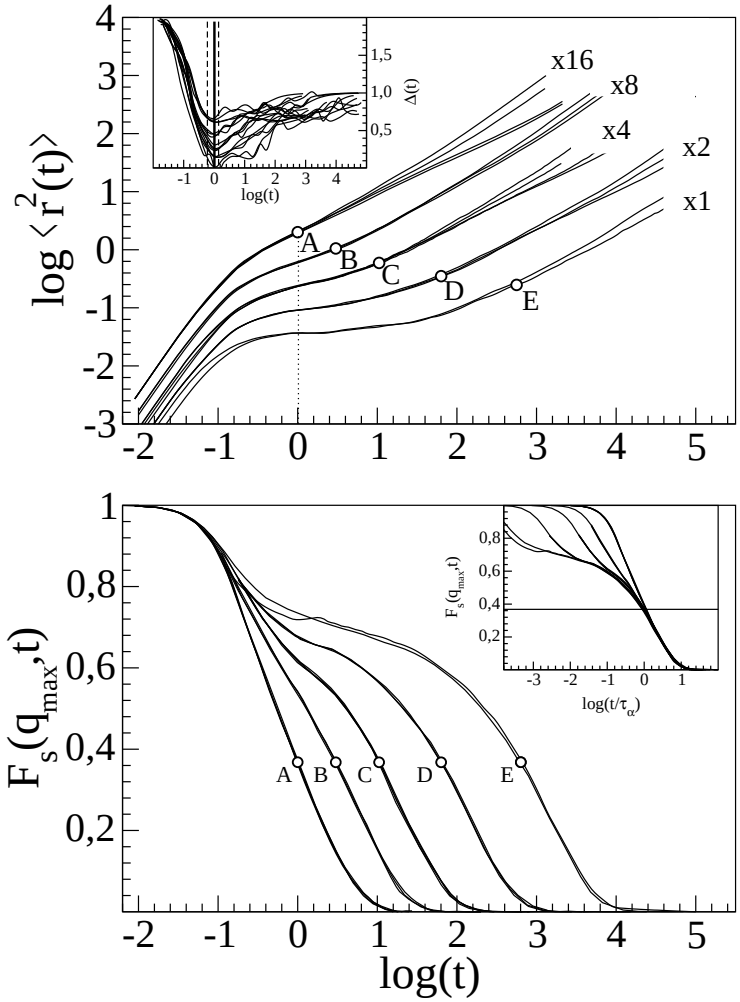

Figure 2.3: Top: monomer MSD in selected states (M, ρ, T, p, q): set A [(2, 1.086, 0.7, 7, 6), (3, 1.086, 0.7, 7, 6), (10, 1.086, 0.7, 7, 6), (2, 1.033, 0.7, 8, 6)]; set B [(2, 1.033, 0.7, 10, 6), (3, 1.039, 0.7, 11, 6), (3, 1.041, 0.7, 11, 6)]; set C [(2, 1.033, 0.5, 10, 6), (3, 1.056, 0.7, 12, 6), (5, 1.033, 0.6, 12, 6), (10, 1.056, 0.7, 12, 6)]; set D [(3, 1.086, 0.7, 12, 6), (5, 1.086, 0.7, 12, 6), (10, 1.086, 0.7, 12, 6)] set E [(2, 1.0, 0.7, 12, 11), (3, 1.1, 1.1, 15, 7)]. The MSDs are multiplied by indicated factors. Inset: corresponding MSD slope $\Delta(t)$; the uncertainty range on the position of the minimum at $t^* = 1.0(4)$ (full line) is bounded by the vertical dashed lines. Bottom: corresponding ISF. Inset: superposition of the ISF curves. The sets of clustered curves A-E show that, if states have equal τ_α (marked with dots on each curves), the MSD and ISF curves coincide from times fairly longer than τ_α down to the crossover to the ballistic regime at least.

is minimum [25, 26]. In the top inset of Figure 2.3 we see that $t^* \simeq 1$ in MD units with no appreciable dependence on τ_α. One defines the short-time MSD (ST-MSD) as:

$$\langle u^2 \rangle \equiv \langle r^2(t = t^\star) \rangle \tag{2.5}$$

This quantity is related to the Debye-Waller factor which, assuming harmonicity of thermal motion, takes the form $\exp\left(-q^2\langle u^2\rangle/3\right)$ where q is the absolute value of the scattering vector. For the present polymer model the structural relaxation time and the ST-MSD collapse on the master curve [25, 26]:

$$\log \tau_\alpha = \alpha + \beta\langle u^2\rangle^{-1} + \gamma\langle u^2\rangle^{-2} \tag{2.6}$$

The best fit of eq 2.6 to all investigated states of the present model yields $\alpha = -0.424(1), \beta = 2.7(1)\cdot 10^{-2}, \gamma = 3.41(3)\cdot 10^{-3}$.

The scaling between the cage dynamics and the structural relaxation is strong, being largely independent of the physical quantities characterizing the fast dynamics and the structural relaxation. In Figure 2.4 the scaling is built by using the two pairs $(\tau^(0.1), \langle u^2\rangle)$ (top panel) and $(\tau_\alpha, \langle r^2(t = 10\cdot t^*)\rangle)$ (bottom panel). For comparison, the original scaling $\log\tau_\alpha$ versus $\langle u^2\rangle^{-1}$ is shown in Figure 2.4 (filled symbols). Two remarks about the robustness of the scaling are in order:

(i) As shown in the bottom inset of Figure 2.3, the polymer model fulfills the time-temperature superposition principles at long times. This readily explains why $\tau^{(0.1)}$ and τ_α are fully equivalent.

(ii) Even if the present model shows that ST-MSD evaluated at both t^* and $10\cdot t^*$ does result in the effective collapse of the data (Figure 2.3 bottom), in actual experimental cases, the evaluation of ST-MSD at too long times may be dangerous in that spurious relaxation effects may come into play [46, 48].

2.3.2 van Hove analysis

The central quantity of the analysis is the self part of the van Hove function $G_s(\mathbf{r}, t)$:

$$G_s(\mathbf{r}, t) = \frac{1}{N}\left\langle \sum_{i=1}^{N} \delta[\mathbf{r} + \mathbf{r}_i(0) - \mathbf{r}_i(t)] \right\rangle \tag{2.7}$$

where $\mathbf{r}_i(t)$ is the position of the ith monomer at time t. In isotropic liquids, the van Hove function depends on the modulus r of $\mathbf{r}$. The interpretation of $G_s(r, t)$ is direct. The product $G_s(r, t)\cdot 4\pi r^2$ is the probability that the monomer is at a distance between r and $r + dr$ from the initial position after a time t. If the monomer displacement is a Gaussian random variable, $G_s(r, t)$ reduces to the Gaussian form [50]:

$$G_s(r, t) = \left(\frac{3}{2\pi\langle r^2(t)\rangle}\right)^{3/2} \exp\left(-\frac{3r^2}{2\langle r^2(t)\rangle}\right) \tag{2.8}$$

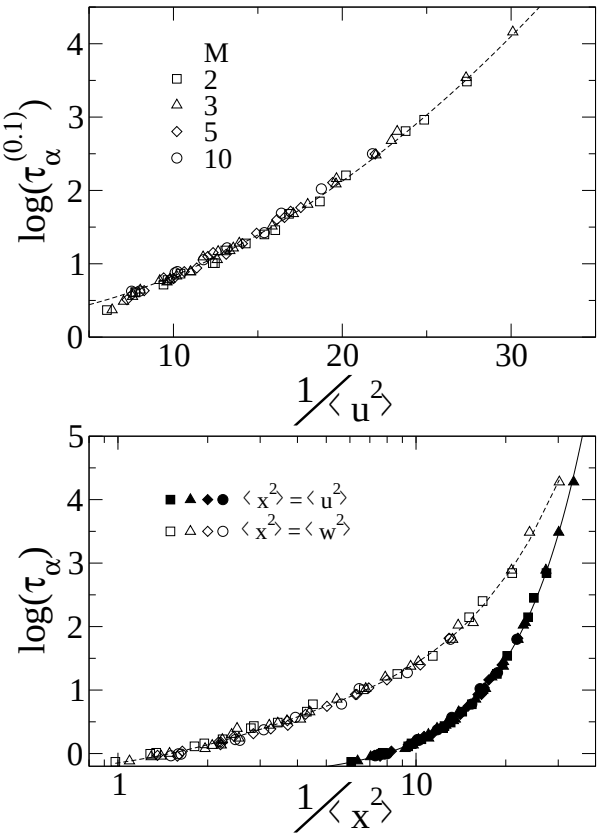

Figure 2.4: Top: the relaxation time $\tau_\alpha^{(0.1)}$, defined by $F_s(q_{max}, \tau_\alpha^{(0.1)})$, versus the ST-MSD $\langle u^2 \rangle$. Dashed line is eq 2.6 with the vertical shift $\alpha' - \alpha = 0.646(2)$. Bottom: the structural relaxation time τ_α versus the ST-MSD evaluated at two different times, $\langle u^2 \rangle = \langle r^2(t^*) \rangle$ (filled symbols) and $\langle w^2 \rangle = \langle r^2(10 \cdot t^*) \rangle$ (open symbols). The solid line across the full symbols is eq 2.6 ; the dashed line across the open symbols is a guide for the eyes.

Equation 2.8 is the correct limit of $G_s(r,t)$ at very short (ballistic regime, $\langle r^2(t) \rangle = 3k_BT/\mu t^2$) and very long times (diffusion regime, $\langle r^2(t) \rangle = 6Dt$, where D is the monomer diffusion coefficient).

The spatial Fourier transform of the self-part of the van Hove function yields the self part of the intermediate scattering function (ISF) [50]:

$$F_s(q,t) = \int G_s(r,t) \exp(-iq \cdot r) dr \tag{2.9}$$

The moments of $G_s(r,t)$ are also of interest:

$$\langle r^n(t) \rangle = 4\pi \int_0^\infty r^n G_s(r,t) r^2 dr \tag{2.10}$$

or alternatively

$$\langle r^n(t) \rangle = \frac{1}{N} \sum_i^N \langle \| \mathbf{r}_i(t) - \mathbf{r}_i(0) \|^n \rangle \tag{2.11}$$

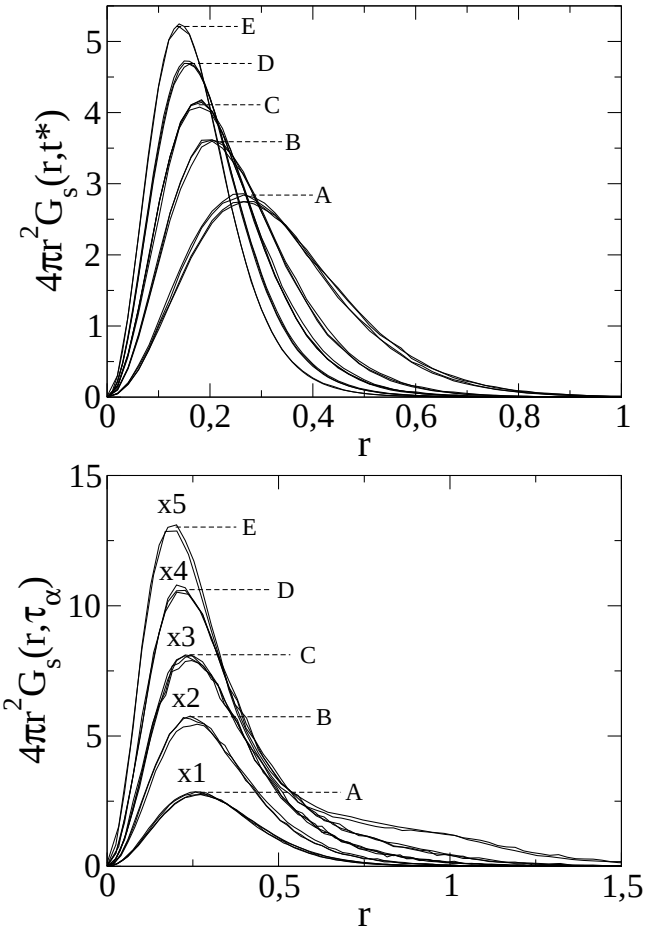

Figure 2.5: Self part of the van Hove function $G_s(r,t)$ of the states of Figure 2.3 at the rattling time $t = t^*$ (top) and the structural relaxation time $t = \tau_\alpha$ (bottom).

For $n = 2$, one recovers the usual mean square displacement.

Figure 2.5 compares the self-part of the van Hove function $G_s(r,t)$ evaluated at either the short time t^* characteristic of the cage rattling (top panel) or τ_α (lower panel). It is seen that states with equal τ_α (the sets of states labelled as A-E) have coinciding $G_s(r,t^*)$ and $G_s(r,\tau_\alpha)$ within about 3 times the monomer radius. The same coincidence is found for any time in the window $t^* \leq t \leq \tau_\alpha$. Note the shoulders at $r \sim 1$ (the monomer diameter) for states D and E in Figure 2.5 (bottom). They signal the marked contribution by jump dynamics [51] and show that the latter fulfills the cage scaling too.

According to eq 2.10, the coincidence of $G_s(r,t)$ in the window $t^* \leq t \leq \tau_\alpha$ for states with equal τ_α implies the coincidence of the moments $\langle r^n(t)\rangle$ in the same interval. Figure 2.6 (top) shows that this is the case for two sets of states and $n = 2, 4, 6$. As a consequence, alternative master curves between the structural relaxation and the higher-order moments of the monomer displacement

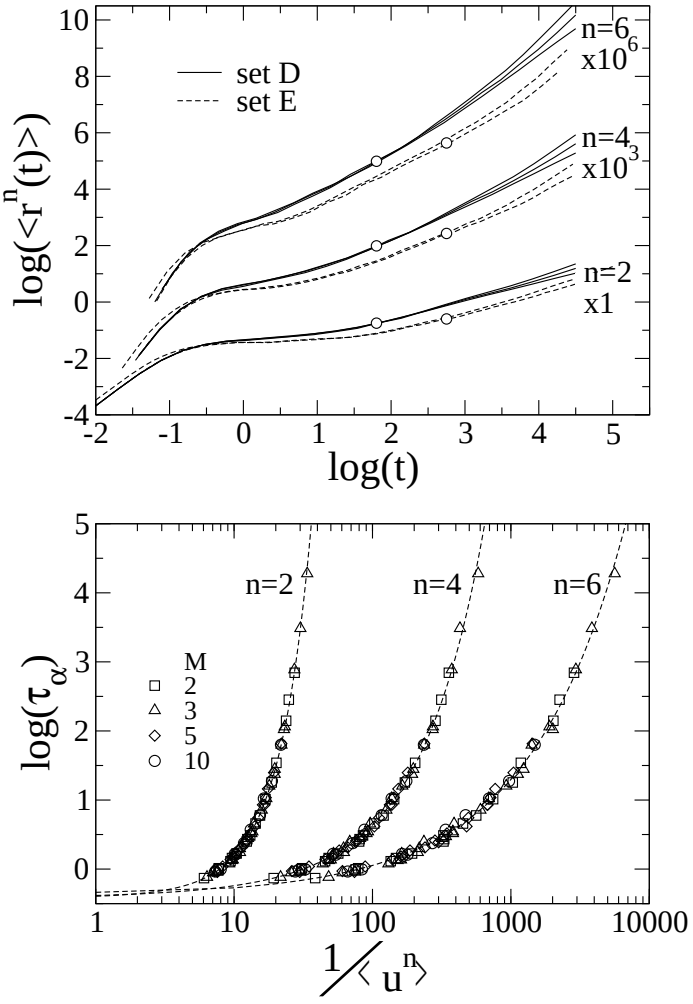

Figure 2.6: Top: time dependence of the moments of the monomer displacement $\langle r^n(t)\rangle$ with $n = 2, 4, 6$ for sets D and E of figure 2.3. The position of structural relaxation time τ_α is marked with dots on each curve. Bottom: τ_α versus$\hat{E}\langle u^n\rangle = \langle r^n(t^*)\rangle$ with $n = 2, 4, 6$. The dashed lines across the data are the laws $\log \tau_\alpha = \alpha^{(n)} + \beta^{(n)}\langle u^n\rangle^{-2/n} + \gamma^{(n)}\langle u^n\rangle^{-4/n}$ with $\alpha^{(2)} = \alpha$, $\beta^{(2)} = \beta$ and $\gamma^{(2)} = \gamma$ as in eq 2.6, $\alpha^{(4)} = -0.427(2)$, $\beta^{(4)} = 3.7(1)\cdot 10^{-2}$, $\gamma^{(4)} = 6.93(4)\cdot 10^{-3}$, $\alpha^{(6)} = -0.425(1)$, $\beta^{(6)} = 4.3(1)\cdot 10^{-2}$, $\gamma^{(4)} = 1.29(3)\cdot 10^{-3}$.

$\langle u^n \rangle = \langle r^n(t^*) \rangle$ may be built up. In Figure 2.6 (bottom) τ_α versus $\langle u^n \rangle$ with $n = 2, 4, 6$ is shown; the case $n = 2$ corresponds to scaling between τ_α and ST-MSD discussed above. The resulting master curves are well described by the law:

$$\log \tau_\alpha = \alpha^{(n)} + \beta^{(n)} \langle u^n \rangle^{-2/n} + \gamma^{(n)} \langle u^n \rangle^{-4/n} \tag{2.12}$$

with $\alpha^{(2)} = \alpha$, $\beta^{(2)} = \beta$ and $\gamma^{(2)} = \gamma$ as in eq 2.6, $\alpha^{(4)} = -0.427(2)$, $\beta^{(4)} = 3.7(1) \cdot 10^{-2}$, $\gamma^{(4)} = 6.93(4) \cdot 10^{-3}$, $\alpha^{(6)} = -0.425(1)$, $\beta^{(6)} = 4.3(1) \cdot 10^{-2}$, $\gamma^{(4)} = 1.29(3) \cdot 10^{-3}$.

Note that the coincidence of the moments $\langle r^2(t) \rangle$ and $\langle r^4(t) \rangle$ for $t^* \leq t \leq \tau_\alpha$ for states with equal τ_α is expected in view of the coincidence of the nongaussian parameter $\alpha_2(t) = \left(3\langle r^4(t) \rangle / 5 \langle r^2(t) \rangle^2\right)$ in the same time window [26] .

Finally the Gaussian approximation $G_s^G(r,t)$ of the van Hove function is treated. Figure 2.7 shows the comparison between t $G_s(r,t)$ and $G_s^G(r,t)$, defined in eq 2.8, at the rattling time $t = t^*$ (left) and at the structural relaxation time $t = \tau_\alpha$ (right) for the sets of clustered curves A, C and E. At short time non-gaussian effects are small and $G_s^G(r,t)$ represents a good approximation of $G_s(r,t)$. Note that the small discrepancies, that are still present, do not seem to depend on the physical state, in agreement with the observed constancy of the non-gaussian parameter $\alpha_2(t)$ at short time [26]. At long times non-gaussian effects are important and the discrepancies between $G_s(r,t)$ and $G_s^G(r,t)$ become increasingly apparent as the sluggishness of the system increases.

2.3.3 Scaling in the diffusion regime

The scaling of the diffusive motion with the cage rattling amplitude $\langle u^2 \rangle$ has been proved for atomic liquids [26]. For polymers, the situation is more complicated in that, while the structural relaxation is weakly dependent on the chain length [52], the dynamics for times longer than τ_α does depend [53]. To show this, first the relaxation time $\tau_q^{(0.1)}$ is defined via the relation $F_s(q, \tau_q^{(0.1)}) = 0.1$; note that the usual definition via the relation $F_s(q, \tau_q) = 1/e$ is not appropriate due to the strong q-dependence of the plateau region of the ISF at intermediate times, especially for large q value [18]. Figure 2.8 plots the wave-vector dependence of $\tau_q^{(0.1)}$. When $q \sim 2\pi/r_0$, being $r_0 \approx 1$ the distance of the nearest neighbors, the cage length scale is probed, and the relaxation time $\tau_q^{(0.1)} \sim \tau_\alpha^{(0.1)}$ is not dependent on the chain length. If $q \gtrsim 2\pi/R_{ee}$, where $R_{ee} = 1.42 b^2 (M-1)$ is the mean square end-to-end distance of the chain [52], the length scale of a chain is probed. In this regime, the relaxation data are not collapsed on a master curve, even if they are at $q \sim 2\pi/r_0 \sim q_{max}$, i.e., the original form of the scaling of the structural relaxation time. When $q < 2\pi/R_{ee}$ the relaxation is controlled by the diffusive motion of the monomers. If one considers short chain, up to $M = 5$ for which $R_{ee} \approx 2.5$, $q \lesssim 1$ is sufficient to observe the onset of the diffusive regime. Figure 2.8 shows that in the region $q \lesssim 1$ a power-law behavior for $\tau_q^{(0.1)}$ is found of the type $\tau_q^{(0.1)} \sim q^{-2}$. This can be interpreted if we consider the Gaussian approximation of the intermediate

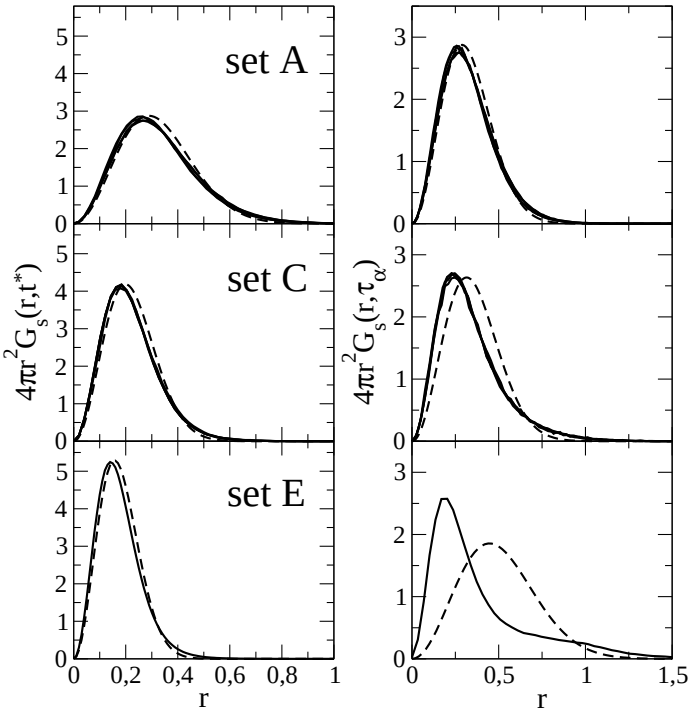

Figure 2.7: Comparison between the self part of the van Hove function $G_s(r,t)$ (full line) and the Gaussian approximation $G_s^G(r,t)$ (dashed line), defined in eq 2.8, at the rattling time $t = t^*$ (left) and at the structural relaxation time $t = \tau_\alpha$ (right) for the sets of clustered curves A, C and E in Figure 2.3.

scattering function;

$$F_s^G(q,t) = \exp\left(-\frac{1}{6}q^2\langle r^2(t)\rangle\right) \tag{2.13}$$

where $\langle r^2(t)\rangle$ is the monomer MSD. Figure 2.9 top shows the comparison between $F_s(q,t)$ and the corresponding Gaussian approximation $F_s^G(q,t)$ eq 2.13 for five different q values. For $q \approx 1$ the agreement is very good and the explanation of the decay of $F_s(q,t)$ in terms of the monomer mean square displacement is allowed (see Figure 2.9 bottom). At long times, the monomer displacement is diffusive, $\langle r^2(t)\rangle = 6Dt$ holds, where D is the diffusion coefficient; this results in a relaxation time $\tau_q^{(0.1)} \propto 1/(Dq^2)$. For longer chain, a power-law $\tau_q^{(0.1)} \sim q^{-n}$ ($n \gtrsim 3$) is observed for $q \sim 1$ (see $M = 10$ in Figure 2.8) corresponding to a sub diffusive regime where $\langle r^2(t)\rangle \sim t^{x_0}$ ($x_0 \approx 0.65$), i.e. a crossover between Rouse regime $\langle r^2(t)\rangle \sim t^{1/2}$ for unentangled chain ($M \lesssim 32$) and free diffusion $\langle r^2(t)\rangle \sim t$.

To extend the scaling between relaxation and caged dynamics to the diffusive regime of polymers, one defines the diffusion relaxation time:

$$\tau_D = \lim_{q\to 0} \tau_q^{(0.1)} \tag{2.14}$$

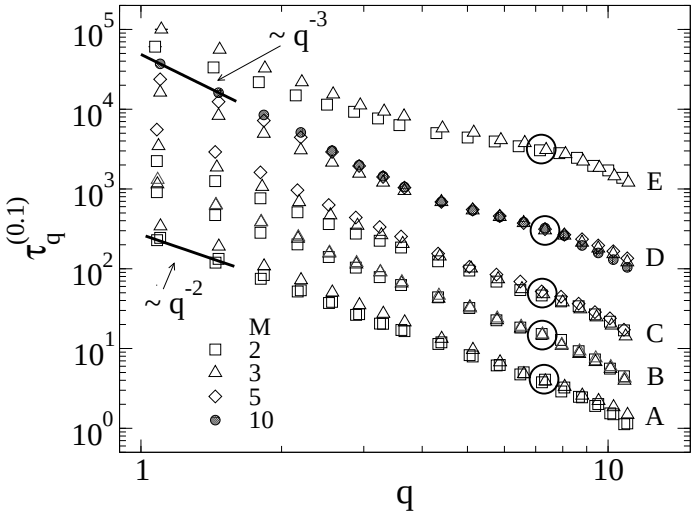

Figure 2.8: Wave-vector dependence of the relaxation time $\tau_q^{(0.1)}$ for the states of Figure 2.3 with chain length $M = 2, 3, 5$. Empty circles mark the structural relaxation time $\tau_{q_{max}}^{(0.1)}$. For small q values, the onset of the diffusive regime is observed, $\tau_q^{(0.1)} \sim q^{-2}$. A single state with $M = 10$ is plotted to show the sub diffusive behavior $\tau_q^{(0.1)} \sim q^{-n}$ with $n \gtrsim 3$ occurring at small q values for longer chains.

In practice, as stated above, it's enough to consider $q \lesssim 2\pi/R_{ee}$. Figure 2.10 top plots ISF at $\tilde{q}$, the smallest q vector of our simulations, and consider the sets of states A-E with equal structural relaxation time and chain length $M = 2, 3, 5$ (see Figure 2.3). It is seen that the decay at long times collapse by using the reduced time t/M. This is readily explained since $\tau_D \propto 1/(Dq^2)$ and for short unentangled chains $D \propto M^{-1}$ [18] (see Appendix B). Figure 2.10 bottom shows that the collapse of MSD at long times is also obtained by using the reduced time t/M. We are now in the position to conclude that if two states have equal relaxation time τ_α, and ST-MSD $\langle u^2 \rangle$, the states have also equal reduced diffusion coefficient $DM = M \cdot \lim_{t\to\infty} \langle r^2(t) \rangle / 6t$. However, it must be noted that deviations from the previous scaling law $D \propto M^{-1}$ are seen at lower temperatures than the one considered in the present study [54].

We consider now the scaling of the polymer diffusion regime with the ST-MSD $\langle u^2 \rangle$. First we define the quantity $\overline{D} = (\tilde{q}^2 \tau_D)^{-1} \propto D$. Figure 2.11 plots the reduced quantity $2/\overline{D}M$, proportional to $1/(DM)$, versus the ST-MSD $\langle u^2 \rangle$. If the effects of the chain length are properly treated, the scaling holds even at the very long times of polymer diffusion (see the inset of Figure 2.11 for the raw data). The resulting master curve is:

$$\log\left(2/\overline{D}M\right) = \alpha_D + \beta_D \langle u^2 \rangle^{-1} + \gamma_D \langle u^2 \rangle^{-2} \tag{2.15}$$

where $\alpha_D = 1.80(5)$, $\beta_D = 6.7(3) \cdot 10^{-2}$ and $\gamma_D = 1.62(2) \cdot 10^{-3}$. In Figure 2.11 it is also shown explicitly the proportionality between the diffusion coefficient D and the quantity $\overline{D}$, in particular it has been found $\overline{D} \approx 0.45\, D$.

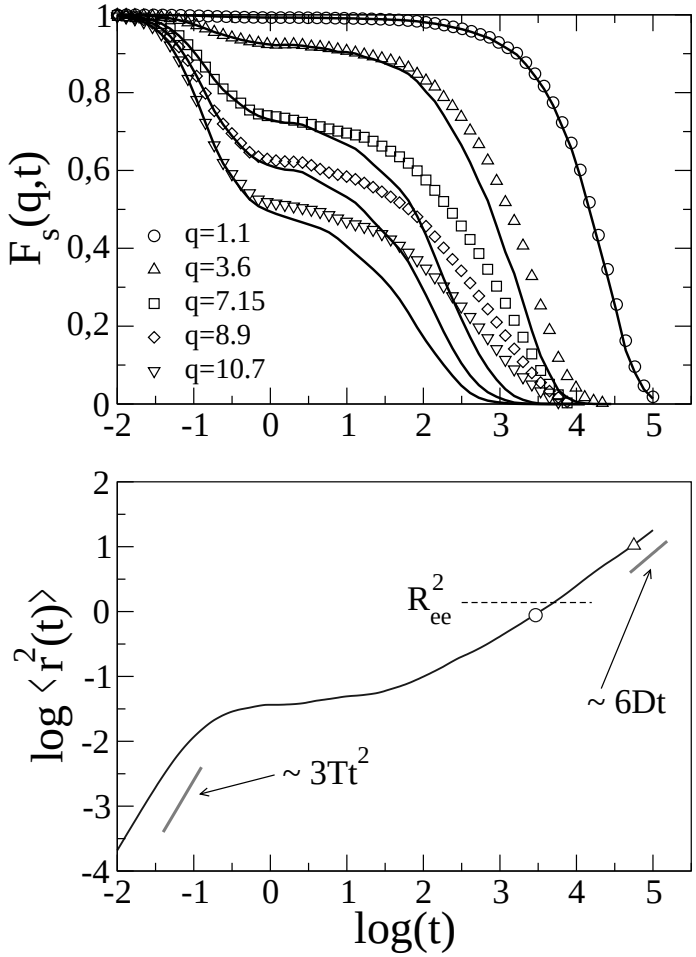

Figure 2.9: Top: comparison between $F_s(q,t)$ and the Gaussian approximation $F_s^G(q,t)$ eq 2.13 with five different q values for the state with $M = 2$, $\rho = 1.0$, $T = 0.7$ and $(p,q) = (11,12)$. For the smallest q value the agreement is very good. Bottom: corresponding monomer MSD. Diffusive behavior $\langle r^2(t)\rangle = 6Dt$ is indicated, starting for $\langle r^2\rangle > R_{ee}^2$, where R_{ee}^2 is the mean square end-to-end distance of the chain. Ballistic regime $\langle r^2(t)\rangle = (3k_BT/m)t^2$ at short time is also indicated. Circle and triangle mark $\tau_q^{(0.1)}$ at $q = q_{max}$, the maximum of the static structure factor, and $q \approx 1$, the smallest q value of our simulation, respectively.

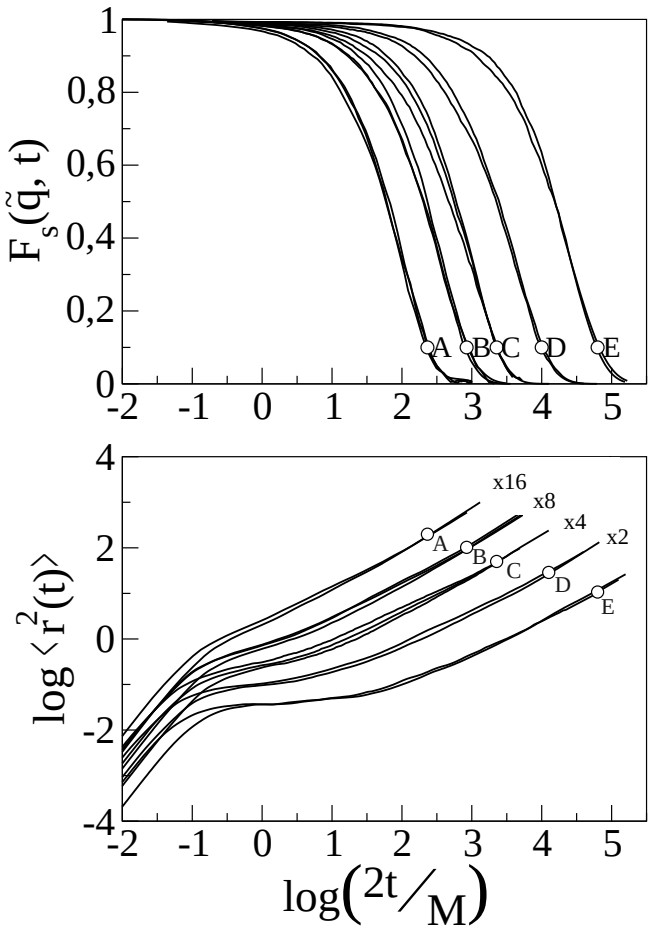

Figure 2.10: Top: long time scaling of $F_s(\tilde{q}, t)$ for the states of Figure 2.3 with $M = 2, 3, 5$. $\tilde{q} \approx 1$ is the smallest q vector of our simulations. Bottom: corresponding long time scaling of MSD. The sets of clustered curves A-E show that, if states have equal τ_α, and ST-MSD $\langle u^2 \rangle$, they have also equal diffusion coefficient D. Circles mark the time $2\tau_D / M$.

One comment has to be made concerning the diffusion master curve. In Figure 2.11 the diffusion scaling is compared to eq 2.6, the master equation of $\log(\tau_\alpha)$ scaling. At high temperature, small relaxation time, the two curve are identical except a constant vertical shift, i.e., D^{-1} and τ_α are proportional. This is due to the Stokes-Einstein relation which account the coupling between the translational diffusion and the viscous flow, being τ_α an effective surrogate of η. As the temperature is lowered, deviation between the two master curve become apparent suggesting a breakdown of the Stokes-Einstein relation, an issue which is discussed in the next section.

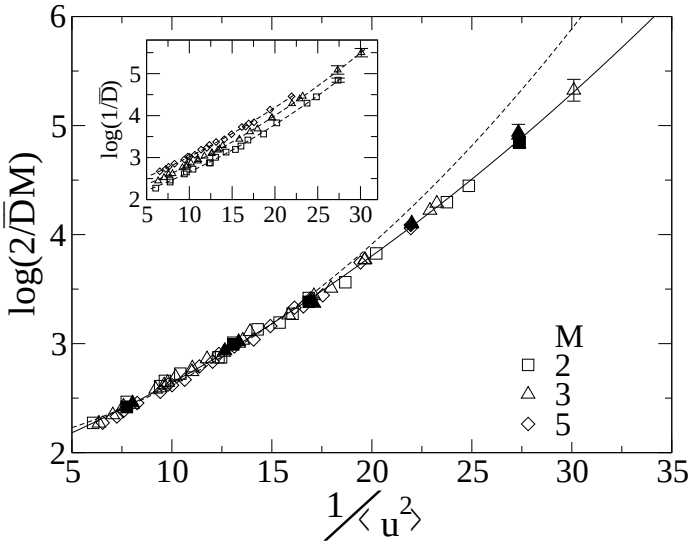

Figure 2.11: Scaling plot of the reduced $\overline{D} = (\tilde{\eta}^2 \tau_D)^{-1}$ versus the ST-MSD $\langle u^2 \rangle$ (open symbols) for polymers with different length M. Diffusion coefficient data are also plotted (full symbols) to show the relation $\overline{D} \approx 0.45\, D$ between the diffusion coefficient D and $\overline{D}$. Full line is eq 2.15 $\log\left(2/\overline{D}M\right) = \alpha_D + \beta_D \langle u^2 \rangle^{-1} + \gamma_D \langle u^2 \rangle^{-2}$ with best-fit parameters $\alpha_D = 1.80(5)$, $\beta_D = 6.7(3) \cdot 10^{-2}$ and $\gamma_D = 1.62(2) \cdot 10^{-3}$. Dashed line is eq 2.6, i.e., the master curve of the τ_α versus $\langle u^2 \rangle$ scaling, with a vertical shift $+2.45$. The discrepancies between the two master curves, emerging at low temperature, suggest the onset of a decoupling between diffusion coefficient D and α-relaxation time τ_α. Inset: the raw data of the diffusion relaxation time τ_D versus the ST-MSD $\langle u^2 \rangle$; dashed line are parabolic guides for the eyes.

2.3.4 Dynamic heterogeneity and Stokes-Einstein violation

Here we discuss the breakdown of the Stokes-Einstein (SE) equation in the present model of a melt of fully flexible linear chain. The diffusion of macroscopic objects in liquids is usually well described by the Stokes-Einstein (SE) equation. For a sphere with radius a and stick boundary conditions the SE equation equals

$$D = \frac{k_B T}{6\pi a \eta} \tag{2.16}$$

In spite of the hydrodynamic arguments used in its derivation, the SE relation works even if the size of the diffusing particle is comparable to the size of the fluid molecules [55]. Close to the glass transition, it is seen that D and η "decouple", i.e., the actual diffusion is higher than the one predicted by eq 2.16 [51, 56–59]. Phenomenologically, it is found that decoupling is well accounted for by the so called fractional SE (FSE) law $D \propto \eta^{-\xi}$ with the non-universal exponent ξ in the range $[0.5 - 1]$ [60–63].

In Figure 2.12 the diffusion coefficient D (in which the chain length dependence is removed) versus the structural relaxation time τ_α from MD simulations is plotted. Deviations from the expected $(DM) \sim \tau^{-1}$ are apparent as

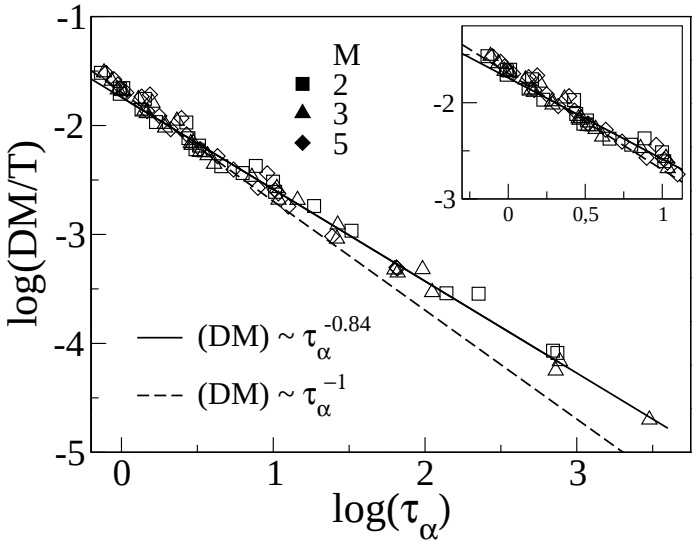

Figure 2.12: Diffusion coefficient D versus the structural relaxation time τ_α from MD simulations of chains with length $M = 2, 3, 5$. Chain length dependence of D is removed. Deviations from the expected $\tau_\alpha \sim (DM/T)^{-1}$ (dashed line) become apparent as the structural relaxation time increases. Full line is the best-fit curve $(DM/T) \sim \tau_\alpha^{-\zeta}$ with $\zeta = 0.84(1)$. The inset magnifies the "high temperature" region where the Stokes-Einstein is still valid.

the sluggishness of the system increases. The onset of the fractional Stokes-Einstein FSE $(DM) \sim \tau_\alpha^{-\zeta}$ is observed for $\tau_\alpha \gtrsim 10$ in MD units. The exponent of the FSE is $\zeta = 0.84(1)$. This value agrees with the FSE observed in several glass forming liquids [64].

A popular explanation of the breakdown of the SE equation relies on the existence of spatially heterogeneous dynamics, the so called "dynamic heterogeneity" (DH) [56, 58]. In the framework of DH, the breakdown of the SE relation is due to the fact that diffusion is dominated by the fastest clusters, whereas the viscous flow or the structural relaxation is dominated by the slowest ones.

The usual quantity to describe DH is the non-gaussian parameter (NGP):

$$\alpha_2(t) = \frac{3\langle r^4(t)\rangle}{5\langle r^2(t)\rangle^2} - 1 \tag{2.17}$$

where $\langle r^2(t)\rangle$ and $\langle r^4(t)\rangle$ are the mean square and quartic displacements of the particle, respectively. α_2 vanishes if the displacement is gaussian, i.e., it follows from a series of independent elementary steps with finite mean and variance. This is expected in liquids with high fluidity, whereas in supercooled liquids regions with solid-like jump dynamics coexist with liquid-like domains and motions are highly correlated, thus yielding non-zero α_2. The NGP is shown in Figure 2.13 for the state points of Figure 2.3. Starting from the ballistic regime, where the it is zero, the NGP increase signaling the cage

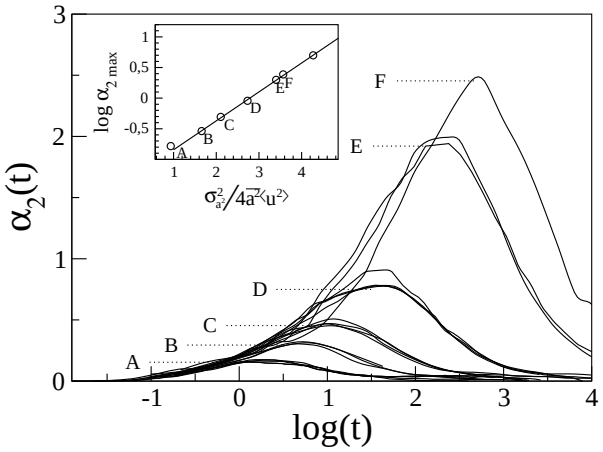

Figure 2.13: Time dependence of the non-gaussian parameter $\alpha_2(t)$ (NGP) for the state points of Figure 2.3. The plot shows that for states with equal τ_α not only MSD and ISF coincide between t^* and τ_α (see Figure 2.3) but also NGP does the same within the statistical uncertainty. Inset: the maximum of the NGP α_2^{max} versus the ratio of the quadratic and the linear terms of eq 2.2 with respect to $\langle u^2 \rangle^{-1}$.

regime. The NGP returns to zero at long times because the diffusion regime at long times is strictly Gaussian; this happens around the structural relaxation time when the cage regime ends and the NGP starts to decrease.

We show that the ratio of the quadratic and the linear terms of eq 2.2 with respect to $\langle u^2 \rangle^{-1}$, $\mathcal{R} = \sigma^2_{a^2}/4\overline{a^2}\langle u^2 \rangle$ is a good signature of DH. First, remind that the concavity of the master curve eq 2.6 is due to $\sigma_{a^2} \sim 0.25 \neq 0$ indicating the distribution of the displacement required to overcome the energy barriers. Then we observe that ratio $\mathcal{R}$ discriminates two different regimes. If $\mathcal{R} < 1$ (large ST-MSD) the quadratic term is negligible and the distribution of the square displacements to overcome the energy barriers is so narrow that it can be replaced by an effective step length $\overline{a^2}^{1/2}$, i.e., the dynamics is homogeneous. If $\mathcal{R} > 1$ (small ST-MSD) the displacement distribution shows up and a heterogeneous mobility distribution is anticipated. A relation between $\mathcal{R}$ and the maximum α_2^{max} of NGP exists [26]: when $\mathcal{R}$ exceeds the unit value, α_2^{max} increases exponentially (see the inset of Figure 2.13).

Now we are in the position to investigate the correlation between DH and the violation of the SE relation. In Figure 2.14 the product $(DM/T) \cdot \tau_\alpha$ is plotted versus both the maximum α_2^{max} of NGP (top panel) and the ratio $\mathcal{R} = \sigma^2_{a^2}/4\overline{a^2}\langle u^2 \rangle$ (bottom panel). The onset of the violation of the SE relation occurs at $\alpha_{2,c}^{max} = 0.40(5)$ or $\mathcal{R}_c = 1.9(1)$. Note that the ratio $\mathcal{R}$ allows to locate the violation with a greater precision with respect to α_2^{max}. Furthermore, it is interesting that the breakdown occurs for $\mathcal{R} \gtrsim 1$, i.e., when the quadratic terms become larger than the linear one in eq 2.2 and the concavity of the curve become apparent (see the bottom panel of Figure 2.14). This is a confirmation of the fact that the concavity of eq 2.6 is strictly related to DH.

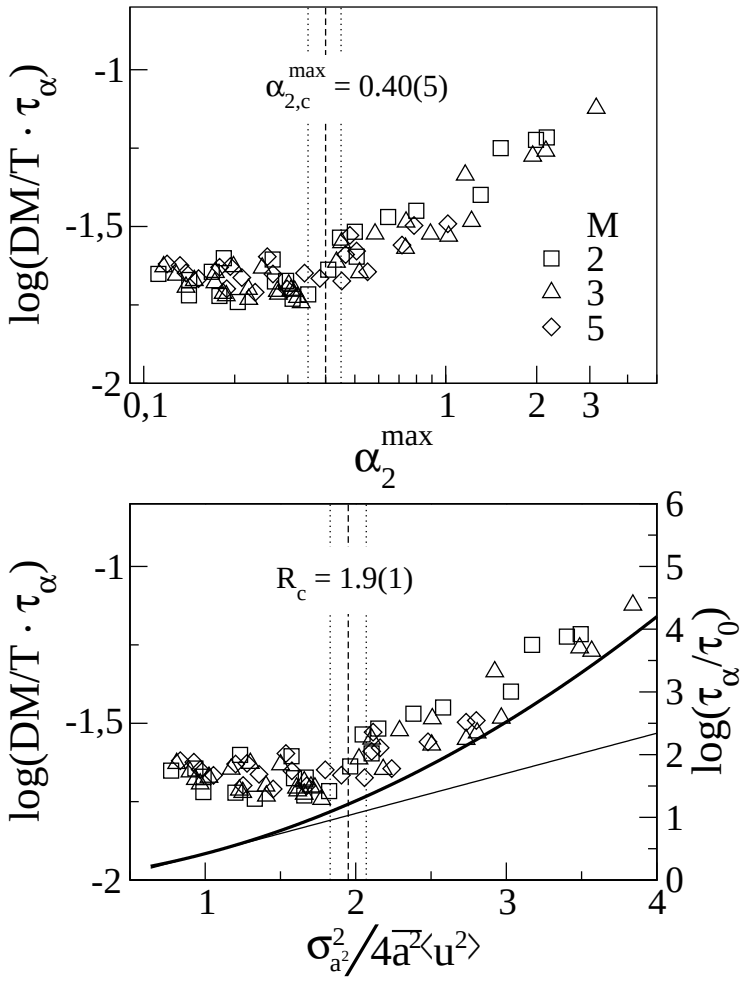

Figure 2.14: Violation of the Stokes-Einstein relation: the product $DM/T \cdot \tau_\alpha$ versus α_2^{max} the maximum of the non-gaussian parameter (top panel) and the ratio $\mathcal{R} = \sigma^2_{a^2}/4\overline{a^2}\langle u^2\rangle$ (bottom panel). The onset of the violation occurs at $\alpha_{2,c}^{max}$ and R_c respectively, indicated as the dashed lines (dotted line marks the uncertainty on these values). Thick line in the bottom panel is eq 2.2 expressed as a function of $\mathcal{R}$ while the thin line is the corresponding best-approximating line for small $\mathcal{R}$ values.

2.3.5 Displacement-displacement correlations

In this section we address the issue of how single-particle dynamics correlates with the one of the neighbors at both short, i.e. vibrational, and long times, i.e., comparable to structural relaxation time τ_α.

We consider both the scalar and the vector character of the displacement-displacement correlations. To this aim, the correlation function of the *direction* of the displacement (D-DDC) is defined as:

$$C_{\vec{u}}(r,t) = \frac{1}{N}\sum_{i=1}^{N}\left\langle \hat{\mathbf{u}}_i(t_0,t)\cdot\frac{1}{N_i(r,t_0)}\sum_{j=1}^{N}\hat{\mathbf{u}}_j(t_0,t)\delta(r-|\mathbf{r}_{ij}(t_0)|)\right\rangle \tag{2.18}$$

where $\hat{\mathbf{u}}_k(t_0,t)$ is the versor of the displacement vector of k-th monomer in a time interval from t_0 to t_0+t, $\mathbf{u}_k(t_0,t) = \mathbf{r}_k(t_0+t)-\mathbf{r}_k(t_0)$. $N_i(r,t_0) = \sum_{j=1}^{N}\delta(r-|\mathbf{r}_{ij}(t_0)|)$ is the number of monomers at distance r from the i-th one at time t_0. The correlation function does not depend on t_0 because the system is in equilibrium. Furthermore, we address the correlations of the *modulus* of the displacement, i.e., the mobility, and define the related correlation function (M-DDC) as:

$$C_{\delta u}(r,t) = \frac{1}{\langle \delta u(t_0,t)^2\rangle}\left[\frac{1}{N}\sum_{i=1}^{N}\left\langle \delta u_i(t_0,t)\frac{1}{N_i(r,t_0)}\sum_{j=1}^{N}\delta u_j(t_0,t)\delta(r-|\mathbf{r}_{ij}(t_0)|)\right\rangle\right] \tag{2.19}$$

where $\delta u_k(t_0,t)$ is the mobility fluctuation of k-th particle, $\delta u_k(t_0,t) = |\mathbf{u}_k(t_0,t)| - \langle|\mathbf{u}(t)|\rangle$ and $\langle \delta u(t_0,t)^2\rangle = 1/N\,[\sum_{j=1}^{N}\delta u_j(t_0,t)^2\,]$

The above two correlation functions yield $C_{\vec{u}} = C_{\delta u} = 1$ and $C_{\vec{u}} = C_{\delta u} = 0$ for perfectly correlated and completely uncorrelated displacements, respectively. Notice also that $C_{\vec{u}}$ and $C_{\delta u}$ coincide with $S_{\vec{u}} = \langle \vec{u}_i\cdot\vec{u}_j\rangle/\langle u^2\rangle$ and $S_{\delta u} = \langle \delta u_i\delta u_j\rangle/\langle(\delta u)^2\rangle$ defined in refs. [65, 66].

In Fig. 2.15 the spatial dependence of $C_{\vec{u}}(r,\Theta)$ and $C_{\delta u}(r,\Theta)$ at the rattling time $\Theta = t^*$ is shown for the sets of states labelled A through E in Fig.2.3. Both correlation functions manifest damped oscillations in-phase with the pair correlation function $g(r)$, thus evidencing that the correlated motion of a tagged monomer and its surroundings is influenced by the structure of the latter. This agrees with previous work on DDCs in Lennard-Jones systems [67, 68], hard-sphere [65] and colloids [66]. The highest correlations are reached at a distance corresponding to the bond length $b = 0.97$ which is a manifestation of the concerted dynamics of bonded monomers. Even if M-DDC and D-DDC are nearly equal at $r = b$, the magnitude of the latter is *larger* for $r > b$. The correlation peaks, located at the first-, second-,... neighbors shells, vanish approximately in an *exponential* way on increasing the distance from the tagged particle (see insets of Fig. 2.15). Distinctly, a $1/r$ decay is observed in colloids at short time which is reminiscent of continuum-like response [66]. Correlations decrease in regions with lower local density and, for mobility fluctuations, strikingly *vanish* for distances corresponding to the minima of $g(r)$.

Figure 2.15 shows that, on increasing τ_α, i.e., moving from A states to E states, the spatial correlations of the mobility fluctuations hardly change. Instead, the direction correlations tend to: i) increase in magnitude, ii) extend

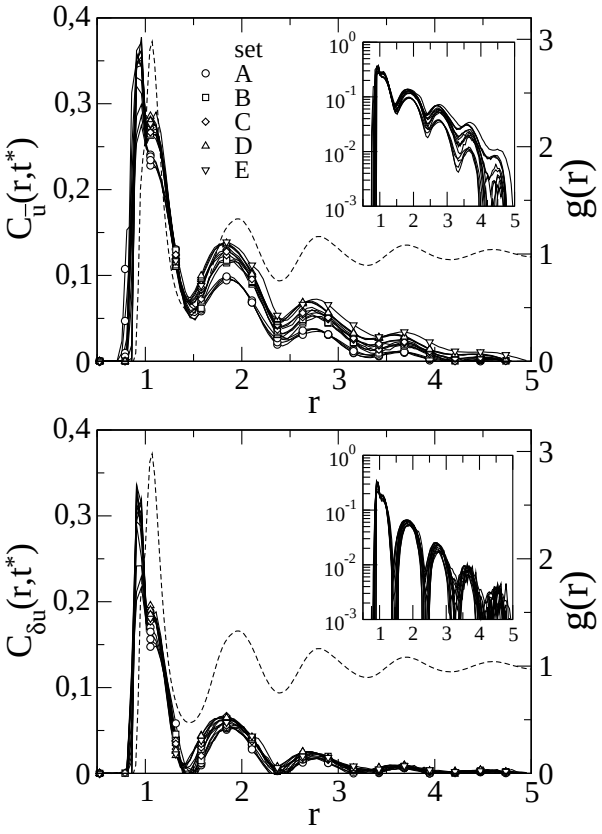

Figure 2.15: Radial dependence of the correlation of the direction (top) and the mobility fluctuation (bottom) at the rattling time t^*. For comparison, the radial distribution function $g(r)$ (dashed line) of the state with $\{\mathrm{M} = 2, æ = 1.086, \mathrm{T} = 0.7, \mathrm{q} = 7, \mathrm{p} = 6\}$ is plotted. The insets are semi-log plots of the corresponding main panels. Note the approximate exponential decay of the peak amplitudes.

for larger distances, and iii) be less modulated by the local structure, see inset of Fig.2.15, top. This finding is quite interesting in the light of the correlation between the structural relaxation time and $\langle u^2 \rangle$ (Eq.2.5) [25, 26]. It suggests that the correlation is a manifestation of the increasing vector coherence of the short time displacements in both magnitude and spatial extension when solidity increases.

In Figure 2.16 the plot of $C_{\vec{u}}(r, \tau_\alpha)$ and $C_{\delta u}(r, \tau_\alpha)$, accounting for the spatial correlations of the displacements performed over τ_α, is shown for the same states of Fig.2.15. Again, in-phase oscillations with the radial distribution function are observed, even if with slightly decreased amplitude. This latter effect is particularly pronounced for modulus correlations. The direction correlations are shown in Fig. 2.16 (top). With respect to short times, they do not show significant increase in their spatial extension and still decay in an approximate exponential way. As a notable difference with short times, the dependence of the direction correlations on the structural relaxation time is

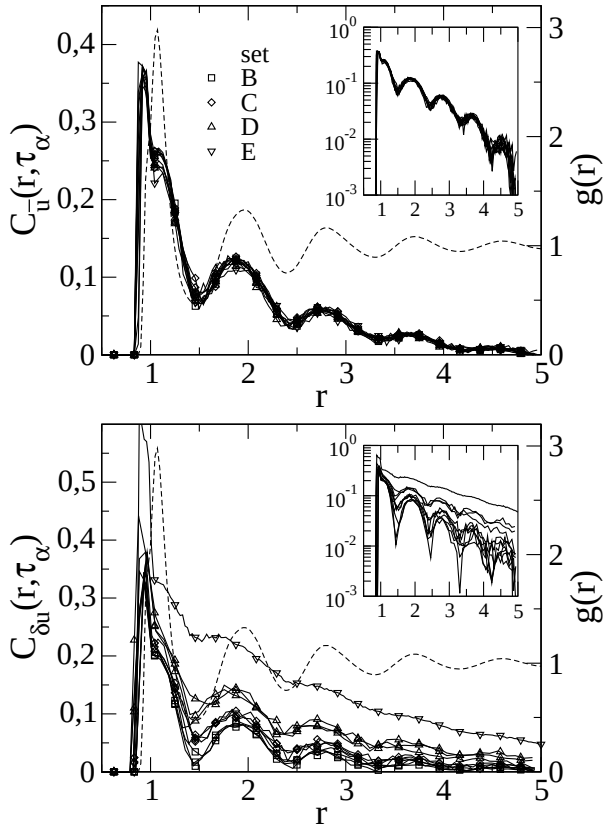

Figure 2.16: Radial dependence of the correlation of the direction (top) and the mobility fluctuation (bottom) at the structural relaxation time τ_α. For comparison, the radial distribution function $g(r)$ (dashed line) of the state with $\{\mathrm{M} = 2, \text{æ} = 1.086, \mathrm{T} = 0.7, \mathrm{q} = 7, \mathrm{p} = 6\}$ is plotted. The insets are semi-log plots of the corresponding main panels. Note the approximate exponential decay of the peak amplitudes.

much weaker. Fig. 2.16 (bottom) shows the modulus (mobility) correlations. Two major differences with respect to short times are apparent, i.e., both their spatial extension and the oscillations damping increase meaningfully with the structural relaxation time (see the inset of Fig. 2.16, bottom). It is also clearly seen that physical states with equal τ_α, i.e., belonging to the same set of states (A, $\cdots$, E), exhibit the same spatial correlations. Closer inspection of Fig.2.15 (top) shows that this feature, even if less apparent, is also present in $C_{\vec{u}}(r, t^\star)$.

By comparing Fig. 2.15 and Fig. 2.16, one observes that, while at short times $C_{\vec{u}}(r, t^\star) > C_{\delta u}(r, t^\star)$, the opposite is true at long times, i.e., $C_{\vec{u}}(r, \tau_\alpha) < C_{\delta u}(r, \tau_\alpha)$, in agreement with what is observed in experiments on colloids [66]. These results supports the picture that, while the rattling of particles within the cage of their neighbors are directionally correlated in space, cage rearrangements involve particles moving in different directions.

In order to make more quantitative the analysis of Figs.2.15,2.16, we re-

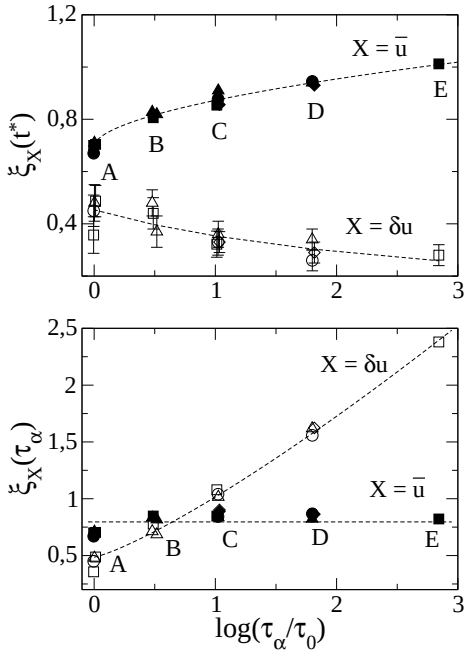

Figure 2.17: Dependence of the direction ($\xi_{\vec{u}}(\Theta)$, full symbols) and modulus ($\xi_{\delta u}(\Theta)$, open symbols) correlation lengths (eq 2.20) on the structural relaxation time τ_α. Top: $\Theta = t^\star$, bottom: $\Theta = \tau_\alpha$. Dashed lines are guides for the eyes.

mind that DDCs decay almost exponentially with the distance (see insets of Fig. 2.15, 2.16):

$$\widetilde{C}_X(R,\Theta) \approx A_X(\Theta)\exp(-R/\xi_X(\Theta)), \quad X = \vec{u}, \delta u \tag{2.20}$$

where R denotes a local maximum of $C_X(r,\Theta)$ with $X = \vec{u}, \delta u$. $\xi_X(\Theta)$ is a dynamic correlation length depending on the considered time scale Θ. Fig.2.17 (top) shows the dependence of $\xi_{\vec{u}}(t^\star)$ and $\xi_{\delta u}(t^\star)$ on the structural relaxation time τ_α. It is seen that the direction correlations are spatially more extended on the time scale of the rattling motion $t^\star$, i.e., $\xi_{\vec{u}}(t^\star) > \xi_{\delta u}(t^\star)$. Furthermore, the direction correlation length increases mildly with τ_α, whereas the modulus correlation tend to become more localized. In Fig.2.17 (bottom) the correlation lengths $\xi_{\vec{u}}(\Theta)$ and $\xi_{\delta u}(\Theta)$ are shown for the timescale $\Theta = \tau_\alpha$. On this time scale the spatial extension of the correlations of the displacement modulus increases quite a lot with τ_α and reaches distances beyond the next-nearest neighbors for the states with the slowest relaxation. Instead, the direction correlations are virtually independent of the structural relaxation. Notice that for the A states $\tau_\alpha \simeq t^\star$ and then $\xi_X(\tau_\alpha) \simeq \xi_X(t^\star), X = \vec{u}, \delta u$. On increasing τ_α, one sees that the ratio $\xi_{\vec{u}}(\tau_\alpha)/\xi_{\vec{u}}(t^\star)$ decreases weakly from ~ 1 to ~ 0.8, whereas the ratio $\xi_{\delta u}(\tau_\alpha)/\xi_{\delta u}(t^\star)$ increases markedly from ~ 1 to ~ 9.

We are now in a position to compare our results with previous work on DDCs. Simulations of Lennard-Jones binary mixture (BM) [69] observed that, at time t_α corresponding to maximum dynamic heterogeneity, $\xi^{BM}_{\delta u}(t_\alpha)$ in-

creases as the temperature decreases while $\xi_{\vec{u}}^{BM}(t_\alpha)$ is almost constant. This agrees with our findings at the structural relaxation time ($t_\alpha \leq \tau_\alpha$), see Fig.2.17 (bottom). However, our direction correlation length, $\xi_{\vec{u}}(\tau_\alpha) \sim 0.8$, is significantly smaller than the one observed in the binary mixture, $\xi_{\vec{u}}^{BM}(t_\alpha) = 1.7$. This effect could be due to the lower density of our systems. In a study of the same polymer system investigated here Bennemann et al. adopted a different definition of the M-DDC correlation length [67], which may be recast in the form [66]:

$$\xi'_{\delta u}(\Theta) = (\langle u^2(\Theta)\rangle / \langle u(\Theta)\rangle^2 - 1) \int dr\, C_{\delta u}(r, \Theta)$$

In the present study, if $\Theta = \tau_\alpha$, the pre-factor in parenthesis changes from 0.30 for states belonging to set A up to 0.63 for set E. By numerically evaluating the integral, we find that $\xi'_{\delta u}(\tau_\alpha)$ increases from 0.05 for set A to 0.43 for set E in good agreement with ref. [67], where for τ_α increasing from ~ 1 up to $\sim 10^3$ the range spanned is $0.05 - 0.32$.

We discuss the issue of dynamic heterogeneity in the framework of the displacement-displacement correlation functions. To this aim, we first define the subsets of fastest and slowest monomers by comparing the self part $G_s(r,t)$ of the van Hove function with its Gaussian approximation, eq 2.8. Even if $G_s^g(r,t)$ describes the single-particle motion fairly well at high temperature, deviations are seen when the dynamics slow down [70]. They manifest as excess contributions at small and large distances, denoting the presence of an excess of slow and fast monomers, respectively. To quantify the deviations from the gaussian limit, one defines the quantity [51, 70].

$$N_s(r,t) = \frac{G_s(r,t) - G_s^g(r,t)}{G_s^g(r,t)} \tag{2.21}$$

Fig. 2.18 plots $N_s(r,t)$ for the rattling time $t = t^*$ (upper panel) and the structural relaxation time $t = \tau_\alpha$ (lower panel). The ratio $N_s(r,t)$ exhibits increasing positive deviations at both short and large r values, evidencing the excess of nearly immobile and highly mobile monomers with respect to purely gaussian behavior, respectively. Note that the excess is apparent also at short times, i.e., $t = t^*$, where the deviations from the gaussian behavior, as quantified by the non-gaussian parameter $\alpha_2(t) = (3\langle r^4(t)\langle / 5\langle r^2(t)\rangle^2) - 1$, are small, i.e., dynamical heterogeneity is weak [71].

We now define the subsets of the highly mobile and nearly immobile monomers. Being $r_s(t)$ and $r_f(t)$ the zeros of $N_s(r,t)$ with $r_f(t) > r_s(t)$ (see Fig.2.18), a slow monomer is a particle that moved less than the distance $r_s(t)$ within the time t, whereas fast monomers are particles that moved more than $r_f(t)$ [51, 70]. Fig.2.18 (top) shows that the ratio $N_s(r,t^\star)$ for $r \leq r_s(t^\star)$, as well as $r_s(t^\star)$ itself, depends weakly on τ_α. Instead, $r_f(t^\star)$ decreases with increasing τ_α signaling a stronger tendency to positive deviations at large r values. Nonetheless, at $t = t^*$ the fraction of slow monomers and fast monomers are respectively about 37% and 6% of the total number of monomers with no significant changes with τ_α. Reminding that the definition of both the fast and the slow monomer rely on the *modulus* of the particle displacement within time t, the weak dependence of the fast and the slow populations at short times

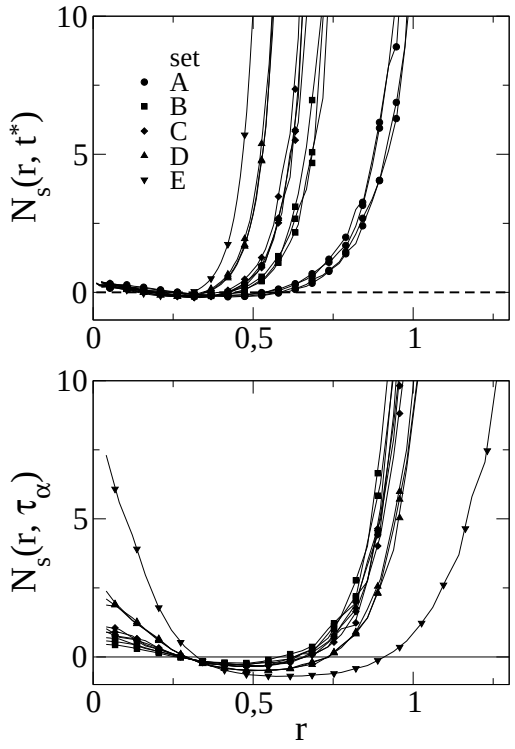

Figure 2.18: The ratio $N_s(r,t) = (G_s(r,t) - G_s^g(r,t))/G_s^g(r,t)$ of the states of Fig.2.3 at the rattling time $t = t^*$ (top) and at the structural relaxation time $t = \tau_\alpha$.

($t = t^\star$) on the structural relaxation time has interesting counterparts in the virtual independence on τ_α in both M-DDC, $C_{\delta u}(r, t^\star)$, (Fig.2.15, bottom) and the related (small) correlation length $\xi_{\delta u}(t^\star)$ (Fig.2.17, top). We conclude that at short times both the mobility distribution and its (limited) spatial correlation are little affected by the slowing down of the structure rearrangement.

Fig.2.18 (bottom) plots $N_s(r, \tau_\alpha)$. One notices a much stronger dependence on τ_α at both short and large distances. The fraction of slow monomers increases with τ_α from about 35% for $\tau_\alpha \approx 1$ (set A) up to about 60% for $\tau_\alpha \approx 1000$ (set E). Instead, the fraction of fast particles is nearly constant to about 10%. This increased sensitivity to τ_α is also seen in both M-DDC, $C_{\delta u}(r, \tau_\alpha)$, (Fig.2.16, bottom) and the related (large) correlation length $\xi_{\delta u}(\tau_\alpha)$ (Fig.2.17, bottom). We conclude that at long times both the mobility distribution and its (wide) spatial correlation are affected by the slowing down of the structure rearrangement.

Having defined the subsets of nearly immobile and highly mobile monomers, we are in a position to analyze the displacement-displacement correlations between one either fast or immobile monomer and its surroundings. Fig. 2.19 plots the spatial extensions of the direction and the modulus displacement-displacement correlations at short times ($\Theta = t^\star$). It is seen that, with respect to the average (bulk) case, fast monomers exhibit increased dis-

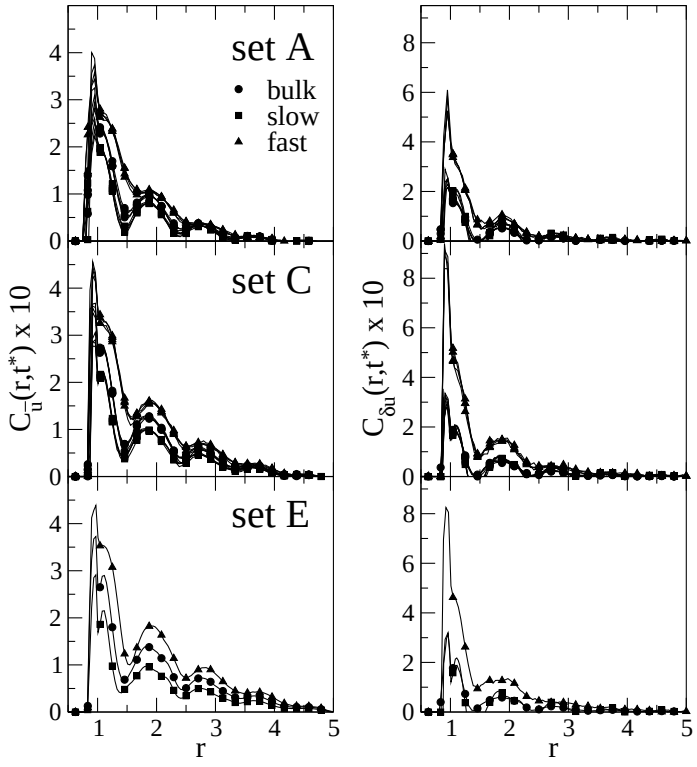

Figure 2.19: Spatial dependence of the correlation of the direction (left) and the modulus (right) of the displacements at the rattling time t^* for the sets of states A, C and E (see Fig.2.3). The average correlation is plotted together with the correlations of the slow and fast fractions.

placement correlations, both in direction and modulus, with the surrounding particles; in the case of modulus correlations, the increase is very strong for pairs of bonded monomers, corresponding to the first peak of the radial distribution function at the bond length $r = b \approx 0.97$. On the other hand, slow particles show a decrease in the correlation of the direction of the displacement over time $\Theta = t^\star$ respect to bulk, whereas no significant difference with the bulk can be observed for the correlation of the modulus.

If one examines the direction correlations of the short-time displacements in more detail (Fig.2.19, left), it is seen that, if the central monomer is slow, D-DDC changes little by slowing down the relaxation. Differently, if the central monomer is fast, D-DDC increases. This provides more insight in the finding drawn by considering bulk D-DDC, (Fig.2.15, top) and the correlation length $\xi_{\vec{u}}(t^\star)$ (Fig.2.17, top) that direction DDC are fairly coupled to the structural relaxation.

As far as the modulus correlations of the short-time displacements are concerned (Fig.2.19, right), it is seen that for states with slow relaxation (set C) fast monomers have larger correlations with bonded ($r \simeq 0.97$) and first-neighbors ($r \simeq 1$) than in A set (fast relaxation). Instead, little difference is

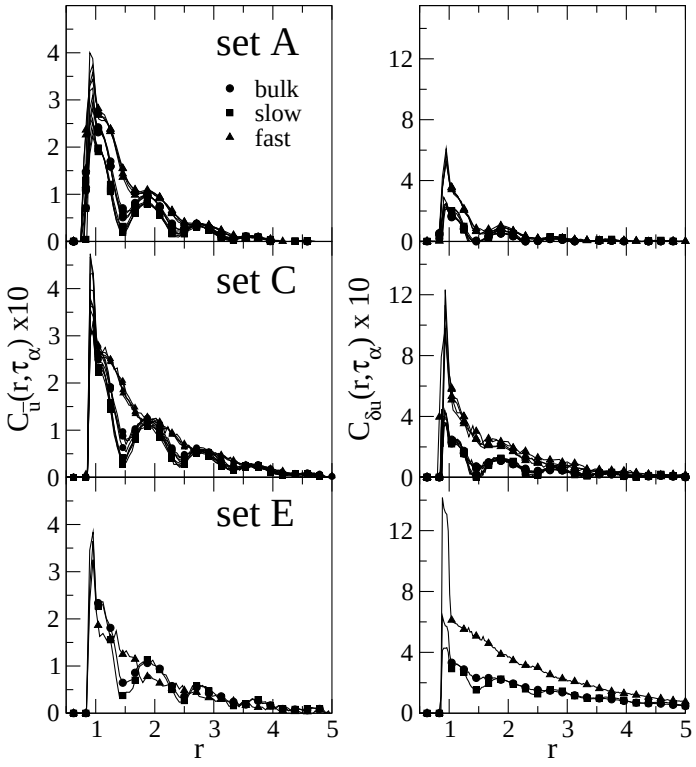

Figure 2.20: Spatial dependence of the correlation of the direction (left) and the modulus (right) of the displacements at τ_α for the sets of states A, C and E (see Fig.2.3). The average correlation is plotted together with the correlations of the slow and fast fractions.

seen at larger distances. Comparing states of C set with states with much slower dynamics (E set) no appreciable differences are seen. M-DDCs of slow monomers with the surroundings are indistinguishable from the bulk case and, as D-DDC of the same kind of monomers, virtually independent on τ_α . This analysis reinforces the conclusion drawn by the consideration of bulk M-DDC, (Fig.2.15, bottom), the correlation length $\xi_{\delta u}(t^\star)$ (Fig.2.17, top) and the mobility distribution that M-DDC are largely independent on the structural relaxation.

Fig.2.20 shows the spatial extension of the correlations of both the direction and the modulus of the displacements within time $\Theta = \tau_\alpha$. Again, the central monomer is taken as highly mobile or nearly immobile and its correlation with monomers at distance r are considered and compared to the bulk (average) behavior. It is seen that both the modulus and the direction correlations of the slow particles differ little from the bulk. Differently, the modulus and the direction correlations of the fast particles show increasing differences from the average behavior. In particular, the decay is almost monotonic, i.e., there is a marked loss of spatial modulation due to the density radial distribution function $g(r)$. A tentative explanation may be given. Remind that, according

Table 2.1: Direction $\xi_{\vec{u}}^{(x)}(\Theta)$ and modulus $\xi_{\delta u}^{(x)}(\Theta)$ correlation lengths for $\Theta = t^*$ and $\Theta = \tau_\alpha$. Bulk ($x = b$), immobile ($x = s$) and fast particles ($x = f$) are considered. The sets of states A, C and E are described in Fig.2.3.

Set	$\Theta = t^*$					
	direction			mobility		
	$\xi_{\vec{u}}^{(b)}$	$\xi_{\vec{u}}^{(s)}/\xi_{\vec{u}}^{(b)}$	$\xi_{\vec{u}}^{(f)}/\xi_{\vec{u}}^{(b)}$	$\xi_{\delta u}^{(b)}$	$\xi_{\delta u}^{(s)}/\xi_{\delta u}^{(b)}$	$\xi_{\delta u}^{(f)}/\xi_{\delta u}^{(b)}$
A	0.70(3)	1.00(8)	1.06(6)	0.44(5)	1.07(9)	0.63(6)
C	0.87(4)	1.03(7)	0.98(6)	0.34(2)	1.1(1)	0.7(1)
E	1.01(4)	1.10(8)	0.96(7)	0.28(4)	0.97(9)	0.62(6)
Set	$\Theta = \tau_\alpha$					
	direction			mobility		
	$\xi_{\vec{u}}^{(b)}$	$\xi_{\vec{u}}^{(s)}/\xi_{\vec{u}}^{(b)}$	$\xi_{\vec{u}}^{(f)}/\xi_{\vec{u}}^{(b)}$	$\xi_{\delta u}^{(b)}$	$\xi_{\delta u}^{(s)}/\xi_{\delta u}^{(b)}$	$\xi_{\delta u}^{(f)}/\xi_{\delta u}^{(b)}$
A	0.70(3)	1.00(8)	1.06(6)	0.44(5)	1.07(9)	0.63(6)
C	0.85(3)	1.05(8)	0.96(4)	1.01(3)	1.10(6)	0.90(5)
E	0.82(2)	1.05(9)	0.99(6)	2.38(4)	1.02(5)	0.86(5)

to the definitions of both $C_{\vec{u}}(r,t)$ and $C_{\delta u}(r,t)$, eqs 2.18, 2.19, r is the *initial* distance between the two monomers before their displacement takes place over a time t. Fast particles perform hopping motion with jump size $\Delta r \sim 1$ at long times [51]. Then, if the total displacement within τ_α is due to a series of jumps, one expects a reduced correlation of both its modulus and direction to the local density at the initial distance r. Notice that the same "smearing" effect is missing or less apparent in slow particles, so that, depending on the relative weight between fast and slow monomers and the relative magnitude of their spatial correlations, it may be present or not in the bulk DDCs.

Table 2.1 compares the correlation lengths $\xi_{\vec{u}}^{(x)}(\Theta)$ and $\xi_{\delta u}^{(x)}(\Theta)$ of the immobile ($x = s$) and fast ($x = f$) monomers to the bulk behavior ($x = b$), where Θ is the time spent during the monomer displacement. We are not aware of similar analysis in other studies on DDCs. First, we note that no changes with τ_α are seen in $\xi_{\vec{u}}^{(x)}(\Theta)$ for fast and slow particles at both $\Theta = t^*$ (see columns 2, 3 top) and $\Theta = \tau_\alpha$ (see columns 2, 3 bottom). Furthermore, one sees that the mobility correlation length of fast monomers is less than the bulk (average) one both at t^* (column 6 top) and τ_α (column 12 top). At long times this reduction is weaker and signals that $\xi_{\vec{u}}^{(f)}(\tau_\alpha)$ markedly increases as $\xi_{\vec{u}}^{(b)}(\tau_\alpha)$ does (column 4 bottom). Differently, mobility correlations of slow monomers exhibit the same spatial extension of bulk monomers on both time scales (columns 5 top and 5 bottom).

2.4 Conclusions

The results of extensive MD simulations of a melt of fully flexible unentangled polymer chain have been presented. In the first part of the chapter, the

correlation between slow relaxation and fast cage dynamics was investigated. The novel results on the scaling are:

1. It does not depend on the specific quantity used to quantify both the relaxation time and the amplitude of the rattling motion.
2. It works on the length scale of the jump-like dynamics.
3. It reaches the time scales of the diffusive regime of the polymer chain, if the chain-length effect is taken into proper account, thus extending to connected systems analogous results known for atomic liquids.

Starting from the analysis of chain diffusion, the violation of the Stokes-Einstein (SE) relation was discussed. It is seen that a crossover occurs between the SE and the fractional Stokes-Einstein (FSE) as the sluggishness of the system increases. The link between the SE violation and the long time dynamic heterogeneity (DH) is discussed. It is seen that the ratio of the quadratic and the linear terms of eq 2.2 with respect to $\langle u^2 \rangle^{-1}$, $\mathcal{R} = \sigma^2_{a^2}/4\overline{a^2}\langle u^2 \rangle$, is a good signature of DH and it allow to locate the onset of the violation with a greater accuracy with respect to the non-gaussian parameter, the common quantity to describe the DH. The fact that, while the maximum of the NGP is reached at times comparable with the structural relaxation, the quantity $\mathcal{R}$ involves only picosecond dynamics, suggests that the long time DH rooted in the fast dynamics.

In the final part of the chapter, displacement-displacement spatial correlations (DCCs) have been discussed in both their scalar and vector character. We investigate two different time scales, i.e., a characteristic vibrational time scale and the structural relaxation time. In both cases the spatial extension of the correlated motion is seen to be influenced by the structure. At short times, the direction correlations are larger and more spatially extended than mobility correlations, i.e., the cage rattling of monomers is directionally correlated in space. On longer time scales mobility correlations are prevailing. The importance of mobility fluctuations increases as the system enters the viscous regime. DCCs were also analyzed in the framework of the dynamical heterogeneity. We show that both mobility and direction correlation length of slow monomers is nearly coincident to the bulk one irrespective of the time scale and relaxation time. One also observes the coincidence of the direction correlation length of the fast monomers with the bulk one whatever the time scale and relaxation time are considered. Instead, the mobility correlation length of fast monomers are seen to be less than the bulk one at both timescales.

Chapter 3

Repulsive reference potentials for molecular liquids

3.1 The research context

A remarkable achievement of our current understanding of atomic simple liquids is the van der Waals picture focussing on the different roles of the repulsive and the attractive forces [72–76]. The short-range harsh repulsion between molecules mainly determine the structure of dense liquids while long-range attractive forces, which vary much more slowly with the distance, provide an essentially uniform attractive background that affects the thermodynamics, but neither the structure nor the dynamics. Working on this premises, Weeks, Chandler and Andersen proposed to split the intermolecular potential into short-ranged repulsive component and longer-ranged component and to treat the latter as a perturbation. This scheme provides a very successful description of static correlations and thermodynamics [75, 77].

The WCA reference was seen to reproduce the liquid dynamics in several systems but exceptions to this were also reported [78–83]. Recently Berthier and Tarjus showed that the dynamics in the viscous regime is not properly reproduced by the WCA reference in a Kob-Andersen binary mixture [84, 85]. The observed differences between WCA and Lennard-Jones models can be due to the truncation of the interaction potential at a distance corresponding to typical interatomic distances, irrespective of the attractive or repulsive nature of the neglected longer-ranged interactions [85, 86].

This drawback has been circumvented by considering another purely repulsive potential , an inverse-power-law (IPL) potential. The IPL scheme relies on the idea that van der Waals-type liquids have a “hidden" scale invariance, which is manifested in the appearance of strong correlation between the potential energy U and the virial W, i.e. the configurational part of the pressure [87–94]. In this regard IPL potential exhibits perfect correlation between U and

W, $W = (n/3)U$ where n is the exponent of the potential. Strongly correlating liquids are liquids that have $R \leq 0.9$, where R is the correlation coefficient of the equilibrium fluctuations of the potential energy and virial. Strongly correlation liquids include the van der Waals and metallic liquids, but neither covalent or hydrogen-bonded liquids nor strongly ionic liquids, where competing interactions tend to break strong UW correlations [89–91]. In this framework, Pedersen *et al.* showed that the pair structure and especially the dynamics of the binary LJ mixture, a strongly correlating system, in the viscous regime can be very well reproduced by replacing the LJ pair potential by an IPL , with an exponent taken from the UW correlations [95]. More recently, it was shown that the same procedure can be applied also to a single component Buckingham liquids in spite of his non-IPL repulsion (the Buckingham potential has an exponential repulsive term, while the attractive part is given by a power law) [96].

Interestingly, up to now, the IPL picture has been tested only in atomic systems. Indeed the idea that the attractive forces play a minor role is based on the fact that in the isotropic environment of a dense liquid the vector sum of the attractive forces on a given particle essentially cancels in most typical configurations [74]. Differently, in microscopically non-isotropic liquids attractive forces do not cancel by symmetry and both attractive and repulsive forces have important effects over comparable length scales of order the molecular size [97]. Model linear polymers offer an interesting situation in that it has been shown that the fast jump dynamics of monomers takes place in sites with aspherical arrangement of surrounding monomers [98–100]. These aspherical sites are very soft, i.e., with small, positive elastic local module, prone to plastic failure and have a large vibration amplitude, as indicated by the local Debye-Waller (DW) factor [101]. Aspherical sites are also found in side-chain polymers [102].

3.2 Models

Two different coarse-grained model of linear polymer chain are considered. In the first model, the rigid bonded chain (RB), bonded monomers are connected by a rigid bond of fixed length. In the second model, the semi-rigid bonded chain (SB), bonded monomers interact with a potential which is the sum of the finitely extendible nonlinear elastic (FENE) potential and the Lennard-Jones potential, resulting in a fluctuation of a few percent in the bond length. In both the models nonbonded monomers interact via the Lennard-Jones potential (LJ); the potential is cut at $r_{cut}^{(LJ)} = 2.5\sigma$ and shifted:

$$\begin{aligned} v^{(LJ)}(r) &= \epsilon \left[\left(\frac{\sigma^*}{r} \right)^{12} - 2 \left(\frac{\sigma^*}{r} \right)^{6} \right] + v_{cut}^{(LJ)} \qquad \text{for } r \leq r_{cut}^{(LJ)} \\ &= 0 \qquad \text{for } r > r_{cut}^{(LJ)} \end{aligned} \tag{3.1}$$

where r is the monomer-monomer distance, $\sigma^* = 2^{1/6}\sigma$ and $v_{cut}^{(LJ)}$ is chosen to ensure $v^{(LJ)}(r) = 0$ at $r = r_{cut}^{(LJ)} = 2.5\sigma$.

The structure and dynamics of LJ chains, both rigid bonded (RB-LJ) and semi-rigid bonded (SB-LJ), was compared to that of models interacting with two different types of repulsive potential. First the inverse-power-law (IPL) potential is considered:

$$\begin{aligned} v^{(IPL)}(r) &= A\left(\frac{\sigma}{r}\right)^n + v_{cut}^{(IPL)} \qquad \text{for } r \le r_{cut}^{(IPL)} \\ &= 0 \qquad \text{for } r > r_{cut}^{(IPL)} \end{aligned} \tag{3.2}$$

where $r_{cut}^{(IPL)} = r_{cut}^{(LJ)} = 2.5\sigma$ and the amplitude A and the exponent n are two adjustable parameters. A modified version of the well-known Weeks-Chandler-Anderson potential (mWCA) was also considered:

$$\begin{aligned} v^{(mWCA)}(r) &= A\epsilon\left[\left(\frac{\sigma^*}{r}\right)^{12} - 2\left(\frac{\sigma^*}{r}\right)^{6}\right] + v_{cut}^{(mWCA)} \qquad \text{for } r \le r_{cut}^{(mWCA)} \\ &= 0 \qquad \text{for } r > r_{cut}^{(mWCA)} \end{aligned} \tag{3.3}$$

where the potential is cut and shifted at $r_{cut}^{(mWCA)} = \sigma^* = 2^{1/6}$, the minimum of the LJ potential. For the mWCA potential, the amplitude A is the only adjustable parameter. Summarizing, the following systems were considered: LJ rigid bonded (RB-LJ) and semi-rigid bonded (SR-LJ) chains, IPL rigid bonded (RB-IPL) and semi-rigid bonded (SR-IPL) chains and mWCA rigid bonded (RB-mWCA) and semi-rigid bonded (SR-mWCA) chains.

We performed MD simulations in the NVE ensemble, after equilibration in the NVT ensemble. The system has $N = 2000$ monomers in all cases, but $M = 3$, where $N = 2001$. All the polymer data are in reduced units: length in units of σ, temperature in units of ϵ/k_B and time in units of $\sigma(\mu/\epsilon)^{1/2}$, where μ is the monomer mass. We set $\mu = k_B = 1$.

3.3 Results and discussion

3.3.1 Fixing the potentials

The inverse-power-law potential (IPL) defined in eq 3.2 has two adjustable parameters: the exponent n and the amplitude A. To fix the value of the exponent, a property of IPL potentials is used [95]. In the case of pair potentials, the virial W, i.e., the configurational contribution to pressure, is given:

$$W = -\frac{1}{3}\sum_{i>j} w(|\mathbf{r}_i - \mathbf{r}_j|) \tag{3.4}$$

where $\mathbf{r}_k$ is the position of k-th particle and $w(r) = rv'(r)$ being v' the derivative of the pair potential $v(r)$. For an IPL pair potential $v(r) \propto r^{-n}$, we have $w(r) = -nv(r)$ and a relation between virial W and potential energy $U = \sum_{i>j} v(|\mathbf{r}_i - \mathbf{r}_j|)$ holds exactly:

$$W = \frac{n}{3}U \tag{3.5}$$

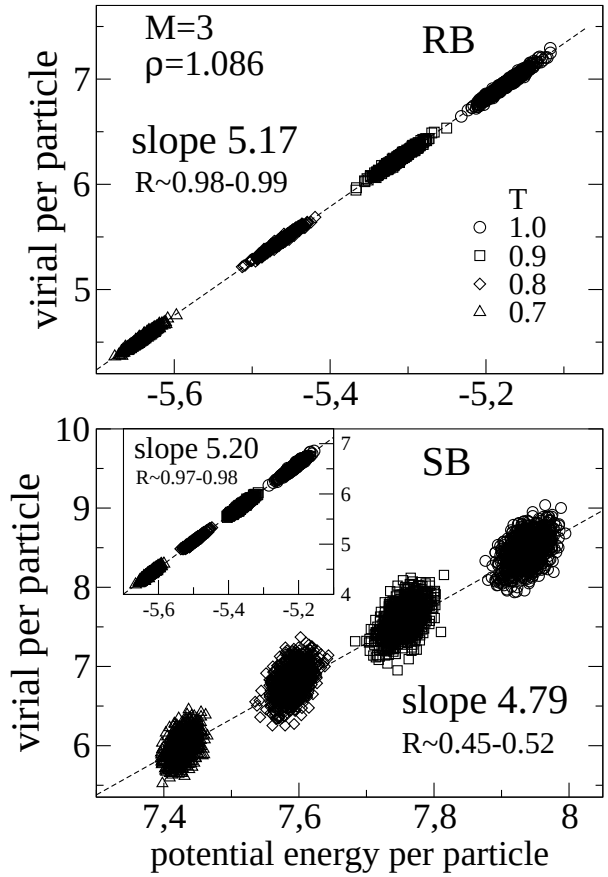

Figure 3.1: Scatter plot of the virial and configurational energy per particle for Lennard-Jones (LJ) Rigid Bonded (top panel) and Semi-rigid bonded (bottom panel) chains, with chain length $M = 3$, for state points with the same density. RB chains show strong correlation between virial, correlation coefficient $R \sim 0.98 - 0.99$, and potential energy and the IPL exponent in eq 3.2 is estimated to $n = 3 \times 5.17 = 15.51$ by evaluating the slope of the scatter plot. For SB chains the correlation between virial and potential energy is weak, $R \sim 0.5$. Strong correlation, $R \sim 0.97 - 0.98$, is recovered if the bonding contribution is neglected (inset of bottom panel) and the IPL exponent is estimated to $n = 3 \times 5.20 = 15.60$.

In IPL systems, potential energy and virial are perfectly correlated, with a "slope" given by $n/3$.

Figure 3.1 shows a correlation plot of the instantaneous virial and potential energy fluctuations of Lennard-Jones (LJ) RB and SB chains, with chain length $M = 3$, at fixed density $\rho = 1.086$. The degree of correlation can be measured via the correlation coefficient R:

$$R = \frac{\langle \Delta W \rangle \langle \Delta U \rangle}{\sqrt{\langle (\Delta W)^2 \rangle} \sqrt{\langle (\Delta U)^2 \rangle}} \tag{3.6}$$

where Δ denotes deviation from the average value of the given quantity and

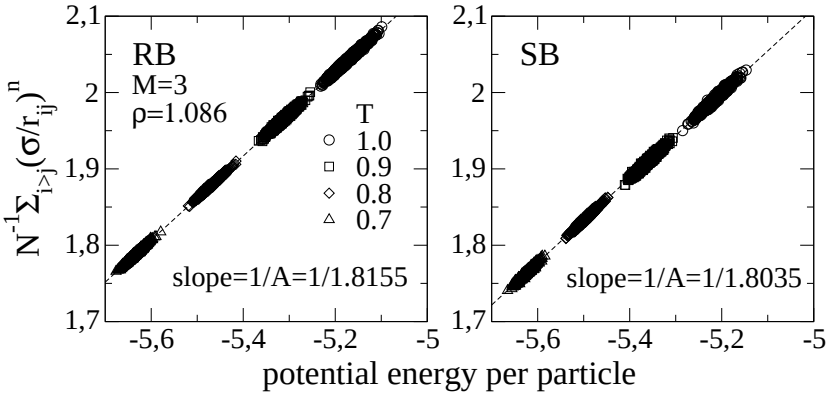

Figure 3.2: Scatter plot of $N^{-1}\sum_{i>j}(\sigma/r_{ij})^n$, with n defined in Figure 3.1, and potential energy per particle for RB-LJ (left panel) and SB-LJ (right panel) chains, with chain length $M = 3$, for state points with the same density. The IPL amplitude in eq 3.2, estimated from the slope of the scatter plot, is $A = 1.8155$ for RB chains and $A = 1.8035$ for SB chains.

$\langle ... \rangle$ denotes thermal averages. In the case of RB chains (top panel of Figure 3.1) the correlation coefficient is very high $R \sim 0.98 - 0.99$ ($R = 1$ for IPL potentials). The slope γ of the best fit line is 5.17. As in previous works [95, 103] we fix the exponent n of the IPL potential as $n = 3 \times 5.17 = 15.51$.

SB chains, on the contrary, show low correlation (bottom panel of Figure 3.1), $R \sim 0.45 - 0.5$ depending on the state point. The lack of correlation is the result of the competition between bonding and Lennard-Jones interactions [89, 104]. This is not the case of RB chains where a bonding potential is not present. The absence of strong $U - W$ correlations makes impossible to use the slope γ of the best fit line to determine the IPL exponent. Note also that the best fit slope γ does not represent the direction of greatest variance of the $U - W$ ellipsoids, which defines an additional slope γ_2.

Strong $U - W$ correlation, $R \sim 0.97 - 0.98$, is recovered even for SB chains if only the nonbonding interactions, the LJ interaction, is included in the calculation of both virial and potential energy (bottom inset of Figure 3.1). Therefore the IPL exponent can be fixed as $n = 3 \times 5.20 = 15.60$, being 5.20 the slope γ of the best fit line.

Once the exponent n in eq 3.2 is determined, a single adjustable parameter, the pre factor A, is left in the IPL potential. As in [95], A is fixed by plotting the fluctuations of the LJ potential versus the quantity $\sum_{i>j}\left(\sigma/r_{ij}\right)^n$, computed on configurations belonging to LJ simulations (see Figure 3.2). This results in $A = 1.8155$ for RB chains and $A = 1.8035$ for SB chains.

Finally, the modified Weeks-Chandler-Anderson potential, mWCA potential, has only one adjustable parameter, the pre factor A, which is fixed by plotting the fluctuations of the LJ potential versus $\sum_{i>j}\epsilon\left[(\sigma^*/r_{ij})^{12} - 2(\sigma^*/r_{ij})^6\right]$, cut at $r_{cut} = 2^{1/6}$, computed on configurations belonging to LJ simulations (see Figure 3.3). This results in $A = 1.135$ for RB chains and $A = 1.144$ for SB chains.

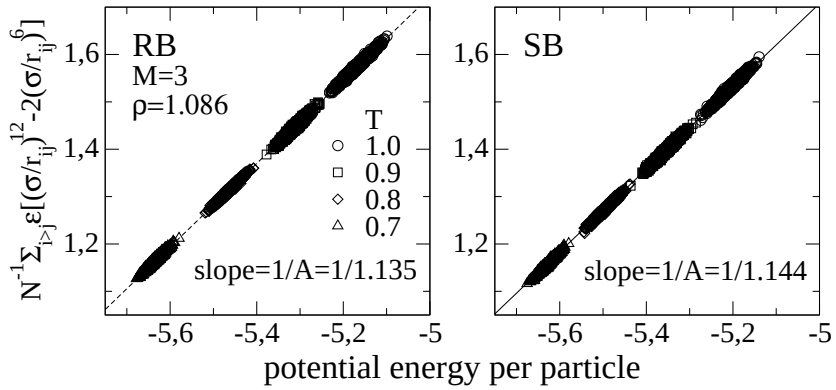

Figure 3.3: Scatter plot of $N^{-1}\sum_{i>j}\epsilon\left[(\sigma^*/r_{ij})^{12}-2(\sigma^*/r_{ij})^6\right]$, with a cut-off distance $r_{cut}=\sigma^*=2^{1/6}$, and potential energy per particle for RB-LJ (left panel) and SB-LJ (right panel) chains, with chain length $M=3$, for state points with the same density. The mWCA amplitude in eq 3.3, estimated from the slope of the scatter plot, is $A=1.135$ for RB chains and $A=1.144$ for SB chains.

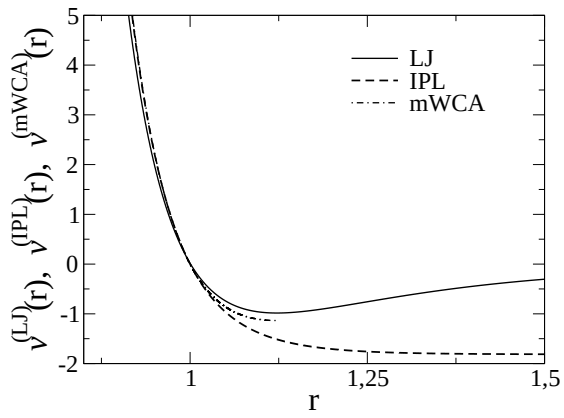

Figure 3.4: Plot of the different monomer-monomer potential in the case of rigid bonded chains: LJ potential (full line) defined in eq 3.1, IPL potential (dashed line), eq 3.2, with $n=15.51$ and $A=1.8155$, and mWCA potential (dash-dotted line), eq 3.3, with $A=1.135$. The curves are vertically shifted to coincide at $r=1$.

3.3.2 Static correlations

First the structure of the three model, as described by the pair correlation function $g(r)$, is considered. Figure 3.5 shows the $g(r)$ of the LJ, IPL and mWCA with both rigid and semi-rigid bond, for a given state point. The agreement between the three model is very good confirming that attraction, which is absent in both IPL and mWCA, does not play a relevant role in determining the structure of liquids [75]. Moreover in the case of SB chains, attraction does not affect also the chain connectivity, as can be seen by the coincidence of the distributions of bond length (see the inset of Figure 3.5).

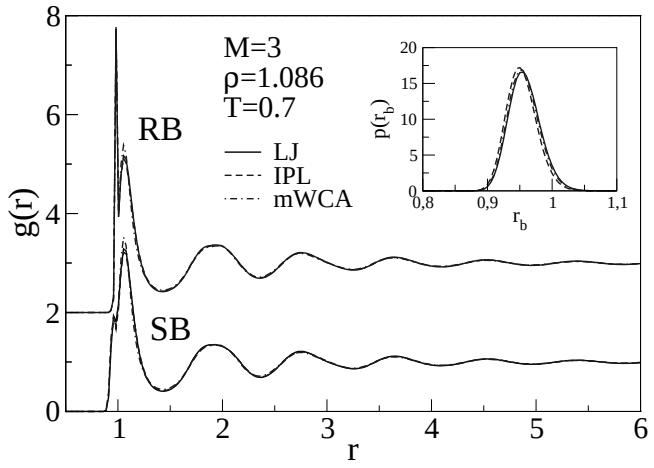

Figure 3.5: Pair correlation function $g(r)$ of the LJ, IPL and mWCA chains with rigid bond RB and semi-rigid bond SB at a given state point. The different curves are vertically shifted, for clarity. Inset: bond distribution of the LJ, IPL and mWCA SB chains for the same state point of the main panel.

In order to get further insight into the capability of the repulsive models to reproduce the statics of the LJ model, we consider the inherent structures (IS), i.e., the configurations obtained from the real ones by minimizing the potential energy in the configuration space (see Appendix A for full details on how IS are computed). This is motivated by the fact at non-zero temperature monomers vibrate around their equilibrium positions and such fast movements may obscure specific arrangements of monomers. Figure 3.6 shows the inherent pair correlation function $g^{(IS)}(r)$ of the three models of potentials. Note that deviations become apparent if inherent configurations are considered. In particular, the first peak of the $g^{(IS)}$ is significantly more pronounced in the mWCA model with respect to the LJ model; this strange effect could be due to the truncation of the monomer-monomer interaction potential at a distance corresponding to typical interatomic distances. On the contrary, a close inspection of Figure 3.6 reveals that the first peak in the IPL model is slightly less pronounced with respect to the LJ model suggesting that the latter is effectively more supercooled. Deviations are also present in the second neighbor shell (insets of Figure 3.6), which is much more detailed in inherent structures. Having removed the vibrational cage rattling, in LJ chains the second peak split in three sub-peaks. The side sub-peaks are well-known signature of local icosahedral order in atomic LJ liquids [105]. The central sub-peak is characteristic of multicomponent systems [106] and of the present molecular system and it is assigned to linear trimers of two bonded and one not bonded monomers. Even in the mWCA model the second peak splitting is present but it appears less detailed with respect to LJ and IPL models.

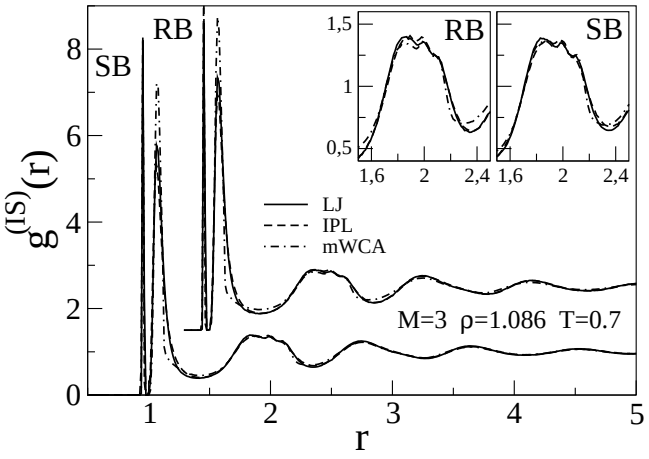

Figure 3.6: Inherent pair correlation function $g^{(IS)}(r)$ of the LJ, IPL and mWCA chains with rigid bond RB and semi-rigid bond SB at a given state point. The different curves are horizontally and vertically shifted, for clarity. Insets: magnification of $g^{(IS)}(r)$ in the region of the second neighbor shell.

3.3.3 Dynamic correlations

Here the results concerning the dynamics of the three models are presented. First we consider the self intermediate scattering function (ISF):

$$F_s(q,t) = N^{-1}\langle \sum_i \exp\{i\mathbf{q}\,[\mathbf{r}_i(t) - \mathbf{r}_i(0)]\}\rangle$$

with $q = 7.35$ corresponding to the maximum of the static structure factor. Figure 3.7 shows ISF curves for RB and SB chains with the three considered potentials. We observe that, unlike the static, the absence of attraction between monomers strongly influences the dynamics of the system, regardless of the chain connectivity. In particular, at the highest temperature the agreement between mWCA and LJ is not perfect but the differences are quite small. As the temperature decreases, deviations increase abruptly (not shown) and the effect become dramatic: at the lowest temperature, relaxation in mWCA models is about two orders of magnitude faster than that in LJ models. These findings agree with recent works on binary mixture [84, 85, 95] where it is seen that, at low temperatures, the dynamics in WCA models is much faster than in LJ models Moreover, our results suggest that considering mWCA models, i.e.,WCA with a scaling of the amplitude, only slightly improves the agreement at low temperatures.

Now we turn to the inverse-power-law IPL models. Figure 3.7 strikingly shows how the small differences in the relaxation dynamics of the high temperature IPL and LJ models become an important effect at low temperatures. Note that at the highest temperature ($T = 1.0$) the dynamics in IPL and mWCA models is almost equivalent. At the lowest temperatures, the deviations between IPL and LJ relaxation is less than an order of magnitude, with

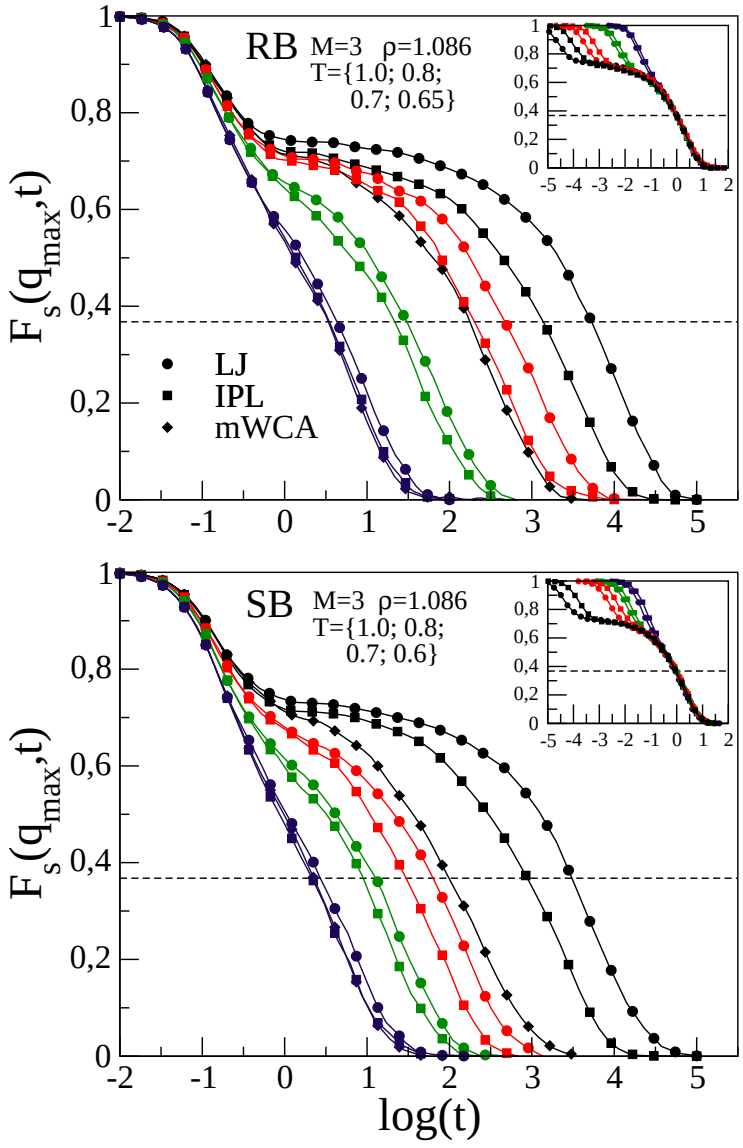

Figure 3.7: Comparison of the incoherent intermediate scattering function $F_s(q_{max}, t)$ for the LJ, IPL and mWCA chains with rigid bond (top panel) and semi-rigid bond (bottom panel) for state points with different temperature along the $\rho = 1.086$ isochore. In both RB and SB chains, the IPL models perform better than the mWCA ones in reproducing the relaxation dynamics of the LJ models. Dashed lines marks the definition of the structural relaxation time via $F_s(q_{max}, \tau_\alpha) = 1/e$. Insets: long time collapse of the ISF curves by rescaling the time.

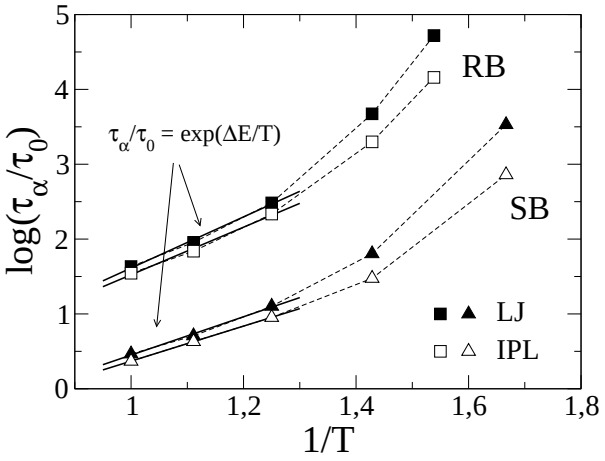

Figure 3.8: Temperature dependence of the structural relaxation time τ_α, defined via $F_s(q_{max}, \tau_\alpha) = 1/e$, for the LJ and IPL chains with rigid and semi-rigid bond for state points with different temperature along the $\rho = 1.086$ isochore. We set $\tau_0 = 10^{-1}$ for RB chains and $\tau_0 = 1$ for SB chains, for clarity. Solid lines are the best fits with the Arrhenius equation $\log(\tau_\alpha/\tau_0) = \Delta E/T$ in the high temperature region.

the former being faster. From this, it is apparent that the IPL potential constitutes a better reference for LJ potential with respect to the mWCA. However for the investigated models, IPL is not a reference potential as good as one would expect from earlier work on binary mixture [95, 103].

We want to point out here that deviations in the relaxation dynamics between IPL and LJ models seem not to depend on the nature of chain connectivity, i.e., if rigid or sem-rigid bond are present. Remind one of the results in section 3.3.1: RB chains are strongly correlating systems (correlation coefficient between virial and potential energy $R > 0.9$)whereas SB chains are not. What we find here is that the condition of being or not being strongly correlating does not affect significantly the IPL reference potential.

From the time decay of the ISF, we define the structural relaxation time via $F_s(q_{max}, \tau_\alpha) = 1/e$. Figure 3.8 shows the temperature dependence of τ_α for LJ and IPL models of RB and SB chains. The figure clearly illustrates the differences in the T-driven slow-down of the LJ and IPL models. At high temperature, the T-dependence of τ_α is well described by the Arrhenius equation $\log(\tau_\alpha/\tau_0) = \Delta E/T$ with a constant energy barrier ΔE (see Figure 3.8). We found that, for both the RB and the SB models, the energy barriers of the IPL models are slightly smaller than the LJ ones.

To conclude the analysis of the relaxation dynamics, we consider the rotational relaxation dynamics described by the correlation function of the end-to-end vector defined as:

$$C_{ee}(t) = \frac{1}{N_p R_{ee}^2} \sum_{i=1}^{N_p} \langle \mathbf{R}_i(t) \cdot \mathbf{R}_i(0) \rangle \tag{3.7}$$

where N_p is the chain number, $\mathbf{R}_i(t)$ is the vector joining the first and the last

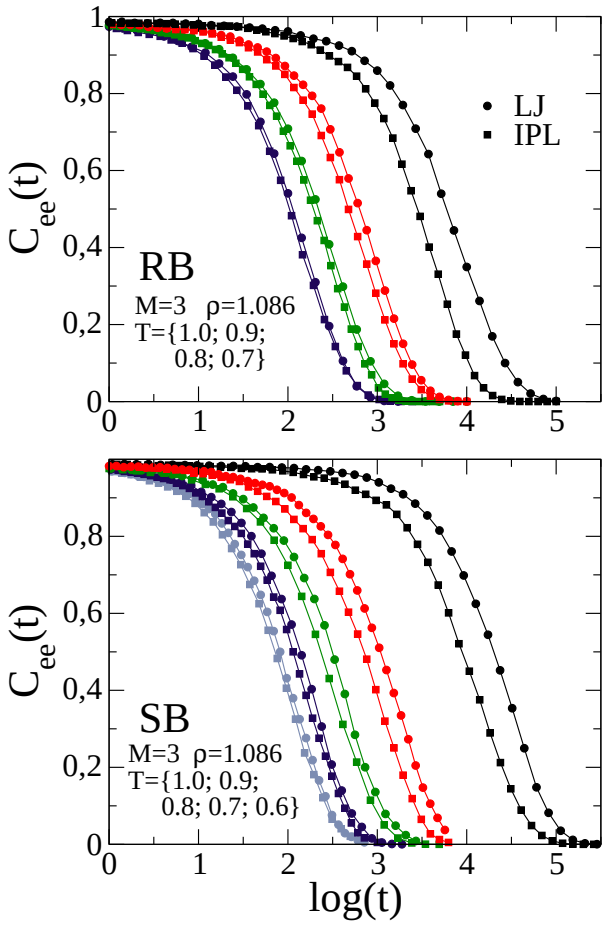

Figure 3.9: Correlation function of the end-to-end vector $C_{ee}(t)$ for the LJ, IPL and mWCA chains with rigid bond (top panel) and semi-rigid bond (bottom panel) for state points with different temperature along the $\rho = 1.086$ isochore.

monomer of the i-th chain and R^2_{ee} is defined:

$$R^2_{ee} = \frac{1}{N_p} \sum_{i=1}^{N_p} ||\mathbf{R}_i||^2 \tag{3.8}$$

Differently from the ISF, that has a single-particle character, the $C_{ee}(t)$ monitors relaxation of the whole chain so it brings a collective information on the relaxation.

In Figure 3.9 the C_{ee} curves for LJ and IPL models of RB and SB chains are shown. We focus on the IPL models since they are seen to perform better than the mWCA models. Again diverging behavior is observed between LJ and IPL models, with the latter being faster. For a given temperature, the deviations in the rotational relaxation of LJ and IPL are comparable to the deviations observed in structural relaxation (ISF curves).

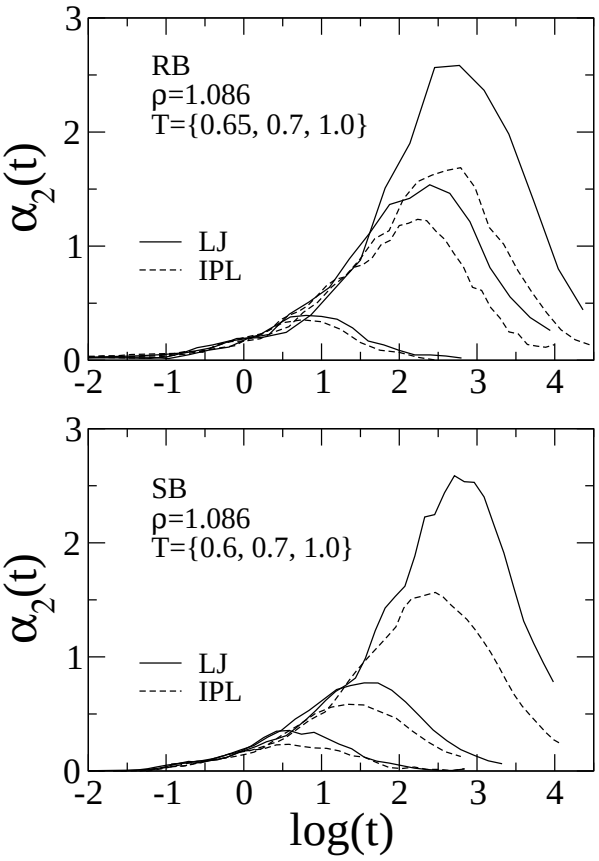

Figure 3.10: Time dependence of the non-gaussian parameter α_2 for the LJ and IPL chains with rigid (top panel) and semi-rigid bond (bottom panel) for state points with different temperature along the $\rho = 1.086$ isochore.

In this framework, the analysis of the IPL and LJ models was extended to other dynamical quantities, such as the mean square displacement, the intermediate scattering function at different wave vectors and the bond-bond correlations, that we do not show here. The common message of all these comparisons is that the dynamics in the LJ models is increasingly slower than in the IPL model. Finally, in Figure 3.10 the time dependence of the non-gaussian parameter $\alpha_2(t)$ is shown for state points with different temperature. The finding, that the dynamics in the IPL models, irrespective on the type of bond, is less heterogeneous (smaller α_2 at long time) then in the LJ ones, agrees with the previous results on dynamic correlations.

Up to this point, we have shown that the absence of attraction strongly influences both the single monomers and the chain dynamics. Notwithstanding that the IPL reference is seen to better perform than the mWCA, deviation between LJ and IPL models become apparent as the temperature is lowered. However, at the lowest temperature that we reach, deviations are not so large (less than half a decade) to reject the idea that inverse-power-law potential is a

good reference for Lennard-Jones potential, in the present molecular systems.

To better explore the low-temperature viscous regime, we operate in a different way. Starting from an equilibrium configuration with temperature $T = 1.0$, a stepwise cooling is carried out, using cooling rate $\Gamma = 10^{-5}$ (in MD units), defined as $\Gamma = \Delta T/\Delta t$ where ΔT is the cooling step and Δt the duration in MD time units.

In the following analysis, decamers , i.e., chain composed of ten monomers, are considered. This because longer chains have a lower tendency to crystallize with respect to short chains and because of this lower temperature can be reached without problems. The exponent n and the amplitude A of the IPL potential, eq 3.2, are fixed with the procedure that we described in section 3.3.1, and using equilibrium configurations with temperatures $T = 1.0, 0.9, 0.8, 0.7$. This results in $n = 15,87$ and $A = 1.7595$. Note that the moving from $M = 3$ to $M = 10$, the variation in the IPL exponent is very small.

Figure 3.11 shows ISF curves for LJ and IPL models of semi-rigid chains for state points with different temperature along the $\rho = 1.086$ isochore, created by step wisely cooling from $T = 1.0$. First, by comparison with the equilibrium simulations, we observe that the system fall-out of equilibrium at $T \leq 0.7$ as it does not have enough time to equilibrate at the given temperature. Hence even in the out-of-equilibrium regime, deviations in the relaxation dynamics increase as the temperature is lowered. At the lowest temperature reached, the relaxation in the IPL model is about six times faster than the LJ model. This value represent a lower limit as we expect that deviations in equilibrium simulations would be larger (due to the fact that dynamics in LJ model is slower than in IPL, the latter is faster in responding to changes in temperature and it results closer to the equilibrium condition).

Now we show that it is possible to extend our results up to the glass transition. In Figure 3.12 a correlation plot of the structural relaxation time for LJ and IPL models, $\tau_\alpha^{(LJ)}$ and $\tau_\alpha^{(IPL)}$ respectively, is shown. In the figure we include both the equilibrium and the out-of-equilibrium simulations, previously shown in Figures3.7 and 3.11 respectively. The existence of a power-law relation connecting $\tau_\alpha^{(LJ)}$ and $\tau_\alpha^{(IPL)}$ in the present model is apparent as the data fall along a straight line in the $\log - \log$ plot. The best-fit line results:

$$\log\left(\tau_\alpha^{(IPL)}/\tau_0\right) = a + b\log\left(\tau_\alpha^{(LJ)}/\tau_0\right) \tag{3.9}$$

where $a = -0.029$ and $b = 0.87$.
According to eq 3.9, the ratio $\tau_\alpha^{(LJ)}/\tau_\alpha^{(IPL)}$ grows rather slowly as a power law $(\tau_\alpha^{(LJ)})^{0.13}$. This explain the small deviations observed for the time scales accessible to MD simulations.

If one assumes that eq 3.9 applies even at lower temperatures, it is possible to make a prediction of the deviations between LJ and IPL models at the glass transition (GT). Remind that the GT relaxation time $\tau_{\alpha g} = 10^2\, s$ in laboratory units is equivalent to $10^{13} - 10^{14}$ in our MD units. So at the GT of the LJ model, we have $\log(\tau_\alpha^{(LJ)}/\tau_\alpha^{(IPL)}) \approx 1.8$, i.e., the IPL model is about two order of magnitude faster than the LJ model.

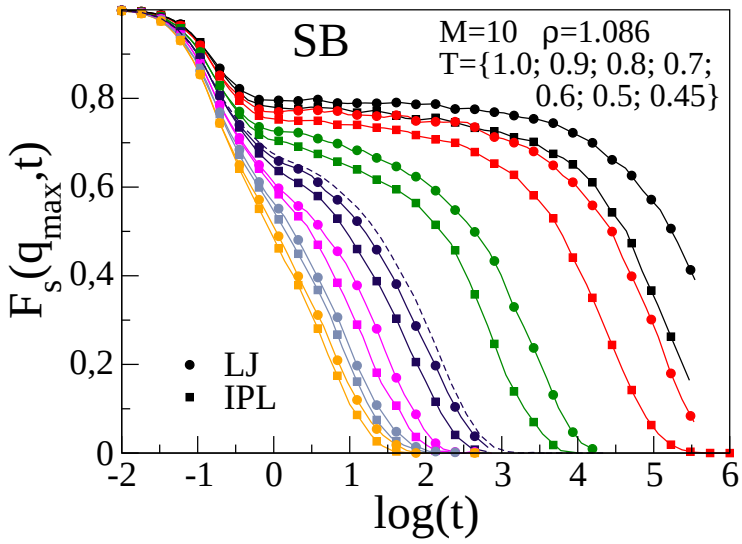

Figure 3.11: Comparison of the incoherent intermediate scattering function $F_s(q_{max}, t)$ for the LJ and IPL chains with semi-rigid bond for state points with different temperature along the $\rho = 1.086$ isochore, explored by step wisely cooling the systems starting from an equilibrium configuration with $T = 1.0$. Dashed line is the corresponding equilibrium simulation of the LJ chains at $T = 0.7$. Even in out-of-equilibrium simulations, the relaxation dynamics in the IPL and LJ models show increasing deviations.

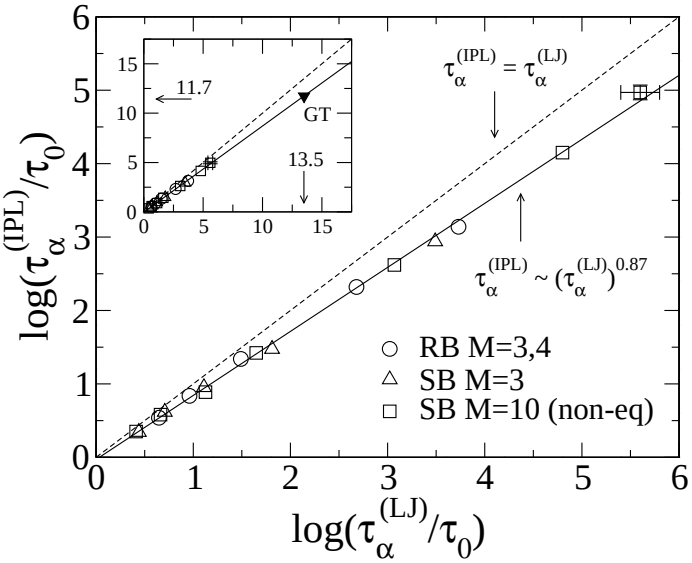

Figure 3.12: Correlation plot of $\tau_\alpha^{(LJ)}$ and $\tau_\alpha^{(IPL)}$, the structural relaxation times of the LJ and IPL models respectively, for the states in Figure 3.7 and Figure 3.11. Dashed line is $\tau_\alpha^{(IPL)} = \tau_\alpha^{(LJ)}$. Full line is the best-fit line $\log(\tau_\alpha^{(IPL)}/\tau_0) = a + b\log(\tau_\alpha^{(LJ)}/\tau_0)$ with $a = -0.029$ and $b = 0.87$. Inset: extrapolation of the best-fit relation showing that, at the glass transition (GT) of the LJ model, IPL is about two order of magnitude faster.

3.3.4 The issue of virial-potential correlations

In section 3.3.1 the subject of the correlations between the potential energy U and the virial W was introduced. Here we briefly resume the discussion.

In Figure 3.13, we plot the instantaneous fluctuations of the potential energy and virial for the LJ chains with rigid (top panel) and semi-rigid bond (bottom panel). As mentioned above, while rigid bonded chains show strong correlations the semi-rigid chains does not, due to the competition between monomer-monomer interaction and bonding interaction. It is puzzling, in our opinion, that if one replace a rigid bond with a more physical semi-rigid one, resulting in a fluctuation of bond length of a few percent, the system loses its status of strongly correlating (correlation coefficient $R \leq 0.9$). Only if the bonding interaction is ignored in the computation of both the virial and the potential energy, strong correlation is recovered in the SB model. Note that in the equations of motion, that determine the dynamics of the monomers, all the interactions are included. Furthermore, in the case of RB models we should have included in the virial the contribution of the constraints [107]

$$W_{con} = \frac{1}{3} \sum_{\alpha=1}^{N} \mathbf{r}_i \cdot \mathbf{G}_i \tag{3.10}$$

where $\mathbf{G}_i$ is the constraint force, $\mathbf{G}_i = \sum_{\alpha=1}^{G} \lambda^\alpha \nabla_{\mathbf{r}_i} \psi^\alpha$, $\psi^\alpha(\mathbf{r}^N)$ are the constraints and λ^α the Lagrangian multipliers. The potential energy has no contribution from the constraints. It is known that if W_{con} is included in the virial, correlation is destroyed even in the RB model [96].

In section 3.3.1 the optimal exponent n for the IPL models was drawn by the slope γ of the correlation curve between the instantaneous virial per particle $W(t)/N$ and potential energy per particle $U(t)/N$. Additional insight is provided by considering the distribution of the instantaneous exponent

$$\Gamma(t) = \frac{W(t) - \langle W \rangle}{U(t) - \langle U \rangle} \tag{3.11}$$

where $\langle ... \rangle$ denote the equilibrium average. Since both $\Delta W(t) = W(t) - \langle W \rangle$ and $\Delta U(t) = U(t) - \langle U \rangle$ are normal variates, $\Gamma(t)$ is a Cauchy variate with Lorentz distribution [108], namely

$$p_C(\Gamma) = \frac{b}{\pi \left(\Gamma - a\right)^2 + b^2} \tag{3.12}$$

with

$$a = R \frac{\langle [\Delta W(t)]^2 \rangle^{1/2}}{\langle [\Delta U(t)]^2 \rangle^{1/2}} \tag{3.13}$$

$$b = \frac{\langle [\Delta W(t)]^2 \rangle^{1/2}}{\langle [\Delta U(t)]^2 \rangle^{1/2}} \sqrt{1 - R^2} \tag{3.14}$$

Note that $a = \gamma_1 = \left(\partial W / \partial U\right)_\rho$ [92]. Figure 3.14 plots $p(\Gamma)$ for the RB model. It is indistinguishable from $p_C(\Gamma)$ with $a = \gamma$. Note that $p_C = \delta(\Gamma - a)$ with

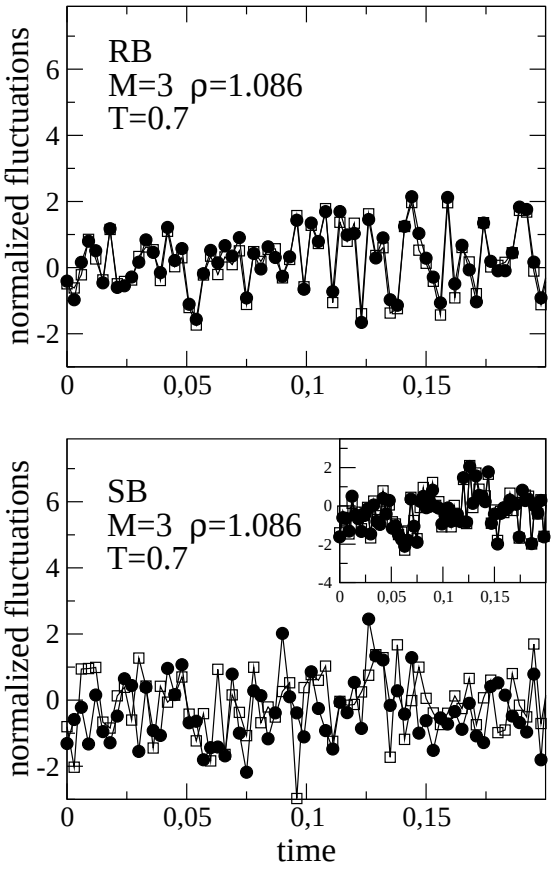

Figure 3.13: Fluctuations of the potential energy U (●) and virial W (□) for the LJ chains with rigid (top panel) and semi-rigid bond (bottom panel) at density $\rho = 1.086$ and temperature $T = 0.7$. A strong correlation between U and W is seen in the RB system but not in the SB. Strong correlation is found in the SB system if the bonding interaction is neglected (inset of bottom panel).

$R = 1$. However, even in the presence of very strong correlations $R > 0.9$, $p(\Gamma) \simeq p_C(\Gamma)$ has long tails (see the inset of Figure 3.14). Remind also that $p_C(\Gamma)$ has infinite average and variance. This spread of the instantaneous slope values signals the difficulty by the inverse-power-law to account for the dynamical states resulting by the Lennard-Jones interaction potential. A closer inspection of Figure 3.14) reveals that, as the temperature is lowered, the width of the distribution slightly increases and consequently increases the presence of events characterized by a very large positive or negative instantaneous slope. These tail event, may be responsible for the slow diverging behavior in the dynamics of the LJ and IPL models that we found in simulations.

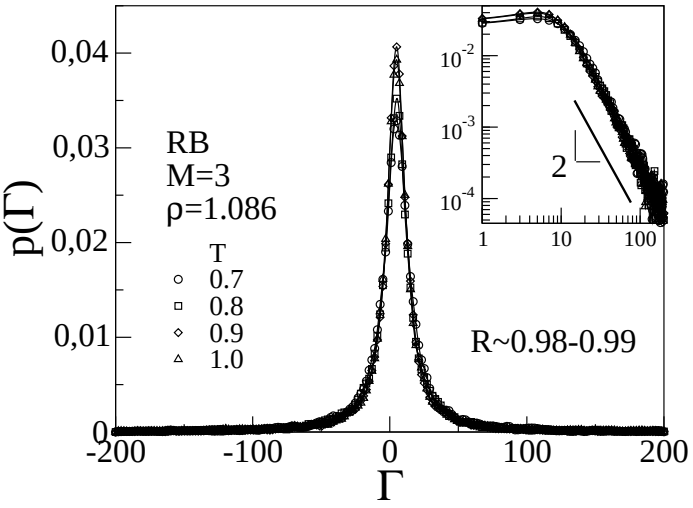

Figure 3.14: Distribution of the instantaneous slope $\Gamma(t)$ of the virial and potential energy fluctuations for state points with different temperature of the rigid bonded model of linear chain. $p(\Gamma)$ indistinguishable from the Lorentz distribution $p_C(\Gamma)$ of eq 3.12. Inset: log – log plot, which shows the slow power-law decay of $p(\Gamma)$. Strong virial-potential correlations are signaled the high values of the correlation coefficient R.

3.4 Conclusions and open questions

Here we consider two standard models of fully flexible linear polymers with M monomers linked by either partially semi-rigid (SB) or rigid (RB) bonds and interacting via the Lennard-Jones (LJ) non-directional potential. To investigate the role of the attractive forces between non-bonded monomers, the LJ interacting potential is replaced by two kind of repulsive potentials, a modified Weeks-Chandler-Andersen (mWCA) form and an inverse power law (IPL). Both of them capture the structure of the LJ liquid, as described by the pair correlation function $g(r)$. Deviations in the static correlations of the three models become apparent if the inherent structures, i.e., the configurations obtained by minimizing the potential energy, are considered. Then via equilibrium NVE simulations, we compare the dynamic correlations, in the form of the intermediate scattering function and the end-to-end correlation function. The viscous slowing down of the three systems is found quantitatively different. Despite the IPL models are seen to significantly better perform than the mWCA ones, its temperature dependence of the relaxation shows a diverging behavior with respect to the LJ models. This effect is observed even in low-temperature, out-of-equilibrium NVE simulations. Extrapolating up to the glass transition, the IPL models is expected to be less than two order of magnitude faster than the LJ one. In the light of these results, the IPL potential can be considered a good “zero-th order" reference for the LJ potentials in molecular liquids.

While it is known from previous works that the differences in the WCA models are due to the fact that the potential tail is truncated at a cutoff cor-

responding to typical interatomic distances, the origin of the deviations in the IPL model is not clear. To provide insight, virial-potential correlations in LJ models are considered. Strong correlations are seen in chains with rigid bonds and even in semi-rigid chains if the bonding interaction is excluded in the computation of virial and energy. The instantaneous slope $\Gamma(t)$ of the correlation is seen to be a Cauchy variate with Lorentz distribution. Even in the presence of very strong correlations, correlation coefficient $R > 0.9$, the distribution has a long tail which signals the difficulty by the IPL to account for the dynamics resulting by the Lennard-Jones interaction potential.

Chapter 4

Thermodynamic scaling in polymers

4.1 The research context

A fundamental problem in the physics of supercooled liquids and glasses is the understanding of the role played by temperature and density in the viscous slowing down as the glass transition is approached [109–111]. The relative importance of the two parameters cannot be resolved from the usual fixed room pressure experiments where only temperature is changed since thermal and density effect act simultaneously. However, addressing the pressure as a variable, it is possible to work out pure volume effects on transport coefficients of glass forming liquids. The most successful result of this approach is the thermodynamic scaling, or density scaling, that is, the fact that the temperature T and density ρ dependences of the relaxation time τ, viscosity η or diffusion coefficient D can be expressed in terms of the single variable ρ^γ/T, namely:

$$\eta, \tau = \mathcal{F}(\rho^\gamma/T) \tag{4.1}$$

where the scaling exponent γ is a material constant independent of thermodynamic conditions [112–119]. This concept has quickly become very interesting because it constitutes a good basis for establishing useful relations between thermodynamics and relaxation dynamics in the vicinity of the glass transition. Thermodynamic scaling applies to van der Waals liquids, polymers and ionic liquids [27, 120–122] but not to hydrogen-bonded liquids since the equilibrium structure of the liquid is expected to change when temperature and pressure are changed [123]. The scaling exponent γ, which is a measure of the contribution of density relative to that of temperature, varies in the range from 0.13 to 8.5 [27].

Among the possible justifications of the scaling, one hypothesis is that the scaling exponent γ is strictly related to the intermolecular potential. Indeed, for a liquid having a pairwise additive intermolecular potential described by an inverse power law (IPL) $U(r) \propto r^{-m}$, all the reduced thermodynamic and dynamic properties can be expressed in terms of the variable $\rho^{m/3}/T$ [124].

The conformance of real materials to density scaling may result from their intermolecular potential being approximate by an IPL at least for consideration of certain dynamic properties. Systematic MD simulations of Lennard-Jones models with different exponent of the repulsive term $(1/r)^n$ [125] indicated that the density scaling exponent γ is consistent with $\gamma \sim m/3$, being m the steepness of an effective IPL, properly evaluated around the distance of closest approach between particles probed in the supercooled regime ($m > n$ due to contributions of the attractions). More general, Dyre and coworkers proposed that liquids which have strong virial-energy ($W - U$) correlation, the so called strongly correlating liquids, exhibit also density scaling [90]. Moreover the scaling exponent γ is obtainable as the ratio of $W - U$ fluctuations since for a pure IPL potential $W = (m/3)U$. Although such a ratio is state point dependent, a "best fit" value, typically obtained from high temperature state points, has been shown to represent a good estimate of the scaling exponent [126–128]. Note that density scaling extends to non-spherical molecules, and even some hydrogen-bonded liquids (e.g. glycerol and sorbitol) [27], for which a power-law repulsive potential is clearly inadequate.

The function $\mathcal{F}$, which is not the same for different dynamic properties, is not known a priori. An interpretation of the scaling is to consider the $\tau(T, V)$ dependence as thermally activated with a V dependent activation energy $\tau(T, V) = \tau_A \exp(E_A(V)/T)$ where τ_A is a constant [129]. Imposing $E_A(V) \propto V^{-\gamma}$, density scaling is recovered, though such a picture is in contrast with the fact τ is not an exponential function of Tv^γ [27]. Casalini *et al.* [130, 131] used the entropy model of Avramov [132] to derive an expression to fit relaxation times in different conditions of pressure and temperature:

$$\log[\tau(T, v)] = \log(\tau_0) + \left(\frac{B}{Tv^\gamma}\right)^D \tag{4.2}$$

where v is the specific volume. Eq 4.2, with two adjustable parameters in addition to γ, is shown to accurately fit experimental data for several glass-forming liquids and polymers.

4.2 Models

Two different coarse-grained model of linear polymer chain are considered. In the first model, the rigid bonded chain (RB), bonded monomers are connected by a rigid bond of fixed length. In the second model, the semi-rigid bonded chain (SB), bonded monomers interact with a potential which is the sum of the finitely extendible nonlinear elastic (FENE) potential and the Lennard-Jones potential, resulting in a fluctuation of a few percent in the bond length. In both the models nonbonded monomers interact via a truncated parametric potential, whose attractive and repulsive steepness can be modulated:

$$v_{p,q}(r) = \begin{cases} \frac{\epsilon}{q-p}\left[p\left(\frac{\sigma^*}{r}\right)^q - q\left(\frac{\sigma^*}{r}\right)^p\right] + v_{cut} & \text{if } r \le r_c \\ 0 & \text{otherwise} \end{cases} \tag{4.3}$$

where the value of the constant v_{cut} is chosen to ensure $v_{p,q}(r_c) = 0$ at $r = r_c = 2.5\,\sigma$.

All the polymer data are in reduced units: length in units of σ, temperature in units of ϵ/k_B and time in units of $\sigma(\mu/\epsilon)^{1/2}$, where σ and ϵ are given by nonbonding potential and μ is the monomer mass. We set $\mu = k_B = 1$.

States with different values of the temperature T, the density ρ, the chain length M, and the steepness p, q of the monomer-monomer interaction potential are studied. Each state is labelled by the multiplet $\{M, \rho, T, p, q\}$.

Full details about the model, the considered states and the simulation technique are given in Appendix A.

4.3 Results and discussion

4.3.1 Thermodynamic scaling of short-time dynamics

We start by investigating the temperature dependence of the ST-MSD $\langle u^2 \rangle$. In Chapter 2 it was shown that if the cage regime is present a minimum at $t = t^*$ in the $\log - \log$ derivative of the MSD is observed which allow to define the ST-MSD via the relation $\langle u^2 \rangle = \langle r^2(t^*) \rangle$. We indicate as $\langle u_m^2 \rangle$ the high T-value of the ST-MSD at the onset of the cage regime; for the present model $\langle u_m^2 \rangle = 0.125$.

In Figure 4.1 the T-dependence of the ST-MSD along different isochores is shown for systems with different repulsion. We observe that in the considered temperature range $\langle u^2 \rangle(T)$ shows a well-defined linear variation, namely

$$\langle u^2(T) \rangle = a_0 + m \cdot T \tag{4.4}$$

For a given chain length and monomer-monomer interaction, the $T \to 0$ linear extrapolation of $\langle u^2 \rangle$ does not depend on the density, i.e., $a_0 \equiv a_0(M; p, q)$. On the contrary the slope of $\langle u^2(T) \rangle$ is a decreasing function of the density ρ, $m \equiv m(M; \rho; p, q)$.

Note that in Figure 4.1 $\langle u^2(T) \rangle$ extrapolates to zero at a finite temperature. In ref. [133], Zhang *et al.* showed that the temperature at which $\langle u^2(T) \rangle$ linearly extrapolates to zero coincides within the uncertainty with the Vogel-Fulcher-Tammann (VFT) temperature T_0 characterizing the T-dependence of the structural relaxation time. We check this fact on the most numerous set at our disposal ($M = 3$, $\rho = 1.033$ and $p, q = 6, 12$) and we found that the ST-MSD vanish at $T_0^{(ST-MSD)} = 0.20(1)$ which is slightly smaller than the VFT temperature $T_0 = 0.28(2)$, obtained by the best-fit of the corresponding structural relaxation time τ_α.

Now the density dependence of the ST-MSD is discussed. From the previous analysis, we know that the ρ-dependence of the ST-MSD is incorporated only in the isochoric slope m. Hence in Figure 4.2 we show the quantity $\langle u^2 \rangle - a_0$ versus the density at constant temperature. In a $\log - \log$ plot, data from a given isotherm collapse into a straight line which is a signature of a power-law dependence on density. The density scaling exponent, that we label as γ_{ts} for clarity reason, is given by the isotherm slope in the $\log - \log$

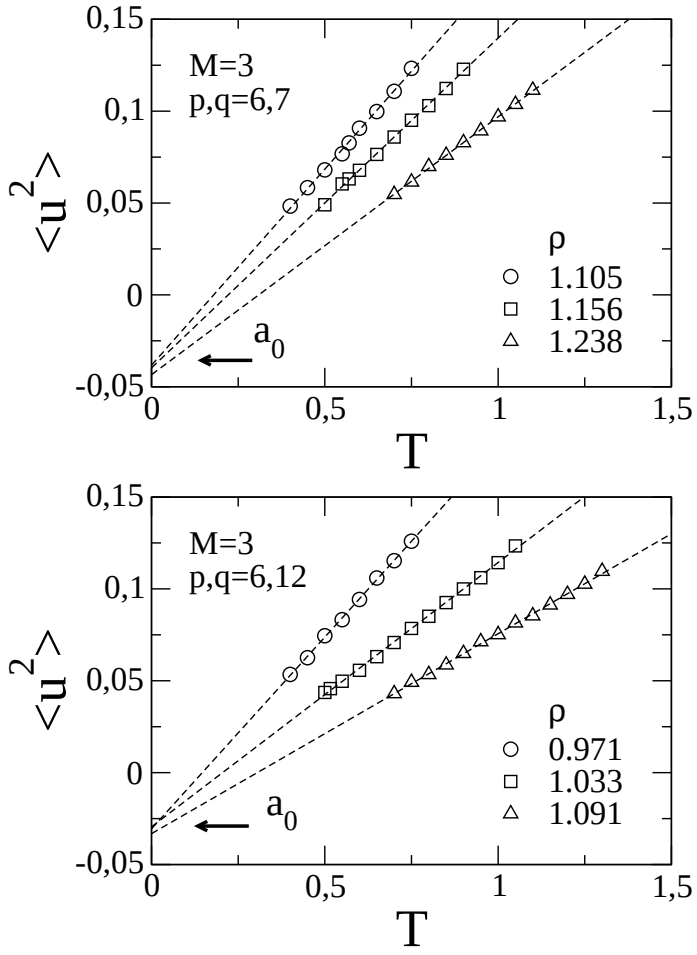

Figure 4.1: Temperature dependence of the ST-MSD $\langle u^2 \rangle$ along different isochores, from MD simulations of semi-rigid bonded chain with length $M = 3$ and steepness of the monomer-monomer potential $p, q = 6, 7$ (top panel) and $p, q = 6, 12$ (bottom panel). Dashed straight lines are best-fit line of the data. The extrapolation for $T \to 0$ gives the parameter a_0.

plot (to be more precise, the slope gives the opposite of the scaling exponent). The density dependence of the isochoric slope m can be work out explicitly $m = a_1 \cdot \rho^{-\gamma_{ts}}$. This results in an equation for the dependence of the ST-MSD on the thermodynamic scaling variable $T\rho^{-\gamma_{ts}}$, namely

$$\langle u^2(T, \rho) \rangle = a_0 + a1 \cdot T\rho^{-\gamma_{ts}} \tag{4.5}$$

where the parameters a_0, a_1 and γ_{ts} depend in general on the chain length, the monomer-monomer potential and the mature of the bonding interaction.

Now we are in the position to investigate the thermodynamic scaling of the ST-MSD in the present models of linear chains. In Figures 4.3 and 4.4, the ST-MSD versus the quantity $T\rho^{-\gamma_{ts}}$ is shown for different systems. It is

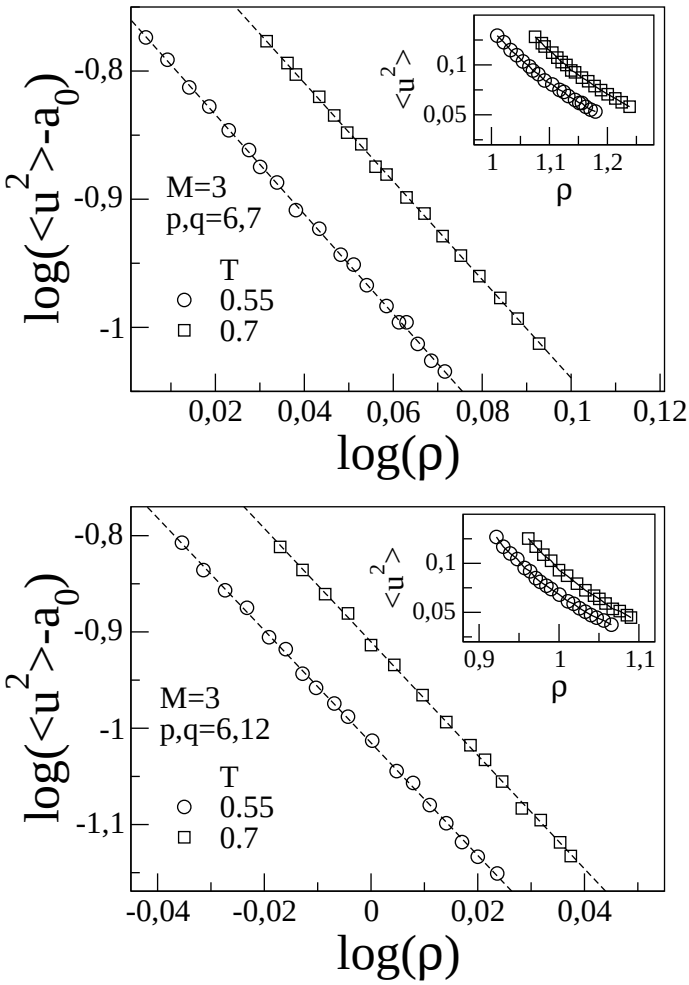

Figure 4.2: Log-log plot of the difference $\langle u_2 \rangle - a_0$, where a_0 is defined in the text, versus the density along different isotherms for the same systems of Figure 4.1. The slope of the best-fit lines (dashed line) gives the exponent of the power-law dependence on density. Insets: the ST-MSD $\langle u_2 \rangle$ versus the density for the same state points of the main panels.

apparent that $\langle u^2 \rangle$ obeys thermodynamic scaling in the form of eq 4.5. All the density scaling exponents γ_{ts} were calculated with a procedure, based on previous observations, that we summarize here:

1. From isochoric measures of $\langle u^2(T) \rangle$, the $T \to 0$ linear extrapolation a_0 of the ST-MSD is calculated. For a given system, we use at least two different isochores.

2. Then the density scaling exponent γ_{ts} is given by the slope of the $\log - \log$ plot of the quantity $\langle u^2(\rho) \rangle - a_0$ versus the density along an isotherm.

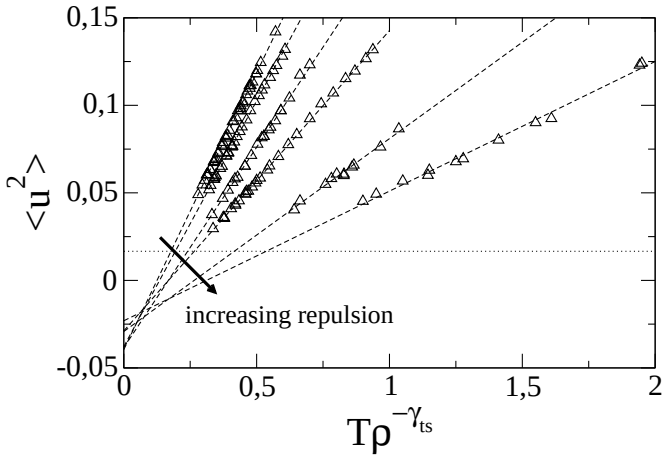

Figure 4.3: The ST-MSD $\langle u^2 \rangle$ versus the thermodynamic scaling variable $T\rho^{-\gamma}$ from MD simulations of semi-rigid chains with $M = 3$ and different repulsion, i.e., different exponent of the repulsive part of the potential $q = 7, 8, 10, 12, 18, 24$. Dashed lines are $\langle u^2 \rangle = a0_+a1 \cdot T\rho^{-\gamma}$. The parameters γ_{ts}, a_0 and a_1 for each system are listed in Table 4.1. Dotted line marks $\langle u_g^2 \rangle \approx 0.0166$, the ST-MSD at the glass transition.

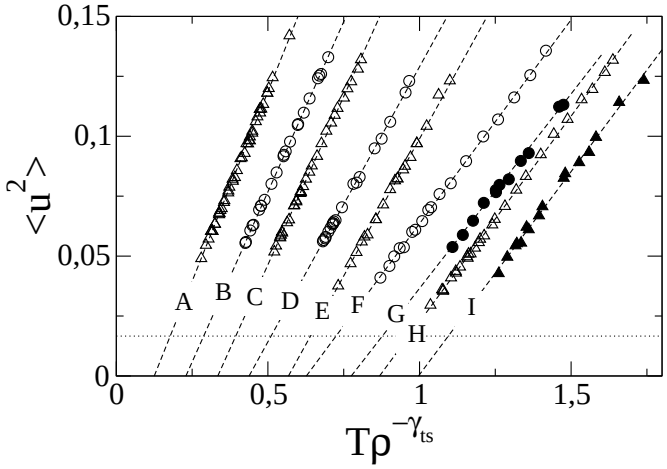

Figure 4.4: Thermodynamic scaling of the ST-MSD: $\langle u^2 \rangle$ versus the quantity $T\rho^{-\gamma}$ from MD simulations of semi-rigid (SB) and rigid bonded (RB) chains with different chain length M and steepness of the monomer-monomer potential p, q. For clarity reasons, data are horizontally shifted. A: SB $M = 3$, $p, q = 6, 7$ (shift:+0.0); B: SB $M = 10$, $p, q = 6, 8$ (+0.1); C: SB $M = 3$, $p, q = 6, 8$ (+0.2); D: SB $M = 10$, $p, q = 6, 10$ (+0.3); E: SB $M = 3$, $p, q = 6, 10$ (+0.4); F: SB $M = 10$, $p, q = 6, 12$ (+0.5); G: RB $M = 10$, $p, q = 6, 12$ (+0.6); H: SB $M = 3$, $p, q = 6, 12$ (+0.7); I: RB $M = 3$, $p, q = 6, 12$ (+0.8). Dashed lines are $\langle u^2 \rangle = a0_+a1 \cdot T\rho^{-\gamma}$. The parameters γ_{ts}, a_0 and a_1 are listed in Table 4.1. Dotted line marks $\langle u_g^2 \rangle \approx 0.0166$, the ST-MSD at the glass transition.

Table 4.1: The density scaling exponent γ_{ts} and the parameter a_0 and a_1 of eq 4.5 for the systems of Figures 4.3 and 4.4

bonds	**M**	$(\mathbf{p},\mathbf{q})$	γ_{ts}	$\mathbf{a_0}$	$\mathbf{a_1}$
semi-rigid	3	$(6,7)$	3.9(1)	$-0.039(2)$	0.317(5)
semi-rigid	10	$(6,8)$	4.7(2)	$-0.036(2)$	0.283(6)
semi-rigid	3	$(6,8)$	4.3(1)	$-0.037(1)$	0.279(4)
semi-rigid	10	$(6,10)$	5.9(2)	$-0.032(1)$	0.0229(5)
semi-rigid	3	$(6,10)$	5.2.(1)	$-0.040(1)$	0.244(6)
semi-rigid	10	$(6,12)$	6.7(1)	$-0.022(1)$	0.170(4)
rigid	10	$(6,12)$	6.65(5)	$-0.029(1)$	0.162(5)
semi-rigid	3	$(6,12)$	5.80(1)	$-0.029(1)$	0.172(4)
rigid	3	$(6,12)$	5.85(5)	$-0.033(2)$	0.169(5)
semi-rigid	3	$(6,18)$	7.6(2)	$-0.029(2)$	0.110(5)
semi-rigid	3	$(6,24)$	8.4(2)	$-0.023(1)$	0.074(5)

Instead, the parameter a_1 in eq 4.5 is given by the intercepts with the vertical axis in the same plot. At least two different isotherms were used at this point.

In Table 4.1 the density scaling exponent γ_{ts} and the parameter a_0 and a_1 are listed.

The fact that the ST-MSD scales as $T\rho^{-\gamma}$, recently observed also in the molten salt CKN [134], is not surprising as long as short-time dynamics and structural relaxation are connected [25]. In this light, thermodynamic scaling of viscosity, relaxation times or diffusion is a consequence of the more fundamental scaling of the fast dynamics.

In Figures 4.3 and 4.4 we show that the actual ST-MSD $\langle u^2 \rangle$ obeys thermodynamic scaling. Recently Fragiadakis [135] pointed out that thermodynamic scales concern reduces quantity as the reduced relaxation time $\tau_\alpha^* = v^{-1/3}(k_BT/m)^{1/2}\tau_\alpha$ or the reduced viscosity $\eta^* = v^{2/3}(mk_BT)^{-1/2}\eta$, where v is the molecular volume, m the molecular mass and k_B is the Boltzmann constant. In this view we should have considered the reduced, ST-MSD $\langle u^2 \rangle^* = \rho^{2/3}\langle u^2 \rangle$. However, in our case, due to the not so large variation of density, the difference between $\langle u^2 \rangle$ and $\langle u^2 \rangle^*$ is negligible. Moreover, in ref. [26], it was shown, in the context of the correlation between fast dynamics and relaxation, that for the present model the scaling of the distances according to $\rho^{-1/3}$ is not only useless but also harmful.

It is interesting to observe that, fixing the chain length and bonding interaction (rigid or semi-rigid) and changing only the repulsion of the monomer-monomer interaction, it seems that all the linear extrapolations of the ST-MSD according to eq 4.5 cross in a single point (see Figure 4.3), suggesting that the two parameters a_0 and a_1 are not completely independent. Note, however, that this intersection, takes place in a non-physical region, i.e., negative ST-MSD.

We want to point out here that the linear dependence on the scaling variable in the form of eq 4.5 is clearly a high-T or low-viscosity behavior. Strong

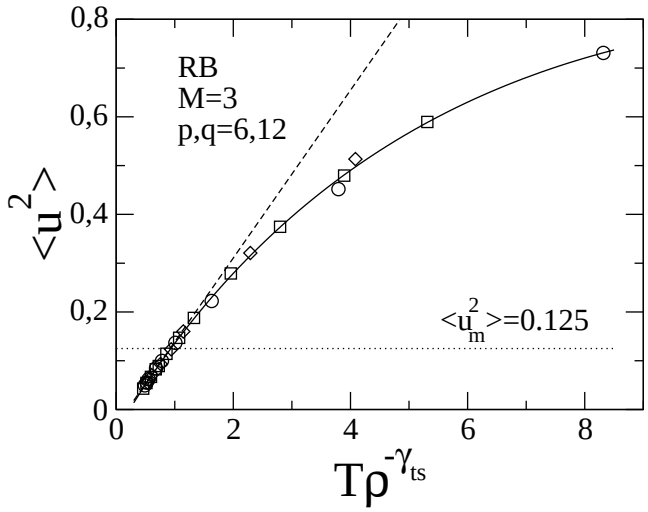

Figure 4.5: ST-MSD defined as $\langle u^2 \rangle = \langle u^2(1.022) \rangle$ as a function of the product $T\rho^{-\gamma^{ts}}$ from Md simulations of rigid-bonded chains with length $M = 3$ and e. Note that density scaling of the dynamics applies from the viscous up to the high-temperature liquid, where the cage effect is not present. Deviation from the low-T linear scaling of eq 4.5 (dashed line) become apparent as the temperature increases. Full line is a guide for the eyes.

deviations may arise as the glass transition is approached. In particular the harmonic behavior $\langle u^2 \rangle \propto T$ is expected below the GT [39]. Nevertheless, the explored T-range is such that the care effect is observed since the definition of the ST-MSD via the relation $\langle u^2 \rangle = \langle u^2(t^*) \rangle$ assumes the appearance of a clear minimum in the $\log - \log$ derivative of the MSD at t^*. We now show that the dynamics obeys the thermodynamic scaling even in the very high temperature region where the cage effect is not present. Remind that for the present model we have that $t^* = 1.022$ does not depend on the state point. In Figure 4.5 we plot the ST-MSD, defined as $\langle u^2 \rangle = \langle u^2(t^* = 1.022) \rangle$ irrespective of whether $t = t^*$ marks the onset of the cage regime, as a function of the scaling variable $T\rho^{-\gamma_{ts}}$. We observe that the scaling exponent γ_{ts} of the "cage" ST-MSD is able to give a very good collapse of the data even for extremely large value of the product $T\rho^{-\gamma_{ts}}$. Deviation from the linear scaling of eq 4.5 become apparent as the temperature increases. The fact that density scaling of the dynamics applies from the viscous up to the high-T liquid, where the structure relaxes on time scale which are faster than picosecond, is in our opinion not trivial.

Note that for the present model we have $\gamma_{ts} > 4$ (see Table 4.1). Usually, high molecular weight polymers are characterized by small values of the exponent, $\gamma_{ts} < 2.6$ [27]. These small values are mainly due to the relative stiffness of the chain units, with respect to the mobility corresponding to the intermolecular degrees of freedom: the stiff chain structure hinders rearrangements, resulting in smaller sensitivity to volume effects [136]. An exception is represented by the polysiloxanes, which have a very flexible chain, and are

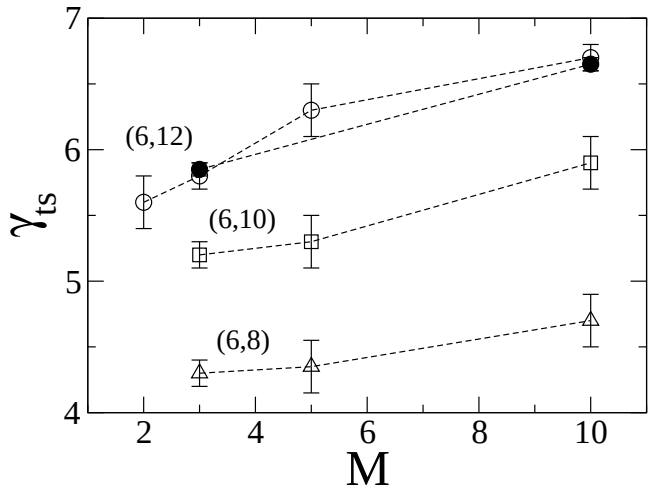

Figure 4.6: Density scaling exponent γ_{ts} versus the chain length M for system with different monomer-monomer interaction potential, as indicated by the steepness of the attractive and repulsive parts (p, q) (number in parenthesis) for chains with semi-rigid bonds (open symbols) and rigid bonds (full symbols).

characterized by larger values of the scaling exponent $\gamma_{ts} \gtrsim 5$ [137]. In the present model of linear chain, no potential for the bond angle are introduced and the back folding of adjacent bonds is only suppressed by the monomer-monomer repulsion. The large values of the scaling exponent that we found are then the results of the high flexibility of the chains. Moreover the value of $\gamma_{ts} = 6.7(1)$ in the case of decamers ($M = 10$) with semi-rigid bond and interacting via the Lennard-Jones potential ($p, q = 6.12$) is very close to that $\gamma_{ts} = 6$ that Budzien *et al.* used to scale diffusion coefficients in the same model [138].

In order to continue the discussion on the density scaling exponent γ_{ts}, in Figure 4.6 we plot γ_{ts} versus the chain length M for systems with different bonds and monomer-monomer interaction. It is apparent that for the present model γ_{ts} increases as the length of the chain increases. The increase is steeper for short chain and it become smoother as the chain become longer (see the case of $p, q = 6.12$). This behavior is again similar to the one of siloxane polymers, in which the scaling exponent, and also other dynamic properties such as the fragility and the glass transition temperature, seem not to depend on the chain length [137]. On the contrary in stiffer polymers, like the polymethylmethacrylate, the exponent decreases abruptly as the length of the chain increases [136].

Finally we want to discuss how the scaling exponent is related to the monomer-monomer interaction potential as described, according to recent works on thermodynamic scaling, via the fluctuations of virial and potential energy [128, 134]. This relies on the inverse-power-law picture, a topic that was discussed in Chapter 3. In Figure 4.7 the instantaneous fluctuations of virial are plotted versus those in the potential energy for systems with different ex-

ponent of the repulsive part of the monomer-monomer interaction potential. According to what we have shown in Chapter 3, we neglect the bonding interaction in the calculation of both the virial and the potential energy in order to achieve strong $U - W$ correlations (correlation coefficient $R \geq 0.9$). We define the quantity γ_{ipl} as the as the ratio of fluctuations. Since it is known that such a ratio is state-point dependent, we define a "mean" value by considering the global fluctuation. i.e. the fluctuations in all the state point, with different temperature and density, that we consider in the thermodynamic scaling. Note that, in agreement with the idea on an underlying inverse-power-law picture analogy, γ_{ipl} increases as the exponent of repulsion increases.

Now we are in the position to compare the thermodynamic scaling exponent γ_{ts} with the prediction γ_{ipl} of the IPL picture. In Figure 4.8 we show the correlation plot of γ_{ts} and γ_{ipl} for systems with different repulsion and chain length. We observe clear deviations from the expected $\gamma_{ts} = \gamma_{ipl}$ with $\gamma_{ts} > \gamma_{ipl}$ for all the systems except the one with the steeper repulsion, where $\gamma_{ts} \lesssim \gamma_{ipl}$. This larger values than the IPL ones reflect the influence of the bonding interaction. Note, indeed, the deviations are small, almost negligible, for short chains (see $M = 3$) but become significant if the length of the chains increases (see $M = 10$). For the semi-rigid chains, the bonding potential, resulting from the combination of the Lennard-Jones and the FENE potential (see Appendix A for details), in the vicinity of the minimum is extremely sharp, in particular steeper than the monomer-monomer potential. The intramolecular bonds thus serve to increase the steepness of the effective repulsive potential on monomers, resulting in a more sensitivity to volume effects and in a larger γ_{ts}. If one increase the monomer-monomer repulsion, the effect of the bonding interaction become increasingly less important; this explain the different behavior of the $q = 24$ potential (see Figure 4.8) for which $\gamma_{ts} \sim \gamma_{ipl}$.

4.3.2 An asymmetry model for the fast dynamics

Now we introduce a minimal model, that is the asymmetric double-well potential [139, 140], which is able, once some assumptions are made, to reproduce the linear dependence of the ST-MSD on the thermodynamic variable observed in our MD simulations.

We start by assuming that, in equilibrium condition, the system explore a potential energy landscape (PEL) consisting of two level, a ground (labeled g) and an excited level (labeled e) (see Figure 4.9) The energy difference between the two level is given by Δ. The ground state can, for example, corresponds to an efficient packing of molecules while the excited state corresponds to a less efficient packing, resulting in a higher energy due to the increased average distance between molecules. In this model structural relaxation is associated to the transitions $e \leftrightarrow g$. In equilibrium the probability currents are equal, namely $J_{g\to e} = J_{e\to g}$.

The short-time mean squared displacement is computed as the mean squared displacement on a time scale much faster than the structural relaxation:

$$\langle u^2 \rangle = \langle r^2(t - t_0) \rangle \qquad t - t_0 \ll \tau_\alpha \tag{4.6}$$

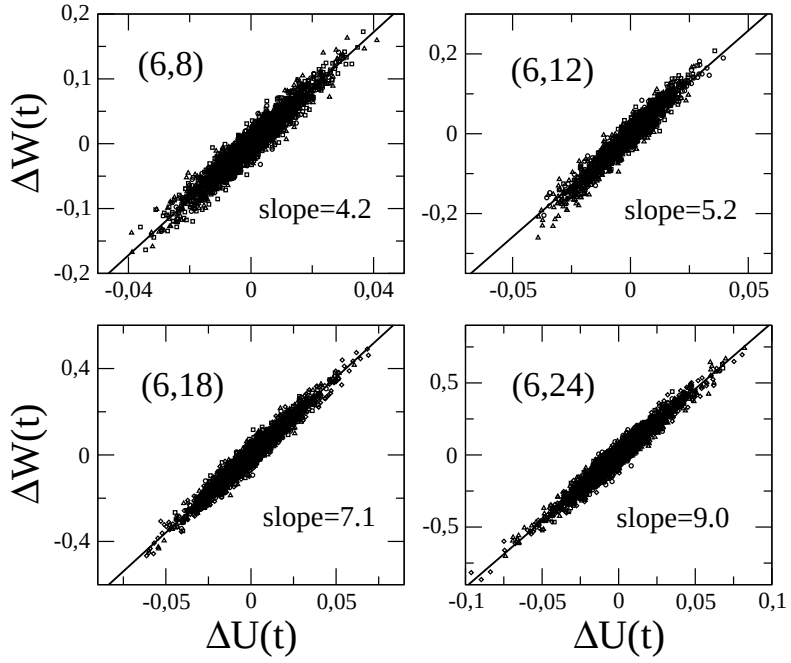

Figure 4.7: Global instantaneous fluctuations of virial versus those of the potential energy in semi-rigid bonded chain with length $M = 3$ and different monomer-monomer repulsive interaction for the parametric (p, q) potential (as indicated by the number in parenthesis). The solid lines represent the linear best fits, whose slope define the quantity γ_{ipl}.

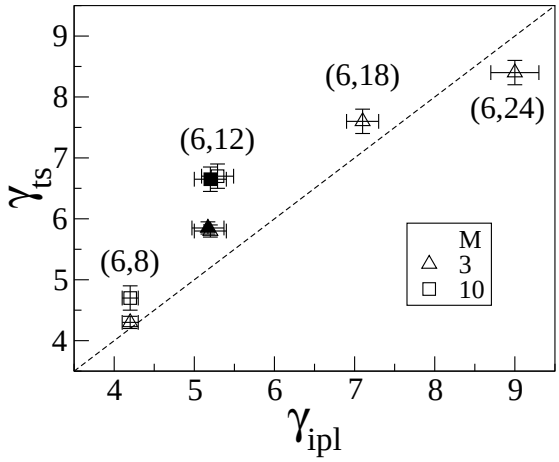

Figure 4.8: Correlation plot of the thermodynamic scaling exponent γ_{ts} versus the slope of virial-potential fluctuations γ_{ipl} for system with different chain length and monomer-monomer interaction potential, as indicated by the steepness of the attractive and repulsive parts (p, q) (number in parenthesis). Both chains with semi-rigid bonds (open symbols) and rigid bonds (full symbols) are considered.

On short time scale, molecules oscillate around the equilibrium positions, corresponding to the bottom of a potential well. Then eq 4.6 can be expressed as [141]:

$$\langle u^2 \rangle = \frac{1}{1+ze^{-\beta\Delta}} \frac{1}{\beta k_g} + \frac{ze^{-\beta\Delta}}{1+ze^{-\beta\Delta}} \frac{1}{\beta k_e} \tag{4.7}$$

where $\beta = 1/k_B T$, z is the number of state in the excited level and k_g and k_e, $k_g > k_e$, are the effective elastic constant of the g and e level respectively. The number of state z is related to the fragility: the larger z, the more fragile the system [3].
In the high temperature limit $\beta\Delta \ll 1$, eq 4.7 reduces to:

$$\begin{aligned}
\langle u^2 \rangle &\simeq \frac{1}{1+z-z\beta\Delta} \left[\frac{1}{\beta k_g} + z\left(1-\beta\Delta\right) \frac{1}{\beta k_e} \right] && (4.8)\\
&= \frac{1}{(1+z)(1-(z\beta\Delta)/(1+z))} \left[\beta^{-1} \left(\frac{1}{k_g} + \frac{z}{k_e} \right) - \frac{z\Delta}{k_e} \right] && (4.9)\\
&\simeq \frac{1}{1+z} \left(1 + \frac{z}{z+1}\beta\Delta \right) \left[\beta^{-1} \left(\frac{1}{k_g} + \frac{z}{k_e} \right) - \frac{z\Delta}{k_e} \right] && (4.10)\\
&= \frac{1}{1+z} \left[\beta^{-1} \left(\frac{1}{k_g} + \frac{z}{k_e} \right) - \frac{z\Delta}{z+1} \left(\frac{1}{k_e} - \frac{1}{k_g} \right) \right] && (4.11)
\end{aligned}$$

The effective elastic constant k_g and k_e are a function only of density since the PEL does not depend on temperature [142]. Then we write $k_i = \chi_i f(\rho)$, and we assume that the function $f(\rho)$ does not depend strongly on the energy level.

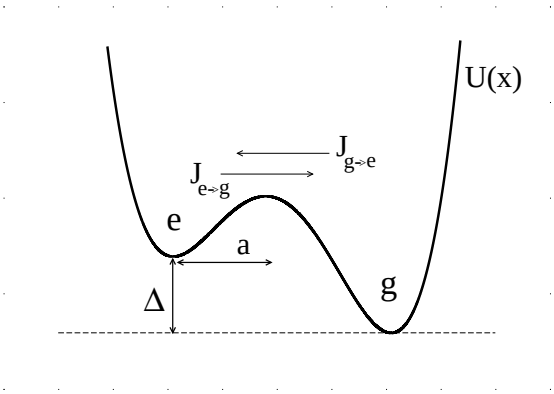

Figure 4.9: Asymmetric double-well potential as a function of the generalized coordinate. Δ is the energy difference between the ground (g) and the excited level (e). $J_{g\to e}$ and $J_{e\to g}$ are the probability current for the transition between the two level. The displacement to reach the transition state is a.

In the harmonic approximation of the potential we have

$$k_e\overline{a^2} + \Delta \simeq k_g\overline{a^2} \tag{4.12}$$

where $\overline{a^2}$ is the mean square displacement to reach the transition state. The second term in eq 4.11 is constant since

$$\frac{\Delta}{k_i} \simeq \frac{\left(k_g - k_e\right)\overline{a^2}}{k_i} \qquad i = g, e \tag{4.13}$$

$$\simeq \frac{\left(\chi_g - \chi_e\right)\overline{a^2}}{\chi_i} \tag{4.14}$$

Then eq 4.11 can be written in the form:

$$\langle u^2\rangle = \frac{1}{1+z}\left(\frac{1}{\chi_g} + \frac{z}{\chi_e}\right) k_B\left[T(f(\rho))^{-1} - T_0(f(\rho_0))^{-1}\right] \tag{4.15}$$

where we have defined the quantity

$$T_0(f(\rho_0))^{-1} = \frac{z}{z+1}\frac{\overline{a^2}(\chi_g - \chi_e)^2}{\chi_e + z\chi_g} \tag{4.16}$$

According to eq 4.15, the isochoric $\langle u^2\rangle$ is a linear function of temperature. Moreover eq 4.15 predicts that the ST-MSD vanishes at a finite temperature T_0. These findings agree with our results from MD simulations. For a strong system, $z \sim 0$, the temperature T_0 vanishes and we recover the relation $\langle u^2(T)\rangle \propto T$, seen in experiments on strong glass-formers [39].

At this point, the connection with the thermodynamic scaling is made, by assuming that the elastic constants scale as ρ^n. A similar dependence is observed in porous gels, systems that are not completely mechanically connected, where the Young's modulus E scales as $E \sim \rho^m$ with $m \sim 4$ [143].

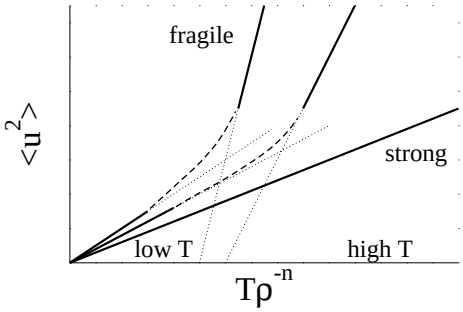

Figure 4.10: ST-MSD versus the product $T\rho^{-n}$, according to asymmetric potential model. At low temperature, $\langle u^2 \rangle \propto T\rho^{-n}$. For strong systems, this behavior extends up to high temperature. For fragile system, the model predicts $\langle u^2 \rangle \propto (T\rho^{-n} - T_0\rho_0^{-n})$ at high temperature.

Glass forming liquids are of course different systems, however it is known the presence in the liquid structure of void region, especially at low density [144, 145], a fact that can justify a bold comparison with gels.
Then, if we write $f(\rho) = \rho^n$, eq 4.15 become

$$\langle u^2 \rangle = \frac{1}{1+z}\left(\frac{1}{\chi_g} + \frac{z}{\chi_e}\right) k_B \left[T\rho^{-n} - T_0\rho_0^{-n}\right] \tag{4.17}$$

A linear dependence of the ST-MSD on the product $T\rho^{-n}$ is found for the present model of asymmetric potential at high temperature (see Figure 4.10). This agrees with eq 4.5 describing the dependence of the ST-MSD on the thermodynamic variable in MD simulations. Furthermore, we found that the slope of eq 4.5 increases as the fragility increases, i.e., the monomer-monomer repulsion decreases (see Figure 4.3 and Table 4.1). Note that the slope of eq 4.17 $(1/\chi_g + z/\chi_e)k_B/(z+1)$ is an increasing function of z and then of fragility.

In the limit of low temperature $\beta\Delta \gg 1$, the higher energy level is not populated and eq 4.7 reduces to:

$$\langle u^2 \rangle \simeq \frac{1}{\beta k_g} \tag{4.18}$$

$$\simeq \frac{1}{\chi_g} k_B T\rho^{-n} \tag{4.19}$$

where we assumed again that $k_g \propto \rho^n$. At low temperature, then, the model predicts that $\langle u^2 \rangle \propto T\rho^{-n}$ (see Figure 4.10), as one would expect.

4.3.3 Thermodynamic scaling of relaxation

Here the thermodynamic scaling of the relaxation dynamics is discussed. In Figure 4.11 the structural relaxation time τ_α as a function of the variable $T\rho^{-\gamma_{ts}}$ is shown for different values of the scaling exponent. Note that the scaling exponent γ_{ts} resulting in the best collapse of the data coincide within the

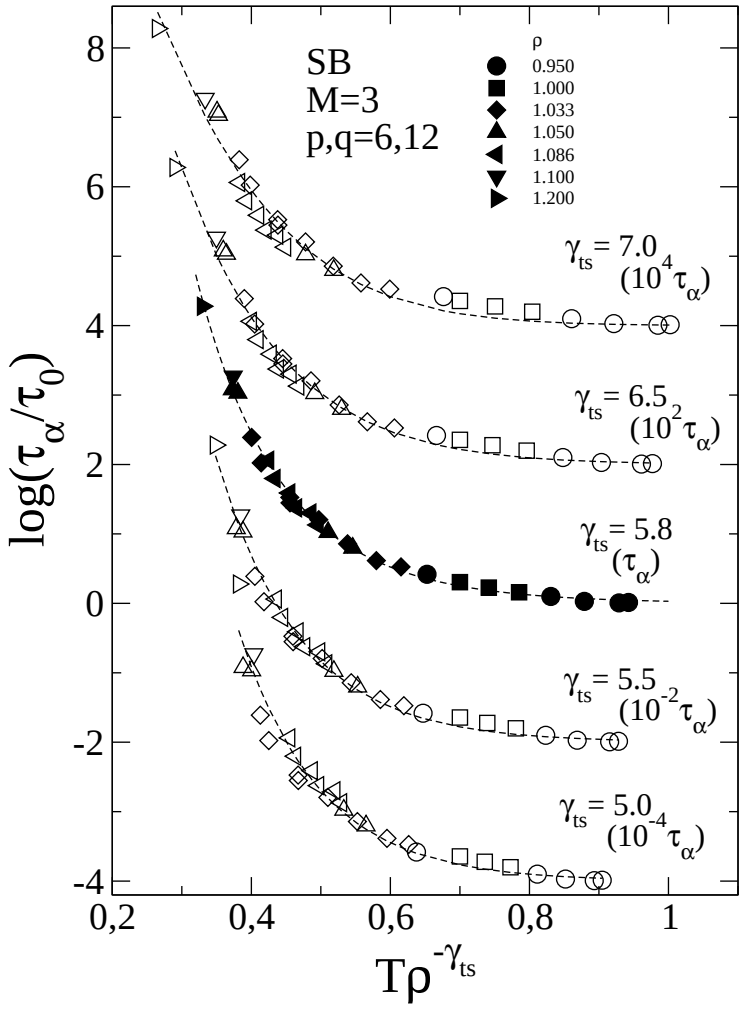

Figure 4.11: Structural relaxation time τ_α versus the product $T\rho^{-\gamma_{ts}}$ with five different values of the scaling exponent. Isochoric states (same density with a tolerance of 5% are plotted with the same symbols. The best collapse of the data is achieved for $\gamma_{ts} = 5.8$ which coincides, within the uncertainty, with the scaling exponent of the ST-MSD. Dashed lines are guides for the eyes.

uncertainty with the density scaling exponent of the ST-MSD. This agrees with the findings of previous work where the coincidence of the scaling exponent for different dynamical quantity was shown [27].

Now we show that for the present model it is possible to work out an explicit expression for the dependence of the structural relaxation time on the variable $T\rho^{-\gamma_{ts}}$ on the basis of the connection between fast dynamics and relaxation. Indeed, the combination of the linear equation for the density scaling of the ST-MSD, eq 4.5 and the parabolic relation connecting the ST-MSD and structural relaxation eq 2.6 gives

$$\log \tau_\alpha = \alpha + \frac{\beta}{(a_0 + a1 \cdot T\rho^{-\gamma_{ts}})} + \frac{\gamma}{(a_0 + a1 \cdot T\rho^{-\gamma_{ts}})^2} \tag{4.20}$$

where α, β and γ are universal while a_0 and a_1, as well as γ_{ts}, are system dependent as they depend on the chain length (M), nature of the bond (b with $b = RB$ for rigid bond and $b = SB$ for semi-rigid bond) and monomer-monomer interaction (label with the steepness of attractive and repulsive part p, q). Eq 4.20 can be recast in a more compact form:

$$\log \tau_\alpha = \log \tau_0 + \frac{r(T\rho^{-\gamma_{ts}}) + s}{(1 + t(T\rho^{-\gamma_{ts}}))^2} \tag{4.21}$$

with

$$\begin{aligned} \log \tau_0 &= \alpha \\ r(M; b; p, q) &= \beta a_1 / a_0^2 \\ s(M; b; p, q) &= (\beta a_0 + \gamma)/a_0^2 \\ t(M; b; p, q) &= a_1 / a_0 \end{aligned}$$

In Figure 4.12 we compare eq 4.20 with the structural relaxation data from MD simulations for the more extended sets at our disposal. No adjustable parameters were used since the density scaling exponent γ_{ts} and the parameter a_0 and a_1 were extracted from the thermodynamic scaling of the ST-MSD. We observe that eq 4.20 fits very well the simulations data over about four decades of relaxation time.

To complete the analysis of the thermodynamic scaling we consider the reorientation relaxation time, i.e., the relaxation time of the correlation function of the vector joining the first and the last monomer of a chain. In Figure 4.13 we show that the exponent γ_{ts} from the scaling of the structural relaxation time, is able to scale also the chain reorientation time.

4.3.4 Comparison with experiments from literature

Now we want to investigate if the expression of the master curve for the thermodynamic scaling in MD simulations, 4.20, is able to reproduce the dependence of the relaxation time on the product $T\rho^{-\gamma_{ts}}$ in real experiments. We are aware that this is a bold comparison. Indeed while eq 2.6, connecting fast dynamics and relaxation, is known to holds true down to the glass transition (GT), the linear master curve for the thermodynamic scaling of the fast dynamics, eq 4.5, is supposed to fail as the system approach the GT.

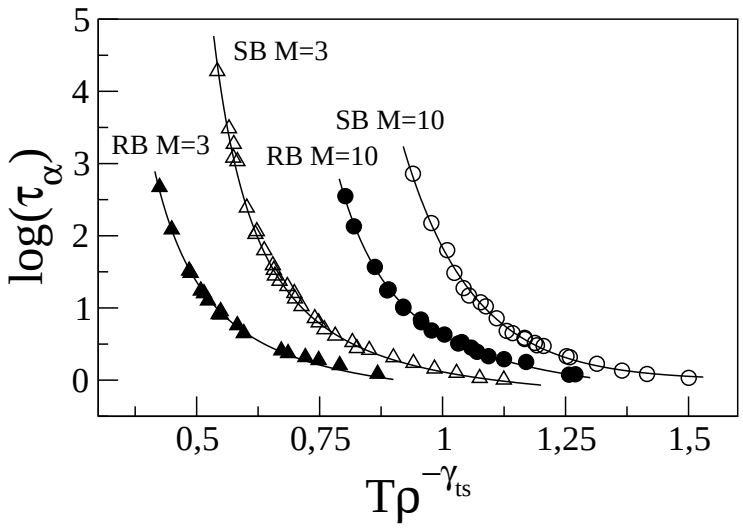

Figure 4.12: Thermodynamic scaling of the structural relaxation time τ_α from MD simulations of rigid bonded (RB) and semi-rigid bonded (SB) Lennard-Jones ($p, q = 6, 12$) chains with length $M = 3, 10$. For clarity reasons data are horizontally shifted: RB $M = 3$ $shift = +0.0$, SB $M = 3$ $+0.2$, RB $M = 10$ $+0.4$ and SB $M = 10$ $+0.6$. The density scaling exponent γ_{ts} is taken from the thermodynamic scaling of the ST-MSD (see Figure 4.4). Full line is eq 4.20, whose parameters are obtained from the scaling of the ST-MSD. The density scaling exponent γ_{ts} and the parameters of eq 4.20 for each system are listed in Table 4.1.

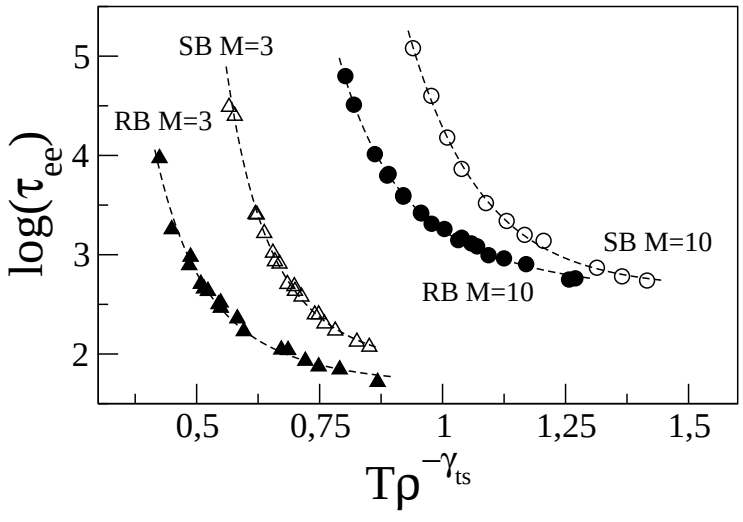

Figure 4.13: Thermodynamic scaling of the reorientation relaxation time τ_{ee}, i.e., the relaxation time of the end-to-end correlation function, for the same systems of Figure 4.12. For clarity, data are horizontally shifted (shift are the same of Figure 4.12). Dashed lines are guides for the eyes.

To extend eq 4.20 to experimental data, the starting point is the assumption that the ST-MSD shows a linear dependence on $T\rho^{-\gamma_{ts}}$, namely

$$\langle u^2 \rangle = \langle u_g^2 \rangle \left[1 + \kappa \left(T\rho^{-\gamma_{ts}} - T_g \rho_g^{-\gamma_{ts}} \right) \right] \tag{4.22}$$

where $\langle u_g^2 \rangle$ is the ST-MSD at the GT, which is supposed to occur at $T_g \rho_g^{-\gamma_{ts}}$. The connection between the fast dynamics and relaxation is given by

$$\log \tau = \alpha + \tilde{\beta} \left(\frac{\langle u_g^2 \rangle}{\langle u^2 \rangle} \right) + \tilde{\gamma} \left(\frac{\langle u_g^2 \rangle}{\langle u^2 \rangle} \right)^2 \tag{4.23}$$

with $\tilde{\beta} = \beta / \langle u_{g,p}^2 \rangle$ and $\tilde{\gamma} = \gamma / \langle u_{g,p}^2 \rangle^2$, α, β and γ are defined in eq 2.6 and $\langle u_{g,p}^2 \rangle$ is the ST-MSD at the GT for the present model of fully flexible chain. Combining eq 4.22 and 4.23, we obtain

$$\log \tau = \alpha + \frac{\tilde{\beta}}{\left[1 + \kappa \left(Y - Y_g \right) \right]} + \frac{\tilde{\gamma}}{\left[1 + \kappa \left(Y - Y_g \right) \right]^2} \tag{4.24}$$

where we have defined $Y \equiv T\rho^{-\gamma_{ts}}$. Once the scaling exponent γ_{ts} and the location of the GT $T_g \rho_g^{-\gamma_{ts}}$ are known, eq 4.24 has only one adjustable parameter, the "slope" κ. This has to be compared with eq 4.2, derived from the Avramov model which has at least two adjustable parameters.

In Figures 4.14 and 4.15 we shows the comparison of eq 4.24 with experimental data of systems spanning a large range of dynamical behavior as indicated by the scaling exponent $1.8 \lesssim \gamma \lesssim 6.5$. As eq 4.24 was derived from MD simulations of a polymer model, we focus mainly on polymeric systems. In order to ensure the best-fit of the data, we allow small adjustments of $\langle u_{g,p}^2 \rangle$ within its uncertainty. The data sources as long as the curve parameters are listed in Table 4.2.

Note that, despite having only one adjustable parameter, eq 4.24 provide a good description of the dependence of $\log \tau$ on $T\rho^{-\gamma}$ in a wide range of relaxation time. It is impressive the case of propylene carbonate (PC) in Figure 4.14, in which the agreement between experimental data and the proposed master curve extends for about fourteen decades of relaxation times. In some systems, systematic deviations are seen, which become apparent if we consider the residuals of the best fit, i.e., the difference between the actual and the expected $\log \tau$. In Figure 4.16, structured residuals are seen clearly for cresolphthalein-dimethyl-ether (KDE) and phenolphthalein-dimethyl-ether (PDE), two molecular liquids. The deviations of the fitted curves are less than ± 0.6 while the global standard deviation of the best fits is $\sigma_G \simeq 0.12$. These values are also affected by the scattering of the experimental data which is apparent in some systems.

We want to point out here that the master curve eq 4.24 is obtained by assuming also that a relation between fast dynamics and slow relaxation exists in the form of eq 4.23. While this relation was seen to fit with experimental data on several different system, at present time for most of the systems in Figures 4.14 and 4.15 such a comparison lacks due to the absence of fast dynamics data.

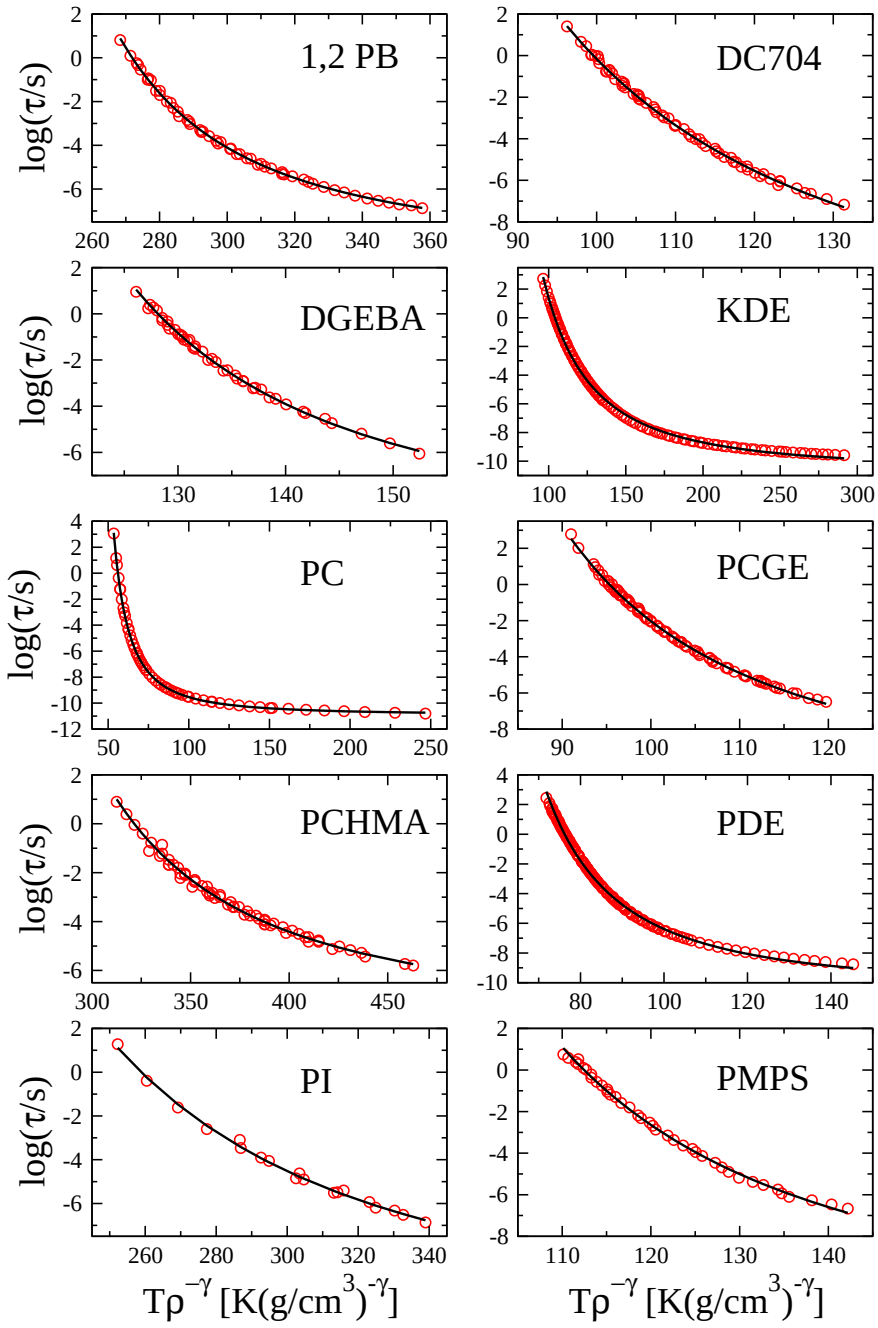

Figure 4.14: $\log \tau$ versus $T\rho^{-\gamma}$ for different materials along with the best fit of eq 4.24: 1,2-polybutadiene (1,2 PB), tetramethyl-tetraphenyl-trisiloxane (DC704), diglycidyl ether of bisphenol-A (DGEBA), cresolphthalein-dimethyl-ether (KDE), propylene carbonate (PC), poly((o-cresyl glycidyl ether)-co-formaldehyde) (PCGE), polycyclohexylmethacrylate (PCHMA), phenolphthalein-dimethyl-ether (PDE), 1,4 polyisoprene (PI) and polymethylphenylsilane (PMPS). The fit parameters and the data sources are given in Table 4.2.

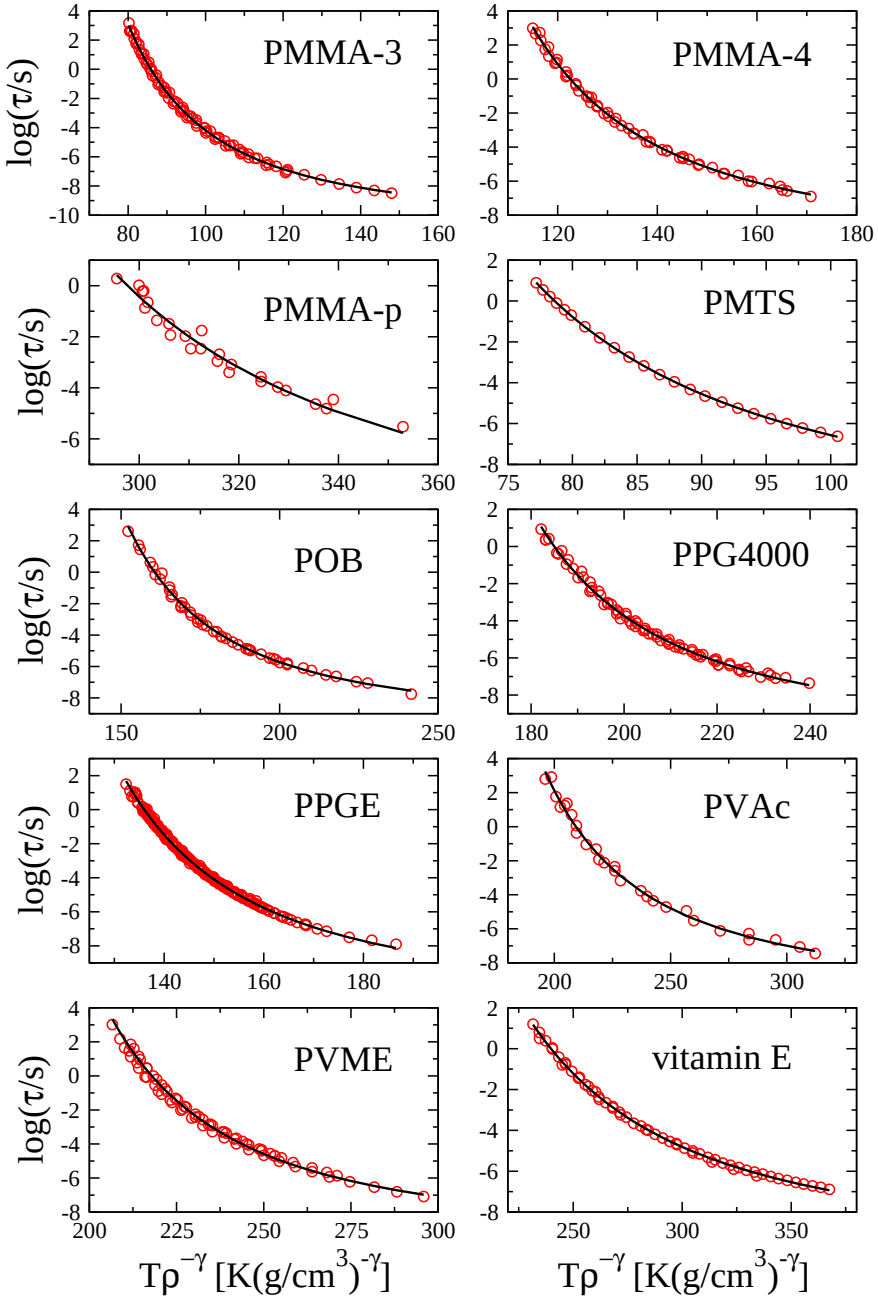

Figure 4.15: $\log \tau$ versus $T\rho^{-\gamma}$ for different materials along with the best fit of eq 4.24: polymethylmethacrylate with degree of polymerization $n = 3, 4$ (PMMA-3, PMMA-4), polymethylmethacrylate (PMMA-p), polymethyltolylsiloxane (PMTS), polybutyloxide (POB), polypropilene glycol with $n = 4000$ (PPG4000), polyphenylglycidyl ether (PPGE), polyvinyl acetate (PVAc), polyvinylmethylether (PVME) and α-tocopherol acetate (vitamin E). The fit parameters and the data sources are given in Table 4.2.

Table 4.2: Relevant information about the investigated systems in Figures 4.14 and 4.15: the density scaling exponent γ, along with the source of the data, the best fit parameter κ in eq 4.24 and the best value of $\langle u_{g,p}^2 \rangle$.

System	γ	**Ref.**	$\kappa \cdot 10^2$ $[\mathrm{K}^{-1}(g/cm^3)^\gamma]$	$\langle u_{g,p}^2 \rangle$ (MD units)
1,2 PB	1.89	[119]	1.23(5)	0.135
DC704	6.15	[146]	1.5(1)	0.124
DGEBA	2.8	[147]	2.8(1)	0.134
KDE	4.5	[119]	1.7(1)	0.132
PC	3.8	[114]	5.2(3)	0.131
PCGE	3.3	[148]	2.4(1)	0.129
PCHMA	2.9	[149]	0.76(8)	0.140
PDE	4.4	[119]	3.0(1)	0.132
PI	3.5	[150]	0.07(1)	0.129
PMPS	5.63	[151]	1.9(1)	0.127
PMMA-3	3.7	[136]	2.3(1)	0.132
PMMA-4	3.2	[136]	1.9(1)	0.134
PMMA-pol	1.8	[136]	1.0(1)	0.134
PMTS	5.0	[152]	3.0(1)	0.134
POB	2.65	[153]	1.7(1)	0.135
PPG4000	2.5	[154]	1.9(1)	0.133
PPGE	3.45	[147]	2.1(1)	0.130
PVAc	2.6	[155]	1.2(1)	0.134
PVME	2.55	[156]	1.4(1)	0.135
vitamin E	3.9	[157]	0.77(5)	0.134

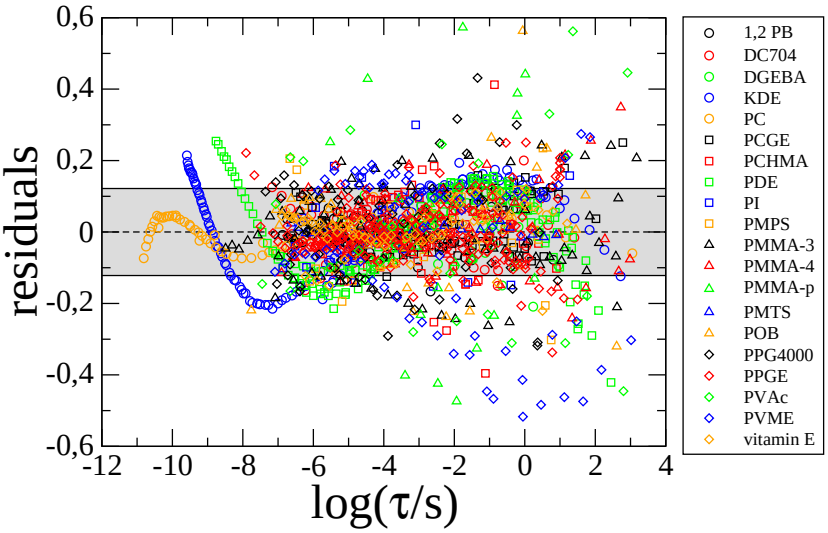

Figure 4.16: Residual of the best fit with eq 4.24 for the systems in Figures 4.14 and 4.15. Full lines mark the global standard deviation of best fit $\sigma_G \simeq 0.12$.

From the master curve of thermodynamic scaling, the fragility, i.e., the popular quantity used to classify the deviation from the Arrhenius behavior in glass formers, can be computed. In particular the expression for the isochoric fragility m_v can be written as

$$m_v = \left. \frac{\partial \log \tau}{\partial \left(Y_g / Y \right)} \right|_{Y_g} \tag{4.25}$$

where again $Y = T\rho^{-\gamma_{ts}}$. Assuming eq 4.24, one obtain

$$\tilde{m}_v = \kappa \left(\tilde{\beta} + 2\tilde{\gamma} \right) T_g \rho_g^{-\gamma} \tag{4.26}$$

The fact that, according to eq 4.26, $\tilde{m}_v$ is a constant agrees with experimental results [119]. In Figure 4.17 the comparison between the experimental m_v and the estimated $\tilde{m}_v$ is shown for the same systems of Figures 4.14 and 4.15. We observe that for the most of the systems, the estimated isochoric fragility deviates significantly from the experimental one. However, this is not surprising. Indeed both eq 4.24 and eq 4.26 were obtained assuming the it is possible to describe the dependence of the ST-MSD on $T\rho^{-\gamma}$ with a single linear relation in the entire temperature range. This “mean" description is supposed to fail in capturing fine details close to GT like the fragility. Note that the deviations are larger for the most fragile systems (PMMA and PCGE) for which the T-dependence of the $\langle u^2 \rangle$ shows large difference between high and low temperature.

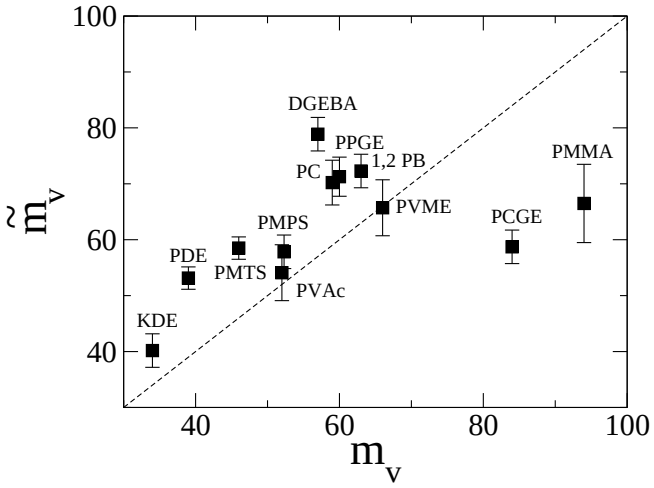

Figure 4.17: Plot of the isochoric fragility $\tilde{m_v}$, estimated according to eq 4.26, versus the experimental m_v for the systems of Figures 4.14 and 4.15. Dashed line is $\tilde{m_v} = m_v$. Deviations from the estimated and the experimental fragility are apparent.

4.4 Conclusions and open questions

Via extensive MD simulations the thermodynamic scaling in a melt of fully flexible unentangled polymer chains have been investigated. Different chain lengths and monomer-monomer interaction potentials are considered. In the first part the scaling of fast dynamics is considered. In the cage regime, the ST-MSD is seen to obeys thermodynamic scaling. The resulting master curves are well described by simple linear equation. In this framework, a rigorous procedure to compute the density scaling exponent is shown, based on isochoric and isothermal measures of the ST-MSD. We observed that the thermodynamic scaling applies up to highly liquid state points where the monomers caging is not present.

The relation between the scaling and the monomer-monomer interaction potential is discussed. According to the picture of the analogy with the inverse-power-law potential, we have compared the exponent γ_{ts} with the slope of the virial-potential correlation γ_{ipl}. γ_{ts} is seen to exceed the value of γ_{ipl} due to the hardening of the effective potential between monomers by the steep bonding interaction.

A minimal model, the double asymmetric well, is introduced. This model, once some assumptions are made, is able to reproduce in the high temperature limit the observed linear dependence of the ST-MSD on the thermodynamic variable. The model agrees with experimental results also in the low temperature limit.

Thermodynamic scaling applies also to relaxation: the exponent for fast dynamics is able to scale both structural relaxation and chain reorientation times. Combining the relation between fast dynamics and slow relaxation with the linear scaling of the ST-MSD (system dependent), an explicit expression

for the master curve of structural relaxation in MD simulations is obtained. It is shown that the proposed master curve fits the experimental results in several systems with only one adjustable parameter, to be compared with entropy based model which has at least two adjustable parameters. The isochoric fragility, estimated via the master curve of the thermodynamic scaling, is seen to significantly deviate from the experimental one, suggesting that the linear picture of the thermodynamic scaling of the ST-MSD is in some case too simple.

Chapter 5

Elastic models of glass transition: a MD simulation study

5.1 The research context: elastic models

The quest for a general theory of the supercooled liquids and the glass transition is still an open question. Different theoretical frameworks provide different interpretation of the complex phenomenology. Thermodynamic theories relate the behavior of glass-forming systems to the existence of a thermodynamic underlying singularity that can be described in purely static terms. This idea is the basis of several approaches including the classic free-volume [158, 159] and configurational-entropy models [160, 161], the random first-order transition theory (RFOT) [162, 163] and frustration-based theories [164]. On the other hand, in non thermodynamic approaches, structural arrest is viewed as a dynamic singularity in the relaxation of supercooled liquids, with no thermodynamic signature. This is the case of the mode-coupling theory (MCT) of glass-forming liquids [165, 166] and of families of models generically referred to as “kinetically constrained models" [167, 168].

A different approach is based on the idea the understanding glass formation only requires identifying the relaxation mechanism that is dominant as the liquid enters the viscous regime. An example of this perspective is represented by the so called *elastic models* [4]. In these models, the height of the barrier for a “flow event", i.e., a molecular rearrangement, which is supposed to be a fast event, could be determined by liquid properties that can be probed on a short time scale. The first paper suggesting this idea is a papers by Tobolsky et al. [169]. In this scenario, the liquid viscosity is controlled by the rate of molecules moving from one position equilibrium to another. The energy barrier to be overcome can be estimated by the intersection of the harmonic approximations of the potential in the minima (see Figure 5.1). Estimated barriers, despite being clearly larger than the actual barriers, are proportional to

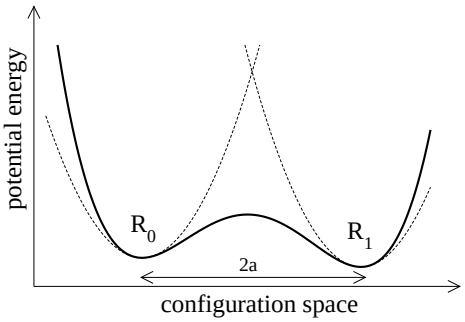

Figure 5.1: Schematic representation of two potential energy minima, indicated as R_0 and R_1, at a distance $2a$. The full curve is the potential energy and dashed line are the estimation via second-order Taylor expansions around the minima. It is apparent that the estimated barrier is considerably larger than actual barrier. However estimated and actual barriers are proportional.

the latter. The rate theory [170] states that the average time between jumps τ is proportional to a microscopic time τ_0 divided by the statistical mechanical probability to find the system around the energy maximum. In the harmonic approximation the energy is quadratic in the reaction coordinate, resulting in a Gaussian probability distribution $\propto \exp(-x^2/2\langle x^2\rangle)$ where x is the distance from the minimum in the reaction coordinate and $\langle x^2\rangle$ the mean square amplitude of vibrations. This leads to

$$\tau = \tau_0 \exp\left(\lambda_1 \frac{a^2}{\langle x^2\rangle}\right) \tag{5.1}$$

where λ_1 is a factor of order one and a the average intermolecular distance. If one define the temperature-dependent activation (free) energy ΔE via the relation $\tau(T) = \tau_0 \exp(\Delta E(T)/k_B T)$, then

$$\Delta E \propto k_B T \frac{a^2}{\langle x^2\rangle} \tag{5.2}$$

For most glass-forming liquids $\langle x^2\rangle$ decreases faster than T upon cooling, resulting in an activation energy that increases upon cooling.

In ref. [169], the authors also argued that the important potential is that resisting to shear deformation and so $\Delta E \propto G$ where G is the liquid shear modulus. As a liquid has a vanishing dc modulus, the instantaneous or infinite frequency shear modulus G_∞ is the relevant quantity, leading to

$$\Delta E \propto a^3 G_\infty \tag{5.3}$$

The microscopic volume a^3 comes from a dimensional analysis.

In ref. [171], eq 5.3 is derived starting from the Maxwell relation $\tau = \eta/G_\infty$ and using known expression for the viscosity [172] and for the relaxation time [173].

A breakthrough in the field of elastic models is represented by the *shoving model*, proposed by Dyre and coworkers [174, 175]. The starting point is that, due to the harsh intermolecular repulsion, a molecular rearrangement requires very high energy if this occurs at constant region volume. So it is more favorable for the molecules to spend some energy on shoving aside the surrounding liquid. The three main assumptions of the shoving model are: (i) elastic energy is the dominant contribution in the activation energy; (ii) this elastic energy is mainly located in the surroundings of the flow event; (iii) the elastic energy is mainly shear elastic energy. Then the activation energy is given by:

$$\Delta E(T) = G_\infty(T) V_c \tag{5.4}$$

The characteristic volume V_c is assumed to be temperature independent. If one suppose that the region of rearranging molecules is approximately spherical and that the radius must increase by Δr before a flow event has a fair chance of taking place, then $V_c = 2(\Delta V)^2/3V$ where $V = 4/3\,\pi r^3$ is the volume before the shoving and $\Delta V = 4\pi r^2 \Delta r$. In this picture, the T-dependence of the activation energy is entirely controlled by G_∞.

For the relaxation, the shoving model gives:

$$\tau = \tau_0 \exp\left(\frac{G_\infty(T) V_c}{k_B T}\right) \tag{5.5}$$

Hence, according to eq 5.5, the logarithm of the viscosity depends linearly on G_∞/T (see Appendix C for a complete derivation of eq 5.5).

A connection with eq 5.2 can be made [4]. If one assumes harmonic vibrations with a single force constant written as $m\omega_0^2$, then, from the classical equipartion theorem, $a^2/\langle x^2\rangle \propto ma^2\omega_0^2/k_BT$. ω_0 is an effective frequency that may depend on temperature. In this "single-force-constant model" the transverse and longitudinal sound velocities are proportional and $c_\infty \propto a\omega_0^2$. This implies that $a^2/\langle x^2\rangle \propto mc_\infty^2/k_BT$ and then:

$$\frac{\Delta E}{k_B T} \propto \frac{a^3 G_\infty}{k_B T} \propto \frac{a^2}{\langle x^2\rangle} \tag{5.6}$$

Then the vibrational mean square amplitude $\langle x^2\rangle$ is expected to be proportional to the quantity G_∞/k_BT.

According to eq 5.5, the key quantity of the elastic models is the shear modulus G_∞. It is useful to say a few words about this quantity. In ref. [174] Dyre and coworkers define explicitly G_∞ via the relation $\lim_{\omega\to\infty} G(\omega) = G_\infty$ without any further clarification. In the following papers [4, 175] G_∞ is always referred as the "instantaneous" or "infinite-frequency" shear modulus. However, by carefully reading the papers [174, 175], it appears that G_∞ has to be understood not as the formal infinite-frequency shear modulus but rather as a high-frequency shear modulus, namely the modulus probed at frequency ω which is high enough to ensure that the structure does not relax ($\omega \gg \tau^{-1}$), but is still lower than phonon frequencies. Denoting this high-frequency modulus with G_∞, as well as the real infinite-frequency modulus can generate confusion.

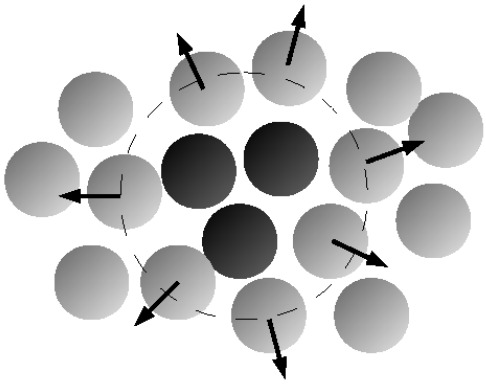

Figure 5.2: A flow event, i.e., a molecular rearrangement, in the picture of the shoving model with dark sphere representing the molecules before the rearrangement. The flow event takes place if, due to thermal fluctuations, the region volume expands sufficiently. According to the statistical mechanics, the probability of this happening is controlled by the reversible work done on the surrounding fixed structure to bring about the same expansion. This quantity can be calculated using standard solid-state elasticity theory: in the simplest case of spherical symmetry, the surrounding molecules are subjected to a pure shear deformation and the activation energy is proportional to $G_\infty(T)$.

Elastic models, and in particular the shoving model, were discussed in experimental [176–185], theoretical [186, 187] and computational [179] work in a wide class of materials including colloids, liquids, polymers and metallic alloys. Different experimental techniques probe the liquid elastic properties at different frequencies. Piezo-ceramic method is able to provide shear modulus data in the frequency range $1\,mHz - 50\,kHz$. Ultrasonic measurement gives data in the MHz range. Higher frequencies, in the GHz range, are obtained with Brillouin light scattering. However, it is not obvious that frequencies in these range are high enough to ensure that G_∞ is really measured.

5.2 The numerical model

A coarse-grained model of a melt of linear, fully flexible, unentangled polymer chains with M monomers each is used. The system has $N = 2000$ monomers in all cases, but $M = 3$, where $N = 2001$. Nonbonded monomers interact via a truncated parametric potential, whose attractive and repulsive steepness can be modulated. Bonded monomers interact with a potential that is the sum of the finitely extendible nonlinear elastic (FENE) potential and the Lennard-Jones (LJ) potential, resulting in a fluctuation of a few percent in the bond length.

All the polymer data are in reduced units: length in units of σ, temperature in units of ϵ/k_B and time in units of $\sigma(\mu/\epsilon)^{1/2}$, where σ and ϵ are given by nonbonding potential and μ is the monomer mass. We set $\mu = k_B = 1$.

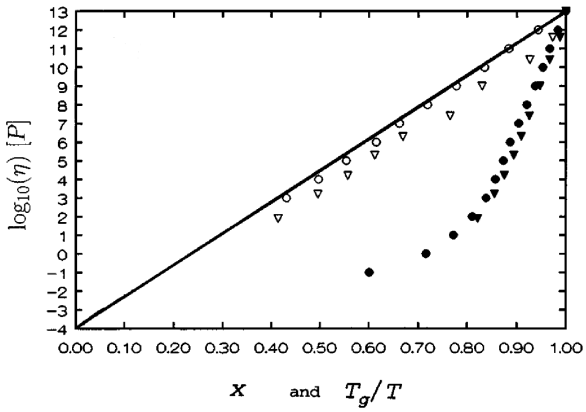

Figure 5.3: Logarithm of the viscosity, expressed in Poise, as a function of inverse temperature (full symbols) and as a function of $X \propto G_\infty/T$ for 5-phenyl-4-ether (◯) and α-phenil-*o*-cresol (▽). Both x-axis variables are normalized to 1 at T_g. Data were obtained from depolarized Brillouin scattering in the GHz range. (reprinted from [174])

States with different values of the temperature T, the density ρ, the chain length M, and the steepness p, q of the monomer-monomer interaction potential are studied. Each state is labelled by the multiplet $\{M, \rho, T, p, q\}$.

Full details about the model, the considered states and the simulation technique are given in Appendix A.

5.3 Results and discussion

5.3.1 Instantaneous elasticity

Here the correlation between **real** infinite frequency elasticity and structural relaxation is investigated. In fact, also due to the ambiguous notation discussed above, one may wonder a bit whether elastic models should predict a correlation between these properties [188].

In equilibrium fluids the infinite frequency shear modulus G_∞ can be expressed by the zero-time correlation function [189, 190]:

$$G_\infty = \frac{V}{k_B T}\langle \sigma_{xy}^2 \rangle \tag{5.7}$$

σ_{xy} is the off-diagonal component of the stress tensor in the atomic representation[1] [191]:

$$\sigma_{\alpha\beta} = \frac{1}{V}\left(\sum_{i=1}^{N}\left[m v_{\alpha i} v_{\beta i} + \frac{1}{2}\sum_{j\neq i} r_{\alpha ij} F_{\beta ij}\right]\right) \tag{5.8}$$

[1] in principle, the stress tensor may be also written in the molecular representation in terms of the centre of mass position and momentum of the polymeric chain, together with internal parameters [191]. These two representations are hydrodynamically equivalent, e.g. to evaluate transport coefficients. However, there are differences - especially at short times - between the atomic and the molecular stress correlation functions [191].

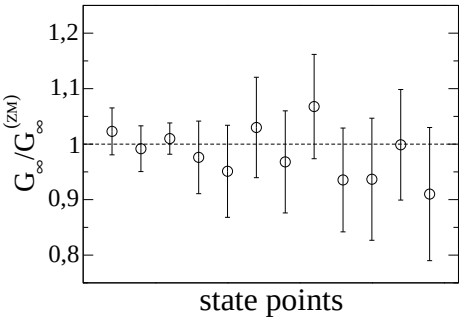

Figure 5.4: Comparison of G_∞, as evaluated from the zero-time shear stress correlation function, with the two-body expression $G_\infty^{(ZM)}$ of ref. [189], for selected state points of the polymer model. The two results are coinciding within the errors. Selected cases (M, ρ, T, p, q) from left to right: (2, 1.086, 0.7, 7, 6), (3, 1.086, 0.7, 7, 6), (10, 1.086, 0.7, 7, 6), (2, 1.033, 0.7, 10, 6), (3, 1.039, 0.7, 11, 6), (2, 1.033, 0.5, 10, 6), (3, 1.056, 0.7, 12, 6), (5, 1.033, 0.6, 12, 6), (3, 1.086, 0.7, 12, 6), (5, 1.086, 0.7, 12, 6), (10, 1.086, 0.7, 12, 6) and (2, 1.0, 0.7, 12, 11). Corresponding relaxation times change from 1 to about 10^3.

where $v_{\alpha k}$, $F_{\alpha kl}$ and $r_{\alpha kl}$ are the α components of the velocity of the k-th monomer with mass m, the force between the kth and the lth monomer and their separation, respectively. The symbol $\langle ... \rangle$ represents the canonical average.

In ref. [189], Zwanzig e Mountain derived an expression for the infinite frequency shear modulus in terms of the pair distribution function $g(r)$

$$G_\infty^{(ZM)} = \rho k_B T + \frac{2\pi}{15}\rho^2 \int_0^\infty dr g(r) \frac{d}{dr}\left[r^4 \frac{d\phi}{dr}\right] \tag{5.9}$$

where $\phi(r)$ is the two body interaction potential.
In Figure 5.4 the equivalence between eq 5.7 and eq 5.9 is explicitly tested for selected case of the polymer model, with different chain length, density, temperature and potential, exploring a range of relaxation time from 1 to 10^3. The two expression of G_∞ are coinciding within the errors.

Now we investigate the correlation of elastic properties with the structural relaxation time τ_α, defined via the relation $F_s(q_{max}, \tau_\alpha) = 1/e$. Figure 5.5 compares the latter quantity with the ratio G_∞/T. It is apparent that G_∞ poorly correlates with the structural relaxation time. Moreover, it is interesting to consider the temperature dependence of G_∞ (see the inset of Figure 5.5). If the temperature decrease, the shear modulus decrease, roughly in a linear way. This agrees with previous findings on binary soft sphere in two [192] and three dimensions [193]. The observed T-dependence of G_∞ is in clear contrast with the expected increase of the shear modulus upon cooling, which is the basis of the super-Arrhenius slow-down in glass-forming liquids according to elastic models [4].

Then we consider the short-time mean square displacement (ST-MSD) $\langle u^2 \rangle$, introduced in section 2.1.2 and defined via the relation $\langle u^2 \rangle = \langle r^2(t^*) \rangle$

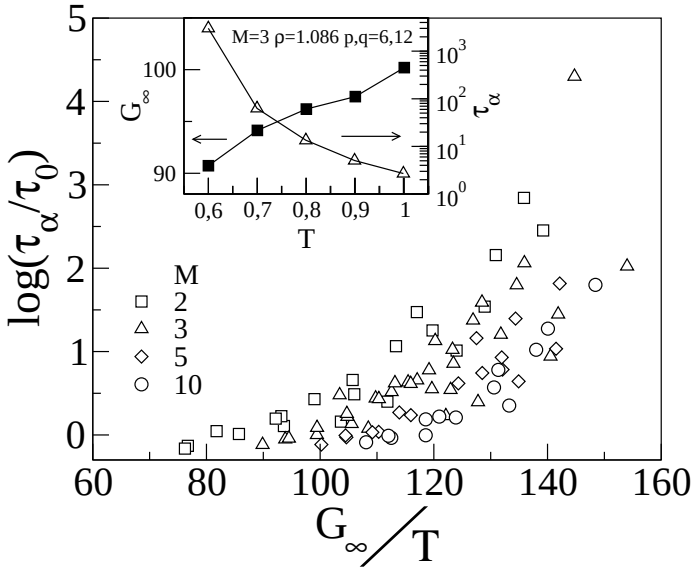

Figure 5.5: The structural relaxation time τ_α versus the ratio G_∞/T from MD simulations. It is apparent that G_∞ poorly correlates with the structural relaxation time. Inset: temperature dependence of G_∞ (full symbols) and structural relaxation time τ_α (open symbols) for states with chain length $M = 3$, density $\rho = 1.086$ and interaction potential $p, q = 6, 12$. Note the opposite behavior of G_∞ and τ_α: as temperature decreases, τ_α increases but G_∞ decreases.

where t^* is time corresponding to the minimum of the $\log - \log$ derivative of $\langle r^2(t)\rangle$. In Figure 5.6 the ST-MSD as a function the quantity G_∞/T is shown. Note that the ST-MSD, which is evaluated at very short time, few picoseconds in real time, is proper of fast dynamics, as well as the elastic modulus G_∞. Nevertheless, no clear correlation is observed between $\langle u^2\rangle$ and G_∞/T.

At this point, we are in the position to conclude that the infinite frequency shear modulus that does not seem to play a relevant role in the mechanism that controls the relaxation in the present polymer model.

5.3.2 Transient elasticity

In the previous section the infinite frequency elastic response was considered. Here the time dependence of the elastic properties are investigated.

First the transient shear elastic modulus $G(t)$ of a volume V is defined via the relation:

$$G(t) = \frac{V}{k_B T}\langle \sigma_{xy}(t_0)\sigma_{xy}(t_0 + t)\rangle \tag{5.10}$$

where the off-diagonal component of the stress tensor is defines in eq 5.8. Note that $G(0) = G_\infty$. Figure 5.7 compares the incoherent intermediate scattering function (ISF) $F_s(q_{max}, t) = N^{-1}\langle \sum_{i=1}^{N} \exp\{-i\mathbf{q}\cdot[\mathbf{r}_i(t) - \mathbf{r}_i(0)]\}\rangle$ and and $G(t)$. For clarity reasons, fast oscillations of $G(t)$, due to rapid vibrations

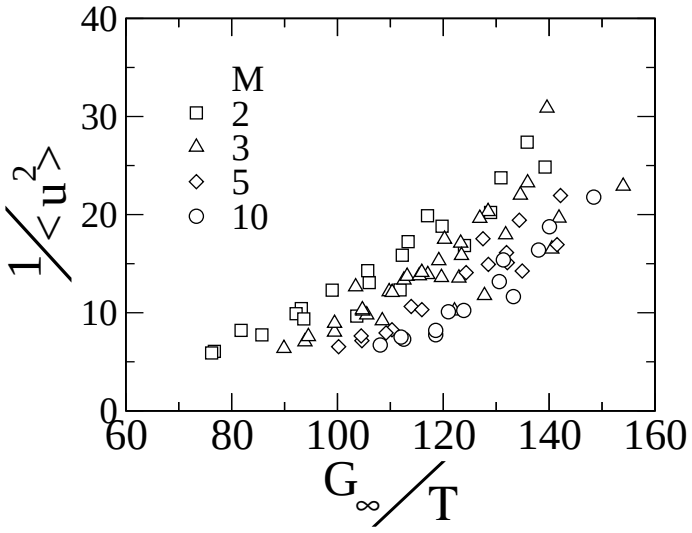

Figure 5.6: The ST-MSD $\langle u^2 \rangle$ versus the ratio G_∞ / T from MD simulations. It is apparent that G_∞ poorly correlates with the structural relaxation time.

of the stiff bonds [194, 195], which are apparent within 0.5 time units, are removed by running averages with time window of about 0.15 time units.

Fig.5.7 shows the characteristic two-step decay of both $G(t)$ (top) and ISF (bottom). A first drop of both $G(t)$ and ISF over times $t \sim 1$, corresponding to a few picoseconds in real time [25], is apparent. Within a unit lapse of time the trapped monomers explore the cage of their first neighbors with incipient escape tendency. This was seen by observing the monomer mean square displacement $\langle r^2(t) \rangle$ which exhibits a well-defined minimum of the logarithmic derivative quantity $\Delta(t) \equiv \partial \log \langle r^2(t) \rangle / \partial \log t$ at $t^\star = 1.023$ [25, 26]. Since this quantity vanishes in the case of perfect trapping, i.e., $\langle r^2(t) \rangle \sim const$, the minimum signals the full exploration of the cage and the onset of early escape events ($t^\star$ is independent of the physical state in the present model). The cage exploration results in the fast, large drop of $G(t)$ from G_∞ to G_p, i.e., the plateau shear modulus measured by most viscoelastic experiments [186]. It seems proper to deepen the discussion about this point. In crystals with one particle per unit cell under athermal conditions the equality $G_p = G_\infty$ holds [196]. Differently, even under athermal conditions, in crystals with multi-atom unit cell [196] and amorphous systems [197–199] the total force on each particle unbalances ($F_{tot} \neq 0$) after the fast, homogeneous, affine shear strain. At finite temperature the mechanical equilibrium is restored rapidly by the non-affine particle displacements within their cages, leading to considerable loss of elastic energy [197–199]. Note that the differences between G_p and G_∞ are reduced but not suppressed in the glass for $T < T_g$ since local cage rattling is still present [38].

We now show that the monomer displacements within times $t^\star$ recover the mechanical equilibration which is missing in the instantaneous elastic re-

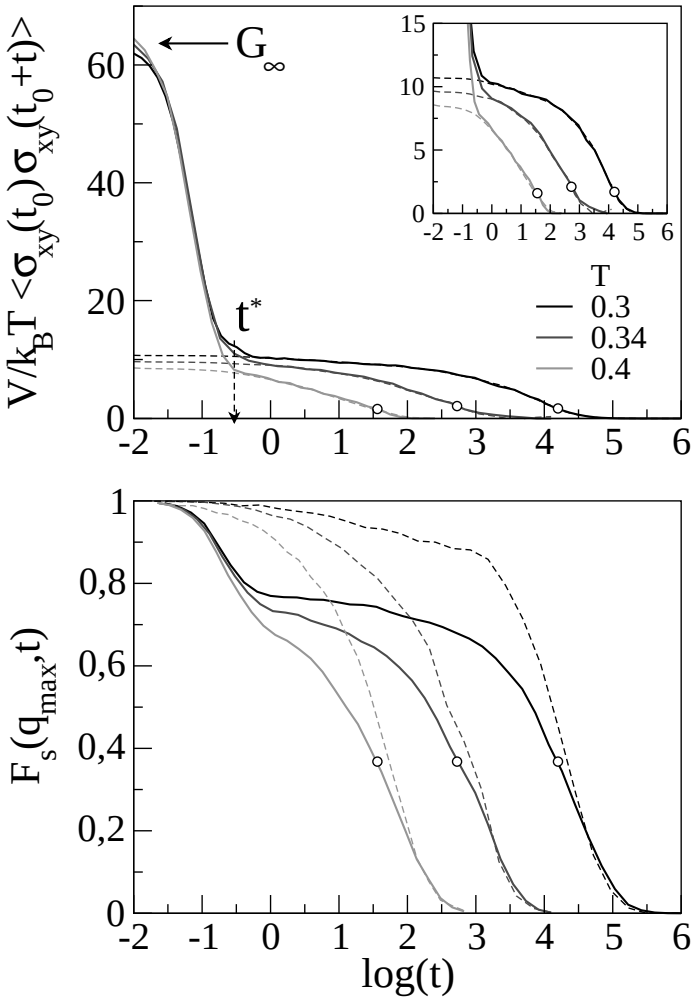

Figure 5.7: MD results of the relaxation properties of linear chains with $M = 3, \rho = 0.984$ at the indicated temperatures. Non-bonded monomers interact with the Lennard-Jones potential. Both Newtonian (full lines) and inherent (dashed lines) dynamics are considered. Dots mark the structural relaxation time τ_α. Top Panel: transient elastic modulus $G(t)$. Note that $G(0) = G_\infty$. The inset magnifies the plateau region at intermediate times. The plateau modulus is defined by $G_p \equiv G(t^\star)$, t^* is defined in the text. Bottom Panel: intermediate scattering function $F_s(q_{max}, t)$.

Table 5.1: Comparison between the inherent and the newtonian elastic modulus $G(t)$ and ISF at initial time and $t^\star$ (the q-dependence of ISF is understood for clarity reasons). Data refer to the states plotted in Fig.5.7.

T	$\log \tau_\alpha$	$1 - F_s^{IS}(t^\star)$	$\frac{1-F_s^{IS}(t^\star)}{1-F_s(t^\star)}$	$\frac{G^{IS}(0)-G_p}{G^{IS}(0)}$	$\frac{G^{IS}(0)-G_p}{G_\infty-G_p}$
0.3	4.2	0.02	$8.7 \cdot 10^{-2}$	$4.7 \cdot 10^{-2}$	$9.6 \cdot 10^{-3}$
0.34	2.73	0.03	0.12	$5.7 \cdot 10^{-2}$	$1.0 \cdot 10^{-2}$
0.4	1.56	0.09	0.28	0.22	$3.2 \cdot 10^{-2}$

sponse. To this aim, the configurations explored by the system via the true Newtonian dynamics are sampled in time and "quenched" to the so-called inherent structures (IS) by locally minimizing the potential energy in configurational space, i.e., enforcing mechanical equilibrium (vanishing total force on each monomer, $\mathbf{F}_{tot} = 0$) [3]. The IS time series defines the "inherent" dynamics of the system which, roughly, subtracts from the true Newtonian dynamics the vibrational motion around the IS. Henceforth, the quantity $X(t)$ will be denoted as $X^{IS}(t)$ if evaluated in terms of the IS occupied at time t. Fig.5.7 (top) shows that $G(t)$ and $G^{IS}(t)$ differ at very short times but they coincide from about $t^\star$ onwards where one observes the plateau G_p revealed by most viscoelastic experiments [186, 190, 193, 200].
For convenience we define

$$G_p \equiv G(t^\star) = G^{IS}(t^\star) \tag{5.11}$$

The coincidence of $G(t)$ and $G^{IS}(t)$ for $t \gtrsim t^\star$ evidences that the decay of the plateau is due to a series of successive jumps from one equilibrated IS structure to a new one, most probably by crossing over the large energy barriers between different metabasins (a metabasin is a group of ISs separated by small energy barriers [3, 142]). Obviously, $G(t)$ vanishes within the structural relaxation time τ_α (Fig. 5.7 top). Note also that $G(\tau_\alpha)$ is approximately state-independent. It is worth noting that G_p and G_∞ have quite different temperature dependence. Fig.5.7 (top) shows that, while G_p decreases by increasing the temperature, G_∞ does increases, as reported elsewhere [193].

Figure 5.7 (bottom) compares the true ISF, $F_s(q_{max}, t)$, with the one evaluated in terms of IS dynamics, $F_s^{IS}(q_{max}, t)$. It is seen that the subtraction of the vibrational dynamics around IS removes the initial drop and the plateau seen in $F_s(q_{max}, t)$ at intermediate times [26]. Note that $F_s(q_{max}, t)$ and $F_s^{IS}(q_{max}, t)$ coincide only at times a little bit longer than τ_α, as it is reported for binary mixtures [201].

Now we investigate if, during the initial mechanical equilibration, transitions between different ISs take place and how they affect both the density and the stress relaxation. To clarify the issue Table 5.1 presents some relevant features of the stress and the structure relaxation of the representative states plotted in Fig.5.7. First, the number of IS transitions within $t^\star$ is compared with the ones needed to complete the structural relaxation. A rough estimate of their ratio is given by the quantity $1 - F_s^{IS}(t^\star)$, which is about a few percents

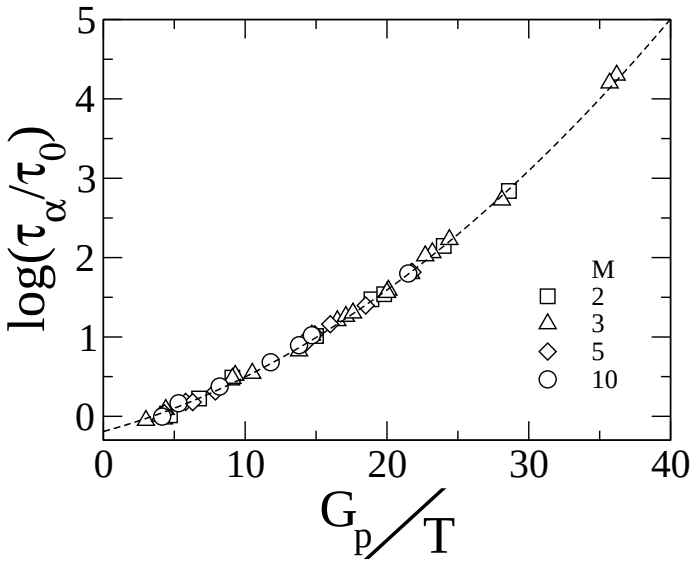

Figure 5.8: The structural relaxation time τ_α versus the ratio G_∞/T from MD simulations. Unlike what seen with the infinite frequency modulus G_∞, high correlation between τ_α and G_p/T is observed. Dashed line is eq 5.12, $\log \tau_\alpha = A + B(G_p/T) + C(G_p/T)^2$. Best fit of data gives $A = -0.191(8)$, $B = 0.048(3)$ and $C = 0.0020(1)$.

for the slowest states (Table 5.1, third column). Note that the initial change of $F_s(t)$ is much larger than the corresponding one of $F_s^{IS}(t)$ (Table 5.1, fourth column), i.e., the vibrational dynamics affects the initial relaxation more effectively, especially at low temperature. The IS transitions at early times result in relative changes of the inherent elastic modulus which are about two times larger than the corresponding ones of $F_s^{IS}(t)$ (compare the third and fifth columns of Table 5.1). This is roughly consistent with the approximate relation $G(t) \sim F_s(q_{max}, t)^2$ drawn by the mode-coupling theory [202, 203]. However, in spite of the quadratic influence of the density relaxation, the stronger process affecting the stress relaxation at early times is the vibrational dynamics around each IS, as it may be seen by the ratio $(G^{IS}(0) - G_p)/(G_\infty - G_p)$ in Table 5.1 and the direct inspection of Fig.5.7 (top).

At this point we investigate the correlation of residual elasticity with both the ST-MSD and τ_α. First the structural relaxation is considered. In Figure 5.8 the structural relaxation time τ_α versus the ratio G_p/T is shown. Unlike what seen with the infinite frequency modulus G_∞, high correlation between τ_α and G_p/T is observed. The resulting master curve in reduced units is well described by the quadratic law:

$$\log(\tau_\alpha) = A + B\left(\frac{G_p}{T}\right) + C\left(\frac{G_p}{T}\right)^2 \tag{5.12}$$

with $A = -0.191 \pm 0.008$, $B = 0.048 \pm 0.003$, $C = 0.0020 \pm 0.0001$. Notice that the replacement $G_\infty \to G_p$ in eq 5.5 still results in a rather poor fit of the MD results

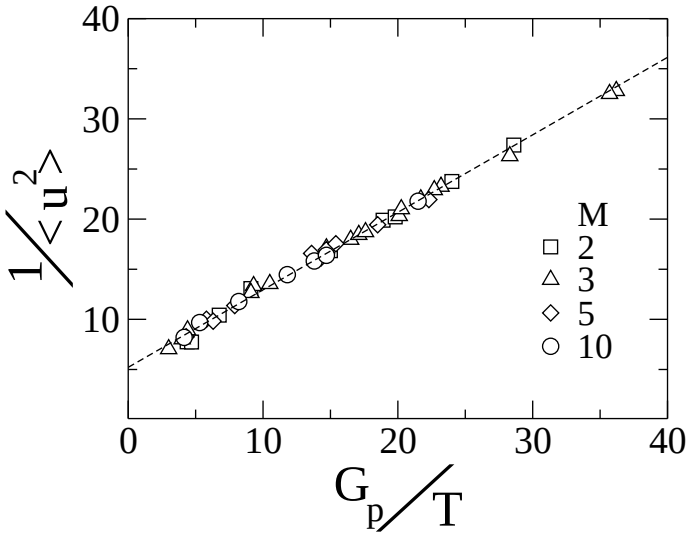

Figure 5.9: The ST-MSD $\langle u^2 \rangle$ versus the ratio G_∞/T from MD simulations. Dashed line is $\langle u^2 \rangle^{-1} = \langle u_0^2 \rangle^{-1} + a^* G_p/T$ with $\langle u_0^2 \rangle = 0.192(4)$ and $a^* = 0.77(2)$. The investigated states, obtained by changing T, ρ, and the interacting potential between non-bonded monomers are listed in Appendix A.

Then the ST-MSD is considered: Figure 5.9 compares G_p and $\langle u^2 \rangle$. Very high correlation between G_p and $\langle u^2 \rangle$ is found. In particular, a linear scaling law between the ratio G_p/T and the inverse of the ST-MSD is found:

$$\frac{1}{\langle u^2 \rangle} = \frac{1}{\langle u_0^2 \rangle} + a^* \frac{G_p}{T} \tag{5.13}$$

Best-fit gives $\langle u_0^2 \rangle = 0.192(4)$ and $a^* = 0.77(2)$.

To provide insight into eq 5.13 we may resort the potential-energy landscape viewpoint. In this picture, the so-called inherent structures (IS), i.e., the configurations corresponding to minima of the potential energy, are grouped to form distinct metabasins (MB) separated by high energy barriers [204]. We can 5.13 interpret the two terms of eq 5.13, $\langle u_0^2 \rangle$ and the "elastic" ST-MSD $T/G_p a^*$ as the average MB full width (or approximately the MSD to reach a different MB), and the typical MSD within an MB, respectively. In fact, for a binary mixture the typical MSD within an MB ($\simeq 6 \cdot 10^{-2}$) and to reach a different MB ($\simeq 0.2$) [205] are rather comparable, at the same $\tau_\alpha \simeq 4 \cdot 10^3$, to the "elastic" ST-MSD ($\simeq 4.5 \cdot 10^{-2}$) and $\langle u_0^2 \rangle \simeq 0.192$ of the monomers, respectively.

The master curve of eq 5.13 is built with polymer states with different temperature, density, chain length and the interacting potential between non-bonded monomers. The constancy of the parameters $\langle u_0^2 \rangle$ and a^*, as long as A, B and C in eq 5.12, is ascribed to the limited changes of the local structure due to the high packing of the investigated states [98].

5.3.3 An extended elastic model

Now we introduce a theoretical framework to interpret the results of MD simulations. The following derivation is conceptually equivalent to the one presented in ref. [26]. We start from the key equation of the elastic models:

$$\tau_\alpha^{(EM)} = \tau_0 \exp\left(\frac{GV^*}{k_B T}\right) \tag{5.14}$$

One basic assumption of standard elastic models is that the activation volume has a characteristic value V^*. To expand this concept, we assume that the volume is dispersed. To model the related distribution, it is assumed that the latter does not depend on the state parameters such as the temperature, the density or the interacting potential. A suitable choice is to take the distribution of the activation volume as a truncated Gaussian form:

$$\mathcal{P}(V^*) = \begin{cases} A \exp\left(-\frac{(V^*-\overline{V^*})^2}{2\sigma_{V^*}^2}\right) & \text{if } V^* > V^*_{min} \\ 0 & \text{otherwise} \end{cases} \tag{5.15}$$

where A is the normalization constant and V^*_{min} is the minimum value of the activation volume. Averaging eq 5.14 over the distribution given by eq 5.15, yields the following generalized equation:

$$\tau_\alpha = \int_0^\infty \tau^{(EM)}(V^*)\mathcal{P}(V^*)dV^* \tag{5.16}$$

$$= B \cdot \mathcal{N}\left[\frac{G}{k_B T}\right] \cdot \exp\left(\frac{G\overline{V^*}}{k_B T} + \frac{G^2\sigma_{V^*}^2}{4k_B^2 T^2}\right) \tag{5.17}$$

where B is a constant and the normalization factor $\mathcal{N}\left[\frac{G}{k_B T}\right]$ produced by the truncation reads:

$$\mathcal{N}\left[\frac{G}{k_B T}\right] = \frac{1 + \mathrm{Erf}\left[\frac{(\overline{V^*}-V^*_{min})/\sigma_{V^*}+\sigma_{V^*}/2\left(\frac{G}{k_B T}\right)}{\sqrt{2}}\right]}{1 + \mathrm{Erf}\left[\frac{(\overline{V^*}-V^*_{min})/\sigma_{V^*}}{\sqrt{2}}\right]} \tag{5.18}$$

If $\overline{V^*} \geq V^*_{min}$, $1 \leq \mathcal{N}\left[\frac{G}{k_B T}\right] \leq 2$ namely $\mathcal{N}\left[\frac{G}{k_B T}\right]$ depends very weakly on the ratio $\left(\frac{G}{k_B T}\right)$ and the truncation is negligible. Then $\tau_0 \equiv B \cdot \mathcal{N}\left[\frac{G}{k_B T}\right]$ and eq 5.17 become:

$$\tau_\alpha = \tau_0 \exp\left(\frac{G\overline{V^*}}{k_B T} + \frac{G^2\sigma_{V^*}^2}{4k_B^2 T^2}\right) \tag{5.19}$$

Eq 5.19 predicts a quadratic dependence of the structural relaxation time on the ratio $\frac{G}{k_B T}$ which agrees with the findings of the simulations discussed in the previous section. Moreover, the good quality of the scaling justifies the assumption of the independence of distributions $\mathcal{P}(V^*)$ on the state parameters. Both the average value $\overline{V^*}$ and the spread σ_{V^*} can be obtained by comparing eq 5.19 with eq 5.12, resulting in $\overline{V^*} = 4.8(3) \cdot 10^{-2}$ and $\sigma_{V^*} = 7.0(1) \cdot 10^{-2}$.

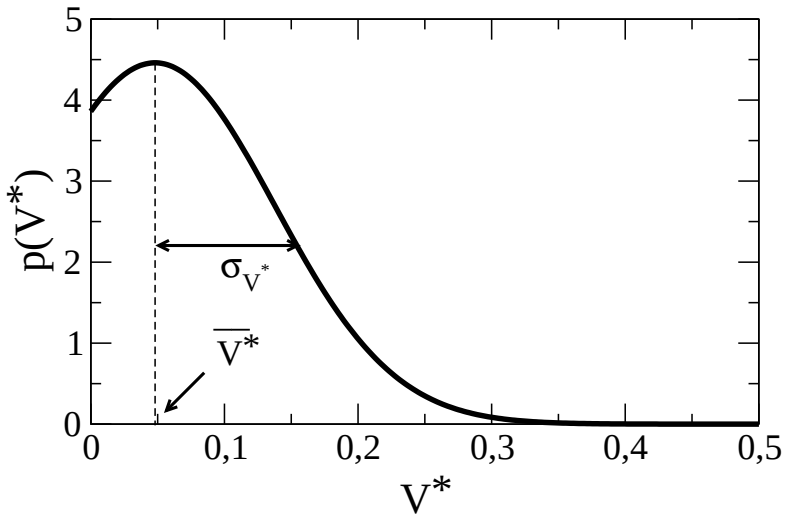

Figure 5.10: The distribution $\mathcal{P}(V^*)$ of the activation volume for a flow event is plotted using the values for $\overline{V^*}$ and $\sigma^2_{V^*}$ obtained from MD simulations. We fixed $V^*_{min} = 0$ to avoid meaningless negative values for V^*.

The concavity of the master curve eq 5.12 is a signature of the heterogeneity, i.e., the existence of a distribution of the activation volume for the flow events (in Figure 5.10 we plot the distribution $\mathcal{P}(V^*)$ with the values of $\overline{V^*}$ and σ_{V^*} from MD simulations).

An expression similar to eq 5.19 was already reported for both supercooled liquids [10] and polymers [206]. This support the choice of the Gaussian form for $\mathcal{P}(V^*)$.

5.3.4 Comparison with simulations and experiments from literature

Now we want to investigate if the MD results are robust enough to be compared with the experiments. Virtually, all the experiments validating the shoving model actually measure G_p since the elastic response is probed at frequencies much lower than the THz range where the crossover from G_∞ to G_p is located [186].

The fact that eq 2.2, assessed in the weakly supercooled regime attainable by MD simulations, holds true down to the glass transition evidences that the relevant information on the coupling between the fast dynamics and the long-time relaxation is present at high temperatures [25]. This motivated to extend the validity of eq 5.12 down to the glass transition. The GT structural relaxation time $10^2\,s$ in real units is equivalent to $10^{13} - 10^{14}$ in MD units.
Having defined the GT in MD simulation, the ratio $G_{p,g}/T_g$ can be obtained by extrapolation:

$$\frac{G_{p,g}}{T_g} = 70.9$$

If we define the reduced variable $X = \left(G_p T_g\right) / \left(G_{p,g} T\right)$, we obtain a quadratic form as candidate for the universal master curve:

$$\log\left(\tau_\alpha / \tau_0\right) = \delta + \epsilon X + \phi X^2 \tag{5.20}$$

with

$$\begin{aligned} \delta &= -11.70(1) \\ \epsilon &= B \cdot G_{p,g}/T_g = 3.4(2) \\ \phi &= C \cdot (G_{p,g}/T_g)^2 = 10.3(8) \end{aligned}$$

δ is set so as to get the familiar $\log(\tau_\alpha/\tau_0) = 2$ at GT.

The boundaries of eq 5.20 can be determined considering the uncertainty on t^*, the time at which both the ST-MSD $\langle u^2 \rangle$ and the plateau modulus G_p are measured. Varying t^* within its confidence interval ($0.6 - 1.4$ [25]), different values of the ratio $G_{p,g}/T_g$ are found. In particular for t^* equal to 0.6 and 1.4, $G_{p,g}/T_g$ is respectively 65.6 and 80.5.

Figure 5.11 shows the comparison of eq 5.20 with both simulations and experimental data of systems spanning a wide range of fragilities and elastic moduli measured at sufficiently high frequencies to allow comparison with τ_α and η over wider ranges (data details and sources are listed in Table 5.2). Elastic response is observed if the experiments probe a time scale in which the liquid has no time to relax so that it behaves like a solid, i.e., $\omega\,\tau_\alpha \gg 1$. The order of magnitude of ω can be changed by using different techniques, such as ultrasonic measurement for the MHz range and Brillouin scattering for the GHz range. For this reason, elastic moduli measured at frequency ω are considered only in the region $\omega > \max\{0.1/\tau_\alpha, 2\pi \cdot 1MHz\}$. The experimental data are vertically shifted to adjust the conversion factor between MD and real units in order to ensure best-fit with eq 5.20. No other adjustment was made. Data shifts τ_0 are listed in Table 5.2.
From Figure 5.11, we observe that all the experimental data collapse on the master curve defined by eq 5.20, within the indicated accuracy. To get further insight, we compare the validity of eq 5.20 with the that of the standard prediction of the shoving model, eq 5.5, where G_∞ is virtually replaced by G_p. Note that, in addition to the vertical shift, the modified version of eq 5.5 has one more adjustable parameter, the volume V_c, with respect eq 5.20. In Figure 5.12 we plot the reduced chi-square $\tilde{\chi}^2$ of the experimental data with both the quadratic form eq 5.20 and the modified eq 5.5, over the variable range from $\log \tau_\alpha^{(min)}/\tau_0$ up to $\log \tau_\alpha^{(max)}/\tau_0 = 6$. It is seen that, while the two fits are equivalent in the low temperature range $-4 \leqslant \log\,\tau_\alpha \leq 6$, eq 5.20 performs much better in the range $-12 \leq \log\,\tau_\alpha \leq -4$, in spite of the additional parameter in eq 5.5.

5.4 Conclusions and open questions

By molecular dynamics simulations of a model polymer system, the correlation of the elasticity with the structural relaxation is investigated. First the instantaneous elasticity is discussed. It is seen that both the structural relaxation

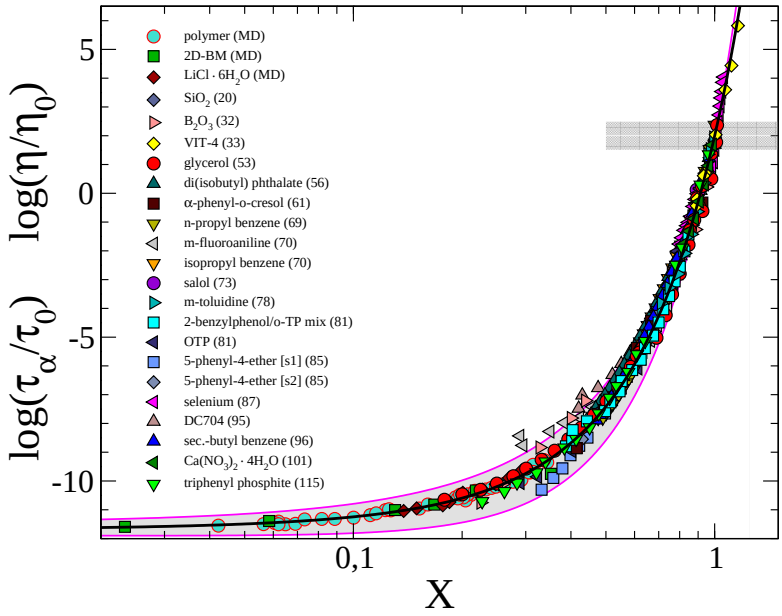

Figure 5.11: Scaling of the structural relaxation time and viscosity in terms of the reduced variable $X = \left(GT_g\right) / \left(G_g T\right)$. Black line is $\log\left(\tau_\alpha/\tau_0\right), \log\left(\eta/\eta_0\right) = \delta + \epsilon X + \phi X^2$ with $\delta = -11.70(1)$, $\epsilon = 3.4(2)$ and $\phi = 10.3(8)$ The numbers in parentheses denote the fragility of the systems (data source are listed in Table 5.2). Magenta line define the error boundaries of eq 5.20 considering $G_{p,g}/T_g$ equal to 65.6 and 80.5 once t^* is set equal to 0.6 and 1.4 respectively. The grey belt marks the GT. Elastic moduli measured at frequency ω are considered only in the region $\omega > \max\{0.1/\tau_\alpha, 2\pi \cdot 1MHz\}$.

Table 5.2: Relevant information about the investigated systems (in order of increasing fragility) and the MD simulations. $\log \tau_0$ and $\log \eta_0$ are the vertical shift factors of all the MD and the experimental data. The shear modulus G is taken from ultrasonic measurements (US) or from Brillouin scattering (BS).

System	τ_α, η			G	
	quantity	$\log(\tau_0)$ $\log(\eta_0)$	ref.	technique	ref.
Polymer	τ_α	11.5	PW	MD	PW
2D BM	τ_α	11.5	[192]	MD	[192]
$LiCl \cdot 6H_2O$	τ_α	0.2	[179]	MD	[179]
SiO_2	η	10.5	[207]	BS	[208]
B_2O_3	η	11.3	[209]	BS	[210]
Vit-4[†]	η	9.6	[182]	US	[182]
Glycerol	η	10.4	[211]	BS	[212]
di(isobutyl)phthalate	η	10.3	[213]	US	[214]
α-phenyl-o-cresol	η	9.8	[174]	BS	[174]
n-propylbenzene	η	9.6	[213]	US	[214]
m-fluoroaniline	τ_α	-0.1	[178]	BS	[178]
isopropyl benzene	η	10.3	[213]	US	[214]
Salol	τ_α	0.8	[178]	BS	[178]
m-toluidine	τ_α	0.0	[178]	BS	[178]
2-benzylphenol/*o*-TP mix.	τ_α	-0.2	[178]	BS	[178]
OTP	η	8.9	[215]	BS	[215]
5-phenyl-4-ether	τ_α	0.8	[178]	BS	[178]
5-phenyl-4-ether	η	10.5	[174]	BS	[174]
Selenium	η	11.5	[34]	US	[216]
DC704	τ_α	0.5	[178]	BS	[178]
sec.-butyl benzene	η	10.0	[213]	US	[214]
$Ca(NO_3)_2 \cdot 4H_2O$	τ_α	0.2	[178]	BS	[178]
triphenylphosphite	τ_α	-0.3	[178]	BS	[178]

[†] $Zr_{46.75}Ti_{8.25}Cu_{7.5}Ni_{10}Be_{27.5}$

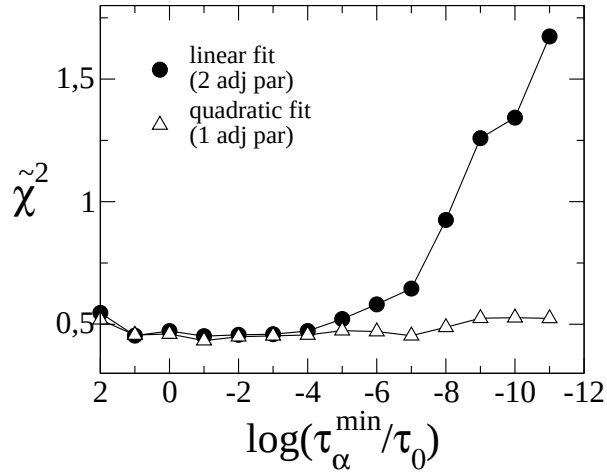

Figure 5.12: Reduced $\tilde{\chi}^2$ of the experimental data of Figure 5.11 with both the quadratic form eq 5.20 (allowing only the vertical shift of the experimental data) and the modified eq 5.5 (two adjustable parameters: V_c and the vertical shift). The fit spans the variable range from $\log \tau_\alpha^{(min)}/\tau_0$ up to $\log \tau_\alpha^{(max)}/\tau_0 = 6$.

and the fast dynamics, as described by the short time mean square displacement (ST-MSD), poorly correlate with the instantaneous elasticity, at variance with the key prediction of the standard elastic models.

Then the time dependence of the elastic response is discussed. Due to the discreteness of the matter, the nonaffine fast displacements of the particles within the cages results in the drop of the modulus from infinite frequency value G_∞ to the finite frequency plateau (or relaxed) modulus G_p. MD simulations reveal a remarkable scaling in terms of the intermediate-time elasticity. In particular, it is shown that the master curve $\log \tau_\alpha$ versus G_p/T exhibits a quadratic form not compatible with the linear prediction of the elastic models. The concavity of the master curve is ascribed to heterogeneity, i.e., a spread in the activation volume for the flow events. The scaling region includes physical states with very long τ_α and virtually pure elastic response on the picosecond time scale, whereas it extends up to high-mobility states where fast restructuring becomes apparent. Moreover, the existence of a linear scaling between the ST-MSD and G_p/T is revealed, as expressed by a "quasi-elastic" relation eq 5.13. At present time, a full understanding of eq 5.13 is missing. In this light, future work should be addressed to the search of the origin of the scaling, investigating for example the effect of early escape processes or the role of chain connectivity.

In the last part of the chapter, the master curve of $\log \tau_\alpha$ versus G_p/T is compared to simulations and experimental results from literature. It is shown that the master curve fits the experimental results over about eighteen decades in relaxation time ($-12 \lesssim \log \tau_\alpha \lesssim 6$) and a wide range of fragilities ($20 \leq m \leq 115$) with one adjustable parameter, to be compared with two adjustable parameters in the linear master curve of the standard elastic models.

Chapter 6

Outlook

In this chapter we wan to briefly summarize the main results of the studies presented in the Thesis and discuss their perspectives.

In this Thesis, we investigated through numerical simulations the dynamics and the structure in a model of fully flexible linear chains. In Chapter 2, some interesting aspects of scaling between caged dynamics and structural relaxation are discussed; in particular it is shown that the scaling can be extended up to the monomer diffusion. One of the key highlight of this study is the connection between fast dynamics and dynamical heterogeneity (DH): it is seen that the breakdown of the Stokes-Einstein equation, related to the DH, is signaled in a precise way by the monomer picosecond displacement. The role of interaction potential is discussed in Chapter 3: we show that purely repulsive potentials, despite capturing the structure, fail to reproduce the viscous slow-down of the Lennard-Jones model in molecular systems. In Chapter 4 a connection between thermodynamic and fast dynamics is made by showing that monomer picosecond displacement obeys thermodynamic scaling as well as the relaxation dynamics. On this basis an analytical expression for the scaling of relaxation time is derived, which results in an acceptable agreement with experiments. The connection between elastic properties and dynamics is discussed in Chapter 5. A well defined scaling between elastic response on the picosecond timescale and structural relaxation is evidenced. The simulation results are validated by comparison with experimental data spanning about eighteen decades in relaxation time and a wide range of fragility.

The unifying theme of the different studies presented in the Thesis is the connection between fast dynamics on the picosecond timescale and slow relaxation. The study suggests that the equilibrium and the moderately supercooled states of the glassformers possess key information on the huge slowing down of their relaxation close to the glass transition.

Below a list of open question is presented as a starting point for future studies.

- The fact that the relaxation is determined by a physical quantity, the short-time mean square displacement $\langle u^2 \rangle$ or the shear modulus G_p, which can be computed on short time scale is conceptually very close to the free-volume models [159]. This analogy is confirmed by recent

findings [26, 48]. It would be interesting to deepen the discussion of the role of the free-volume in the connection between fast dynamics and relaxation.

- In the last few years, the possible presence of localized ordered structures in liquids and polymeric systems, approaching their glass transition, has attracted an increasing interest [99, 217–219]. Although the role of the structure has been marginally treated in the present work (see Chapter 3), this topic represents an on on-going work of Leporini's group at the University of Pisa.

- The discussion about the role of the interaction potential in Chapter 3 was carried out for a single value of the density, which is, in the case of molecular systems, pretty high. However, one may wonder if higher values of density can result in a better agreement for the viscous slow-down of the Lennard-Jones model and the purely repulsive ones, especially in the case of the inverse-power-law potential. Further work should be done in this direction. It would be interesting also to consider parametric Lennard-Jones models, in which it is possible to change the steepness of both the attractive and repulsive part of the potential.

- In Chapter 5 we have discussed the time dependence of the shear modulus $G(t)$. A drop of $G(t)$, from the instantaneous value G_∞ to the plateau value G_p, over times corresponding to a few picoseconds in real time, is apparent. This is due to non-affine motion of the monomers which allow to recover the missing mechanical equilibrium. This motion may be connected with the boson peak [188] and the tunneling states which dominate the glass behavior at very low T [220]. This point should be investigated. In this sense, numerical simulations are a powerful tool since they provide easy access to G_∞.

- The shoving model [174, 221] relies on the dominance of the shear modulus for the temperature dependence of the relaxation time. Bulk modulus is assumed to play only a minor role. To what extent is this assumption correct? It would be valuable to investigate bulk effects in the framework of elastic models.

Appendix A

Numerical and data details

A.1 Numerical details

A.1.1 Models: rigid and semi-rigid polymers

Two different coarse-grained model of linear polymer are considered. In the first model, the rigid bonded chain (RB), bonded monomers are connected by a rigid bond of fixed length $b_{RB} = 0.97\,\sigma$ (in MD reduced units). In the second model, the semi-rigid bonded chain (SB), bonded monomers interact with a potential which is the sum of the finitely extendible nonlinear elastic (FENE) potential and the Lennard-Jones (LJ) potential:

$$v_{LJ}(r) = \epsilon \left[\left(\frac{\sigma^*}{r} \right)^{12} - 2 \left(\frac{\sigma^*}{r} \right)^{6} \right] \tag{A.1}$$

$$v_{FENE}(r) = -\frac{1}{2} k R_0^2 \ln \left[1 + \left(\frac{r}{R_0} \right)^2 \right] \tag{A.2}$$

where r is the monomer-monomer distance and $\sigma^* = 2^{1/6}\,\sigma$. The FENE characteristic parameters are $k = 30\,\epsilon\sigma^{-2}$ and $R_0 = 1.5\,\sigma$ [18], resulting in the average bond length $b_{SB} = 0.97\,\sigma$ with fluctuations of a few percent.

Non-bonded monomers, both in RB and SB model, interact via a truncated parametric potential:

$$v_{p,q}(r) = \begin{cases} \frac{\epsilon}{q-p} \left[p \left(\frac{\sigma^*}{r} \right)^q - q \left(\frac{\sigma^*}{r} \right)^p \right] + v_{cut} & \text{if } r \le r_c \\ 0 & \text{otherwise} \end{cases} \tag{A.3}$$

where the value of the constant v_{cut} is chosen to ensure $v_{p,q}(r_c) = 0$ at $r = r_c = 2.5\,\sigma$. Changing the p and q parameters does not affect the position $r = \sigma^*$ and the depth ϵ of the potential minimum, but only the steepness of the repulsive and attractive wings. Note that the pair $(p, q) = (6, 12)$ gives the usual Lennard-Jones potential.

All quantities are in reduced units: length in units of σ, temperature in units of ϵ/k_B (k_B is the Boltzmann constant) and time in units of $\sigma(\mu/\epsilon)^{1/2}$, where μ is the monomer mass. We set $\mu = k_B = 1$.

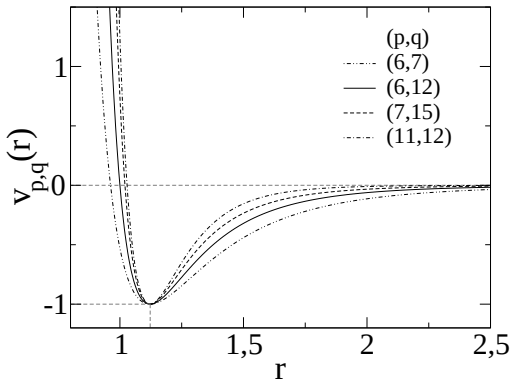

Figure A.1: The interaction potential $v_{p,q}(r)$ between non-bonded monomers. $V_{6,12}$ is the usual Lennard-Jones potential.

A.1.2 Simulation protocol

The simulation protocol to create and simulate state points of the model is the following:

1. Placement of the chains in a regular face-centered cubic (FCC) lattice preventing the dangerous effects of the overlap of monomers.

2. If the number density has not the desired value, a NPT-ensemble simulation run is performed.

3. Equilibration is performed via NVT-ensemble simulation. It is assumed that equilibration end when it is reached some multiples (from twice to ten times) of the longest relaxation time of the system, i.e., the time needed by the end-to-end correlation function $C_{ee}(t)$ to decay to less than one-tenth of its initial value.

4. NVE-ensemble production run. NVE-ensemble is chosen in order to avoid non-physical effects in the dynamics due to the presence of thermostats and pistons.

A.1.3 Algorithms

NPT and NTV ensembles are studied by the extended system method introduced by Andersen [222] and Nosé [223]. The numerical integration of the augmented Hamiltonian is performed through the multiple time steps algorithm, reversible Reference System Propagator Algorithm (r-RESPA), developed by Tuckerman *et al* [224]. In particular, the NPT and NTV operators is factorized using the Trotter theorem [225] separating the short range and long range contributions of the potential, according to the Weeks-Chandler-Andersen (WCA) decomposition [226].

The simulations have a drift of the total energy of the total energy less than $\sim 5 \cdot 10^{-8}\, \epsilon/\tau_{MD}$ and a standard deviation of the total energy less than $2 \cdot 10^{-4}$

with an integration time step $3 \cdot 10^{-3}\,\tau_{MD}$. The latter was kept constant in all the production runs but for extremal cases where $1.5 \cdot 10^{-3}\,\tau_{MD}$ was adopted to reduce the accumulation of errors on energy.

A.1.4 Inherent dynamics

Inherent structure (ISs) of the potential energy landscape (PEL) [227] are defined as the local minima of the configurational potential energy $U(\mathbf{r}^N)$ where $\mathbf{r}^N$ is the $3N$-dimensional position vector of a N-body system. To locate the relevant inherent structures of a system, instantaneous configurations, sampled from a molecular dynamics trajectory, are mapped to ISs by minimizing the potential energy along the steepest descent path. Energy minimization is carried out via the conjugate gradient (CG) algorithm [228]. The CG algorithm is a modified steepest descent technique with the successive descent directions chosen to be conjugate to preceding directions and an accurate line minimization is performed along each search direction. The CG quenches are assumed to be converged when the change in energy between two successive iterations is less than $10^{-8}\epsilon$ [229].

A.2 Data details

States with different values of the temperature T, the density $\rho = N/V$ (N is the total number of monomers and V is the volume of the cubic box) the chain length M, and the steepness p, q of the monomer-monomer interaction potential, eq A.3, are studied. Each state is labelled by the multiplet $\{M, \rho, T, p, q\}$. We had $N = 2000$ in all cases but $M = 3$ where $N = 2001$. For each case averages on at least five independent configurations are performed. For $M = 10$ the least number of independent configurations is ten. Below, the different state points are listed.

Below the considered state points are listed:

$T = 0.7$:

- $p = 6$. All the combinations with $M = 2$, 3, 5, 10, $\rho = 1.033$, 1.056, 1.086 and $q = 7$, 8, 10, 12. The case $M = 2$, $\rho = 1.086$, $q = 12$ equilibrates very slowly and was discarded.
- $p = 6$, $M = 3$. The pairs (ρ, q): $(1.090, 12)$, $(1.033, 11)$, $(1.039, 11)$, $(1.041, 11)$, $(1.045, 11)$, $(1.051, 11)$, $(1.056, 11)$, $(1.086, 11)$, $(1.033, 9)$, $(1.056, 9)$, $(1.063, 9)$, $(1.071, 9)$, $(1.079, 9)$, $(1.086, 9)$.
- $p = 5$, $q = 8$. All the combinations with $M = 2, 3, 5, 10$ and $\rho = 1.133$, 1.156, 1.186, 1.2. Furthermore, $M = 2$, $\rho = 1.033$.
- $p = 11$, $q = 12$, $M = 2$ with densities $\rho = 0.980$, 0.990, 1.0.

$T \neq 0.7$, $p = 6$:

- $T = 0.5$, $\rho = 1.033$. All the combinations with: $M = 2$, 3, 5, 10, $q = 7$, 8, 10.

- $T = 0.6$, $\rho = 1.033$. All the combinations with: $M = 2, 3, 5, 10$, $q = 8, 10$.
- $T = 0.6$, $q = 8$, $M = 3$ with $\rho = 0.95.1.056, 1, 086, 1.090$
- $q = 12$, $\rho = 1.033$, the pairs (M, T): $(2, 0.5)$, $(3, 0.5)$, $(2, 0.55)$, $(3, 0.55)$, $(2, 0.6)$, $(3, 0.6)$, $(5, 0.6)$, $(3, 0.65)$, $(5, 0.65)$, $(10, 0.65)$.
- $q = 12$, $\rho = 1.086$, the pairs (M, T): $(2, 0.75)$, $(3, 0.75)$, $(5, 0.75)$, $(10, 0.75)$, $(2, 0.8)$, $(3, 0.8)$, $(5, 0.8)$.
- $q = 12$, $\rho = 1.090$, $M = 3$, with $T = 0.75, 0.8$.

Other particular cases with $M = 3$:

- $\rho = 1.2$, $T = 0.95$, $q = 12$, $p = 6$
- $\rho = 1.1$, the triplets (T, q, p): $(0.95, 12, 6)$, $(0.9, 15, 7)$, $(1.1, 15, 7)$.
- $p = 6$, $q = 18$, the pairs (ρ, T): $(1.025, 0.8)$, $(1.025, 0.9)$ $(1.025, 1.0)$, $(1.033, 0.9)$, $(1.033, 1.0)$, $(1.033, 1.1)$, $(1.033, 1.2)$, $(1.033, 1.4)$, $(1.050, 1.0)$, $(1.050, 1.1)$, $(1.050, 1.2)$, $(1.050, 1.2)$, $(1.050, 1.3)$, $(1.050, 1.4)$, $(1.050, 1.5)$, $(1.075, 1.2)$, $(1.075, 1.3)$, $(1.075, 1.5)$, $(1.075, 1.6)$, $(1.075, 1.8)$.
- $p = 6$, $q = 24$, the pairs (ρ, T): $(0.950, 0.7)$, $(0.950, 0.8)$, $(0.950, 0.9)$, $(0.950, 1.0)$, $(0.950, 1.2)$, $(1.000, 0.95)$, $(1.000, 1.0)$, $(1.000, 1.1)$, $(1.000, 1.2)$, $(1.025, 1.4)$, $(1.025, 1.5)$, $(1.025, 1.6)$, $(1.050, 1.4)$, $(1.050, 1.5)$, $(1.050, 1.6)$.

Finally, the states $p = 5$, $q = 8$, $M = 2$, $\rho = 1.033$, $T = 0.5$.

Polymer Clusters Data plotted in Figure 2.3 are grouped in the following multiplets (M, ρ, T, q, p):

- Set A (blue): $(2, 1.086, 0.7, 7, 6)$, $(3, 1.086, 0.7, 7, 6)$, $(10, 1.086, 0.7, 7, 6)$, $(10, 1.033, 0.7, 8, 6)$
- Set B (black): $(2, 1.033, 0.7, 10, 6)$, $(3, 1.039, 0.7, 11, 6)$, $(3, 1.041, 0.7, 11, 6)$
- Set C (red): $(2, 1.033, 0.5, 10, 6)$, $(3, 1.056, 0.7, 12, 6)$, $(5, 1.033, 0.6, 12, 6)$, $(10, 1.056, 0.7, 12, 6)$
- Set D (green): $(3, 1.086, 0.7, 12, 6)$, $(5, 1.086, 0.7, 12, 6)$, $(10, 1.086, 0.7, 12, 6)$
- Set E:$(2, 1.0, 0.7, 12, 11)$, $(3, 1.1, 1.1, 15, 7)$
- Set F:$(3, 1.1, 0.65, 12, 6)$

Appendix B

The Rouse model

The Rouse model [32] is the simplest bead-spring model for flexible polymer chains [29, 53, 230]. It is usually applied to describe the long-time or large-scale polymer dynamics by neglecting the interactions between monomers which are distant along the chain, i.e. excluded volume, hydrodynamic interactions and chain entanglements are not considered. This model has been frequently applied to non-entangled chains in concentrated solutions. The model also serves in the description of the entangled chains: the tube model analyses the motion of the Rouse chain confined in a tube-like regime for calculating various kinds of dynamic properties [53]. Thus, the Rouse model is one of the most important models in the field of polymer dynamics.

In the Rouse model each chain is composed of $M_R - 1$ segments being modeled by M_R non-interacting beads, connected by entropic springs with force constant $\kappa = 3k_BT/a_R^2$, where a_R is the average size of the segment, i.e. the root mean square length of the spring, k_B is the Boltzmann constant, and T is the absolute temperature. No other interaction between the beads is present. The model considers a given chain and regards the surrounding ones as a uniform frictional medium for the focused chain. The segmental friction coefficient of the selected chain in this medium is denoted by ζ. The surrounding chains are depicted to exert on each bead of the selected chain also a fast-fluctuating random force to ensure proper equilibrium properties via the fluctuation-dissipation theorem.

The Rouse model has been tested by experiments [231–235] and numerical simulations [18, 19, 236–239]. Corrections for free-volume effects [240], intra- and intermolecular mean-force potentials [236] and uncrossability constraints [241] are also known.

The discrete Rouse model [242, 243] describes a single linear chain as a series of $M_R - 1$ segments being modeled by M_R non-interacting beads, connected by entropic springs in the presence of a highly damping gaussian environment. The Langevin equation for the inner beads ($2 \leq n \leq M_R - 1$) is :

$$\zeta \dot{\mathbf{r}}_n(t) = \frac{3k_BT}{a_R^2} \left[\mathbf{r}_{n-1}(t) - 2\mathbf{r}_n(t) + \mathbf{r}_{n+1}(t)\right] + \mathbf{f}_n(t) \tag{B.1}$$

and for the end beads ($n = 1, M_R$):

$$\zeta \dot{\mathbf{r}}_1(t) = \frac{3k_BT}{a_R^2}\left[\mathbf{r}_2(t) - \mathbf{r}_1(t)\right] + \mathbf{f}_1(t) \tag{B.2}$$

$$\zeta \dot{\mathbf{r}}_{M_R}(t) = \frac{3k_BT}{a_R^2}\left[\mathbf{r}_{M_R-1}(t) - \mathbf{r}_{M_R}(t)\right] + \mathbf{f}_{M_R}(t) \tag{B.3}$$

where $\mathbf{r}_n$ is the position vector of the n-th bead of the chain and the dot denotes a time derivative. The cartesian components α and β of the stochastic force $\mathbf{f}_n(t)$ are modeled as Gaussian white noise with zero average and correlations according to the fluctuation-dissipation theorem: $\langle f_{n\alpha}(t) f_{m\beta}(t')\rangle = 2\zeta k_B T \delta_{nm}\delta_{\alpha\beta}\delta(t-t')$ The set of eqs B.1 with $n = 1, \ldots, M_R$ are exactly solvable [243]. The solution, i.e. the position of the $n-$th bead $\mathbf{r}_n$, is conveniently expressed in terms of normal coordinates, the so-called Rouse modes $\mathbf{X}_p^R$ with $p = 0, \ldots, M_R - 1$, as:

$$\mathbf{r}_n(t) = \mathbf{X}_0^R(t) + 2\sum_{p=1}^{M_R-1} \mathbf{X}_p^R(t) \cos\left[\frac{(n-1/2)p\pi}{M_R}\right]. \tag{B.4}$$

The Rouse modes may be conversely written as:

$$\mathbf{X}_p^R(t) = \frac{1}{M_R}\sum_{n=1}^{M_R} \mathbf{r}_n(t) \cos\left[\frac{(n-1/2)p\pi}{M_R}\right] \tag{B.5}$$

The static cross-correlations between the Rouse modes vanish. In particular, for $p > 0$

$$\langle \mathbf{X}_p^R \cdot \mathbf{X}_q^R\rangle = \delta_{pq}\frac{a_R^2}{8M_R \sin^2(p\pi/2M_R)} \tag{B.6}$$

$$\cong \delta_{pq}\frac{M_R\, a_R^2}{2\pi^2 p^2}, \qquad p/M_R \ll 1 \tag{B.7}$$

For $p, q = 0$ one finds:

$$\langle |\mathbf{X}_0^R(t) - \mathbf{X}_0^R(0)|^2\rangle = 6\frac{k_BT}{M_R\zeta}t \tag{B.8}$$

which describes the diffusive motion of the center of mass $\mathbf{R}_{CM} = \mathbf{X}_0^R$. For $p > 0$, having defined the normalized self-correlation function of the p-th Rouse mode as:

$$\phi_p^R(t) = \frac{\langle \mathbf{X}_p^R(t)\cdot\mathbf{X}_p^R(0)\rangle}{\langle |\mathbf{X}_p^R|^2\rangle} \tag{B.9}$$

The Rouse model predicts the exponential decay $\phi_p^R(t) = \exp\left[-t/\tau_p\right]$ with characteristic time:

$$\tau_p = \frac{\zeta a_R^2}{12k_BT\sin^2(p\pi/2M_R)} \tag{B.10}$$

$$\cong \frac{\zeta a_R^2}{3\pi^2 k_BT}\frac{M_R^2}{p^2}, \qquad p/M_R \ll 1 \tag{B.11}$$

Appendix C

The shoving model

The starting idea of the shoving model is that, due to the strong intermolecular repulsion, rearrangement occurring at constant region volume requires very high energy. Because of this, it is more favorable that rearranging molecules spend some energy on shoving aside the surrounding molecules. Let us assume that the rearranging region is a sphere whose radius increases by Δr at the transition. If the surrounding liquid is regarded as an elastic solid on the short time scale of a flow event, the energy cost for the expansion is $A(\Delta r)^2$. The energy barrier is some function $f(\Delta r)$. Minimizing the total energy leads to $2A\Delta r + f'(\Delta r) = 0$. The ratio between the shoving work and the barrier is $\lambda = A(\Delta r)^2 / f(\Delta r) = -(1/2) d \ln f / d \ln \Delta r$. Due to strong repulsion, the logarithmic derivative of $f(\Delta r)$ is much larger than one, so the shoving work is dominant and the "inner" contribution to the activation energy may be ignored.

The shoving work can be calculated assuming that during a flow event the surrounding liquid behaves as an elastic isotropic solid. If V is the volume of the rearranging region and $\Delta V << V$. The activation energy is the elastic energy stored in the surroundings after the region volume has expanded to $V + \Delta V$. The strain tensor u_{ij} is defined

$$u_{ij} = \frac{1}{2} \left(\partial_i u_j + \partial_j u_i \right) \tag{C.1}$$

where u_k is the k-th component of the elastic displacement $\mathbf{u}$. For an isotropic solid the bulk and shear moduli K and G are defined via the relation between the stress tensor σ_{ij} and the strain tensor u_{ij}:

$$\sigma_{ij} = K u_{ll} \delta_{ij} + 2G \left(u_{ij} - \frac{1}{3} \delta_{ij} u_{ll} \right) \tag{C.2}$$

where the sum over repeated indices is implied. The equation for the static equilibrium is:

$$\partial_i \sigma_{ij} = 0 \tag{C.3}$$

The combination of eqs C.1, C.2 and C.3 leads to

$$\left(K + \frac{1}{3} G \right) \nabla \left(\nabla \cdot \mathbf{u} \right) + G \nabla^2 \mathbf{u} = 0 \tag{C.4}$$

For a purely radial displacement $\nabla \times \mathbf{u} = 0$ and thus, via a well known vector identity, $\nabla^2\mathbf{u} = \nabla(\nabla \cdot \mathbf{u})$. Substituting in eq C.4, one finds

$$\nabla(\nabla \cdot \mathbf{u}) = 0 \tag{C.5}$$

This leads to $\nabla \cdot \mathbf{u} = C_1$, where C_1 is a constant, and, by solving, the radial displacement $u_r = C_2 r^{-2} + C_1 r/3$ is found. As the latter term diverges as $r \to \infty$, then $C_1 = 0$ and $\nabla \cdot \mathbf{u} = 0$, i.e., there is no compression of the surroundings during the flow event.

If R is the radius of the region before the expansion and $\Delta R \ll R$ is the change in radius, then

$$u_r = \Delta R \frac{R^2}{r^2} \, (r > R) \tag{C.6}$$

In an elastic solid the density of energy is given by $(1/2)Ku_{ll}^2 + G(u_{ij} - (1/3)\delta_{ij}u_{ll})^2$. Since $u_{ll} = 0$, the energy density reduces to $Gu_{ij}u_{ij} = G(u_{rr}^2 + u_{\phi\phi}^2 + u_{\theta\theta}^2)$ (all mixed terms vanish because the displacement is purely radial). Substituting eq C.6 in the expression of the strain vector in polar coordinates, one get for the energy density $6G(\Delta R)^2 R^4 r^{-6}$. Thus, the elastic energy is

$$\int_R^\infty 6G(\Delta R)^2 R^4 r^{-6} \, (4\pi r^2) dr = 8\pi G(\Delta R)^2 R \tag{C.7}$$

One introduce the characteristic volume

$$V_c = \frac{2}{3}\frac{(\Delta V)^2}{V} \tag{C.8}$$

where $V = 4\pi R^3/3$ and $\Delta V = 4\pi R^2 \Delta R$. Then the activation energy is given by

$$\Delta E(T) = G_\infty(T) V_c \tag{C.9}$$

where the assumption $G \equiv G_\infty(T)$. For the relaxation time one have

$$\tau = \tau_0 \exp\left(\frac{G_\infty(T) V_c}{k_B T}\right) \tag{C.10}$$

When eq C.10 is compared to experiment, it is usually assumed that V_c is temperature independent.

Bibliography

[1] C. A. Angell. Perspective on the glass transition. *J. Phys. Chem. Solids*, 49:863, 1988.

[2] C. A. Angell, K. L. Ngai, G. B. McKenna, P. F. McMillan, and S.W.Martin. Relaxation in glassforming liquids and amorphous solids. *J. Appl. Phys.*, 88:3113–3157, 2000.

[3] P. G. Debenedetti and F. H. Stillinger. Supercooled liquids and the glass transition. *Nature*, 410:259–267, 2001.

[4] J. C. Dyre. The glass transition and elastic models of glass-forming liquids. *Rev. Mod. Phys.*, 78:953–972, 2006.

[5] A. Cavagna. Supercooled liquids for pedestrians. *Physics Reports*, 476:51 – 124, 2009.

[6] F. Sausset, G. Biroli, and J. Kurchan. Do solids flow? *J. Stat. Physics*, 140:718–727, 2010.

[7] J. Shao and C. A. Angell. Vibrational anharmonicity and the glass transition in strong and fragile vitreous polymorphs. In *Proc. XVIIth International Congress on Glass, Beijing*, volume 1, pages 311–320. Chinese Ceramic Societ, 1995.

[8] C.A. Angell. Relaxation in liquids, polymers and plastic crystals - strong/fragile patterns and problems. *J.Non-Crystalline Sol.*, 131-133:13–31, 1991.

[9] C. A. Angell. Formation of glasses from liquids and biopolymers. *Science*, 267:1924–1935, 1995.

[10] H. Bässler. Viscous flow in supercooled liquids analyzed in terms of transport theory for random media with energetic disorder. *Phys. Rev. Lett.*, 58:767–770, 1987.

[11] I. Avramov. Viscosity in disordered media. *J. Non-Cryst. Solids*, 351:3163 – 3173, 2005.

[12] Yael S. Elmatad, David Chandler, and Juan P. Garrahan. Corresponding states of structural glass formers. *The Journal of Physical Chemistry B*, 113:5563–5567, 2009.

[13] M. P. Allen and D. J. Tildesley. *Computer simulations of liquids*. Oxford university press, Clarendon, 1987.

[14] D. Frenkel and B. Smith. *Understanding Molecular Simulations*. Academic Press, 2002.

[15] W. Kob. Computer simulations of supercooled liquids and glasses. *J. Phys.: Condens. Matter*, 11:R85–R115, 1999.

[16] J. L. Barrat and M. L. Klein. Molecular dynamics simulations of supercooled liquids near the glass transition. *Annu. Rev. Phys. Chem.*, 42:23–53, 1991.

[17] L. J. Lewis and G. Wahnström. Molecular-dynamics study of supercooled *ortho* -terphenyl. *Phys. Rev. E*, 50:3865–3877, Nov 1994.

[18] J. Baschnagel and F. Varnik. Computer simulations of supercooled polymer melts in the bulk and in confined geometry. *J. Phys.: Condens. Matter*, 17:R851–R953, 2005.

[19] W. Paul and G. D. Smith. Structure and dynamics of amorphous polymers: computer simulations compared to experiment and theory. *Rep. Prog. Phys.*, 67:1117, 2004.

[20] S. Sastry, P. G. Debenedetti, and F. H. Stillinger. Statistical geometry of particle packings. ii. "weak spots" in liquids. *Phys. Rev. E*, 56:5533–5543, 1997.

[21] P. A. Netz, F. W. Starr, H. E. Stanley, and M. C. Barbosa. Static and dynamic properties of stretched water. *J. Chem. Phys.*, 115:344–348, 2001.

[22] J. Baschnagel and K. Binder. On the influence of hard walls on structural properties in polymer glass simulation. *Macromolecules*, 28:6808–6818, 1995.

[23] W. Gøtze. Recent tests of the mode-coupling theory for glassy dynamics. *J. Phys.: Condens. Matter*, 11:A1, 1999.

[24] W. Kob and H. C. Andersen. Scaling behavior in the β-relaxation regime of a supercooled lennard-jones mixture. *Phys. Rev. Lett.*, 73:1376–1379, 1994.

[25] L. Larini, A. Ottochian, C. De Michele, and D. Leporini. Universal scaling between structural relaxation and vibrational dynamics in glass-forming liquids and polymers. *Nature Physics*, 4:42–45, 2008.

[26] A. Ottochian, C. De Michele, and D. Leporini. Universal divergenceless scaling between structural relaxation and caged dynamics in glass-forming systems. *J. Chem. Phys.*, 131:224517, 2009.

[27] C. M. Roland, S. Hensel-Bielowka, M. Paluch, and R. Casalini. Supercooled dynamics of glass-forming liquids and polymers under hydrostatic pressure. *Rep. Prog. Phys.*, 68:1405, 2005.

[28] U. W. Gedde. *Polymer Physics*. Chapman and Hall, London, London, 1995.

[29] G. Strobl. *The Physics of Polymers*. Springer, New York, 1997.

[30] P.J.Flory. *Principles of Polymer Chemistr.* Cornell University Press, New York, 1953.

[31] P.-G.deGennes. *Scaling Concepts in Polymer Physics.* 1988.

[32] P. E. Rouse. A theory of the linear viscoelastic properties of dilute solutions of coiling polymers. *J. Chem. Phys.*, 21:1272, 1953.

[33] R. W. Hall and P. G. Wolynes. The aperiodic crystal picture and free energy barriers in glasses. *J. Chem. Phys.*, 86:2943–2948, 1987.

[34] U. Buchenau and R. Zorn. A relation between fast and slow motions in glassy and liquid selenium. *Europhys. Lett.*, 18:523–528, 1992.

[35] A. Widmer-Cooper and P. Harrowell. Predicting the long-time dynamic heterogeneity in a supercooled liquid on the basis of short-time heterogeneities. *Phys. Rev. Lett.*, 96:185701(4), 2006.

[36] S. Sastry. The relationship between fragility, configurational entropy and the potential energy landscape of glass-forming liquids. *Nature (London)*, 409:164–167, 2001.

[37] L.-M. Martinez and C. A. Angell. A thermodynamic connection to the fragility of glass-forming liquids. *Nature*, 410:663–667, 2001.

[38] K. L. Ngai. Why the fast relaxation in the picosecond to nanosecond time range can sense the glass transition. *Phil. Mag.*, 84:1341–1353, 2004.

[39] K. L. Ngai. Dynamic and thermodynamic properties of glass-forming substances. *J. Non-Cryst. Solids*, 275:7–51, 2000.

[40] T. Scopigno, G. Ruocco, F. Sette, and G. Monaco. Is the fragility of a liquid embedded in the properties of its glass? *Science*, 302:849–852, 2003.

[41] A. P. Sokolov, E. Rössler, A. Kisliuk, and D. Quitmann. Dynamics of strong and fragile glass formers: Differences and correlation with low-temperature properties. *Phys. Rev. Lett.*, 71:2062–2065, 1993.

[42] U. Buchenau and A. Wischnewski. Fragility and compressibility at the glass transition. *Phys. Rev. B*, 70:092201, 2004.

[43] V. N. Novikov and A. P. Sokolov. Poisson's ratio and the fragility of glass-forming liquids. *Nature*, 431:961–963, 2004.

[44] V. N. Novikov, Y. Ding, and A. P. Sokolov. Correlation of fragility of supercooled liquids with elastic properties of glasses. *Phys.Rev.E*, 71:061501, 2005.

[45] S. N. Yannopoulos and G. P. Johari. Poisson's ratio and liquid's fragility. *Nature*, 442:E7–E8, 2006.

[46] A. Ottochian and D. Leporini. Scaling between structural relaxation and caged dynamics in $ca_{0.4}k_{0.6}(no_3)_{1.4}$ and glycerol: free volume, time scales and implications for the pressure-energy correlations. *Philosophical Magazine*, 91:1786–1795, 2011.

[47] C. De Michele, E. Del Gado, and D. Leporini. Scaling between structural relaxation and particle caging in a model colloidal gel. *Soft Matter*, 7:4025–4031, 2011.

[48] A. Ottochian and D. Leporini. Universal scaling between structural relaxation and caged dynamics in glass-forming systems: Free volume and time scales. *J. Non-Cryst. Solids*, 357:298–301, 2011.

[49] J. P. Boon and S. Yip. *Molecular Hydrodynamics*. Dover Publications, New York, 1980.

[50] J. P. Hansen and I. R. McDonald. *Theory of Simple Liquids, 3rd Ed.* Academic Press, 2006.

[51] C. De Michele and D. Leporini. Viscous flow and jump dynamics in molecular supercooled liquids. i. translations. *Phys. Rev. E*, 63:036701, 2001.

[52] A. Barbieri, E. Campani, S. Capaccioli, and D. Leporini. Molecular dynamics study of the thermal and the density effects on the local and the large-scale motion of polymer melts: Scaling properties and dielectric relaxation. *J. Chem.Phys.*, 120:437–453, 2004.

[53] M. Doi and S. F. Edwards. *The Theory of Polymer Dynamics*. Clarendon Press, Oxford, 1988.

[54] M. Durand, H. Meyer, O. Benzerara, J. Baschnagel, and O. Vitrac. Molecular dynamics simulations of the chain dynamics in monodisperse oligomer melts and of the oligomer tracer diffusion in an entangled polymer matrix. *J. Chem. Phys.*, 132(19):194902, 2010.

[55] L. Bocquet, J. P. Hansen, and J. Piasecki. On the brownian-motion of a massive sphere suspended in a hard-sphere fluid. 2. molecular-dynamics estimates of the friction coefficient. *J. Stat. Physics*, 76:527–548, 1994.

[56] M. D. Ediger. Spatially heterogeneous dynamics in supercooled liquids. *Annu. Rev. Phys. Chem.*, 51:99–128, 2000.

[57] S. F. Swallen, P. A. Bonvallet, R. J. McMahon, and M. D. Ediger. Self-diffusion of *tris* - naphthylbenzene near the glass transition temperature. *Phys. Rev. Lett.*, 90:015901, 2003.

[58] R. Richert. Heterogeneous dynamics in liquids: fluctuations in space and time. *J. Phys.: Condens. Matter*, 14:R703–R738, 2002.

[59] T. Köddermann, R. Ludwig, and D. Paschek. On the validity of stokes–einstein and stokes–einstein–debye relations in ionic liquids and ionic-liquid mixtures. *ChemPhysChem*, 9:1851–1858, 2008.

[60] G. L. Pollack. Atomic test of the stokes-einstein law: Diffusion and solubility of xe. *Phys. Rev. A*, 23:2660–2663, 1981.

[61] G. Heuberger and H. Sillescu. Size dependence of tracer diffusion in supercooled liquids. *J. Phys. Chem.*, 100:15255–15260, 1996.

[62] M. T. Cicerone and M. D. Ediger. Enhanced translation of probe molecules in supercooled o-terphenyl: Signature of spatially heterogeneous dynamics? *J. Chem. Phys.*, 104:7210–7218, 1996.

[63] J.F. Douglas and D. Leporini. Obstruction model of the fractional stokes-einstein relation in glass-forming liquids. *J. Non-Cryst. Solids*, 235-237:137–141, 1998.

[64] F. Mallamace, C. Corsaro, H. E. Stanley, and S. H. Chen. The role of the dynamic crossover temperature and the arrest in glass-forming fluids. *Eur. Phys. J. E*, 34:94, 2011.

[65] B. Doliwa and A. Heuer. Cooperativity and spatial correlations near the glass transition: Computer simulation results for hard spheres and disks. *Phys. Rev. E*, 61(6):6898–6908, Jun 2000.

[66] Eric R Weeks, John C Crocker, and D A Weitz. Short-and long-range correlated motion observed in colloidal glasses and liquids. *J.Phys.:Condens. Matter*, 19(20):205131, 2007.

[67] Christoph Bennemann, Claudio Donati, Jorg Baschnagel, and Sharon C. Glotzer. Growing range of correlated motion in a polymer melt on cooling towards the glass transition. *Nature*, 399(6733):246–249, 05 1999.

[68] Claudio Donati, Sharon C. Glotzer, and Peter H. Poole. Growing spatial correlations of particle displacements in a simulated liquid on cooling toward the glass transition. *Phys. Rev. Lett.*, 82(25):5064–5067, Jun 1999.

[69] T. Narumi and M. Tokuyama. Simulation study of spatialâĂŽäìtemporal correlation functions in supercooled liquids. *Phil. Mag.*, 88(33-35):4169–4175, 2008.

[70] W. Kob, C. Donati, S. J. Plimpton, P. H. Poole, and S. C. Glotzer. Dynamical heterogeneities in a supercooled lennard-jones liquid. *Phys. Rev. Lett.*, 79:2827–2830, 1997.

[71] A. Ottochian, C. De Michele, and D. Leporini. Non-gaussian effects in the cage dynamics of polymers. *Philosophical Magazine*, 88:4057–4062, 2008.

[72] H. C. Longuet-Higgins and B. Widom. A rigid sphere model for the melting of argon. *Mol. Phys.*, 8:549–556, 1964.

[73] J. A. Barker and D. Henderson. Perturbation theory and equation of state for fluids. ii. a successful theory of liquids. *J. Chem. Phys.*, 47:4714–4721, 1967.

[74] B. Widom. Intermolecular forces and the nature of the liquid state. *Science*, 157:375–382, 1967.

[75] J. D. Weeks, D. Chandler, and H. C. Andersen. Role of repulsive forces in determining the equilibrium structure of simple liquids. *J. Chem. Phys.*, 54:5237–5247, 1971.

[76] J. A. Barker and D. Henderson. What is "liquid"? understanding the states of matter. *Rev. Mod. Phys.*, 48:587–671, 1976.

[77] D. Chandler, J. D. Weeks, and H. C. Andersen. Van der waals picture of liquids, solids, and phase transformations. *Science*, 220:787–794, 1983.

[78] M. Bishop, M. H. Kalos, and H. L. Frisch. The influence of attractions on the static and dynamic properties of simulated single and multichain systems. *J. Chem. Phys.*, 79:3500–3504, 1983.

[79] T. Young and H. C. Andersen. Tests of an approximate scaling principle for dynamics of classical fluids. *J. Phys. Chem. B*, 109:2985–2994, 2005.

[80] S. D. Bembenek and G. Szamel. The role of attractive interactions in self-diffusion. *J. Phys. Chem. B*, 104:10647–10652, 2000.

[81] J. Jonas. Nuclear magnetic resonance at high pressure. *Science*, 216:1179–1184, 1982.

[82] J. Kushick and B. J. Berne. Role of attractive forces in self-diffusion in dense lennard-jones fluids. *J. Chem. Phys.*, 59:3732–3736, 1973.

[83] D. Chandler. Equilibrium structure and molecular motion in liquids. *Acc. of Chem. Res.*, 7:246–251, 1974.

[84] L. Berthier and G. Tarjus. Nonperturbative effect of attractive forces in viscous liquids. *Phys. Rev. Lett.*, 103:170601, Oct 2009.

[85] L. Berthier and G. Tarjus. The role of attractive forces in viscous liquids. *J. Chem. Phys.*, 134:214503, 2011.

[86] S. Toxvaerd and J. C. Dyre. Role of the first coordination shell in determining the equilibrium structure and dynamics of simple liquids. *J. Chem. Phys.*, 135:134501, 2011.

[87] U. R. Pedersen, N. P. Bailey, T. B. Schrøder, and J. C. Dyre. Strong pressure-energy correlations in van der waals liquids. *Phys. Rev. Lett.*, 100:015701, 2008.

[88] U. R. Pedersen, T. Christensen, T. B. Schrøder, and J. C. Dyre. Feasibility of a single-parameter description of equilibrium viscous liquid dynamics. *Phys. Rev. E*, 77:011201, 2008.

[89] N. P. Bailey, U. R. Pedersen, N. Gnan, T. B. Schrøder, and J. C. Dyre. Pressure-energy correlations in liquids. i. results from computer simulations. *J. Chem. Phys.*, 129:184507, 2008.

[90] N. P. Bailey, U. R. Pedersen, N. Gnan, T. B. Schrøder, and J. C. Dyre. Pressure-energy correlations in liquids. ii. analysis and consequences. *J. Chem. Phys.*, 129:184508, 2008.

[91] T. B. Schrøder, N. P. Bailey, U. R. Pedersen, N. Gnan, and J. C. Dyre. Pressure-energy correlations in liquids. iii. statistical mechanics and thermodynamics of liquids with hidden scale invariance. *J. Chem. Phys.*, 131:234503, 2009.

[92] N. Gnan, T. B. Schroder, U. R. Pedersen, N. P. Bailey, and J. C. Dyre. Pressure-energy correlations in liquids. iv. "isomorphs" in liquid phase diagrams. *J. Chem. Phys.*, 131:234504, 2009.

[93] T. B. Schrøder, N. Gnan, U. R. Pedersen, N. P. Bailey, and Jeppe C. Dyre. Pressure-energy correlations in liquids. v. isomorphs in generalized lennard-jones systems. *J. Chem. Phys.*, 134:164505, 2011.

[94] U. R. Pedersen, N. Gnan, N. P. Bailey, T. B. Schrøder, and J. C. Dyre. Strongly correlating liquids and their isomorphs. *J. Non-Cryst. Solids*, 357:320 – 328, 2011.

[95] U. R. Pedersen, T. B. Schrøder, and J. C. Dyre. Repulsive reference potential reproducing the dynamics of a liquid with attractions. *Phys. Rev. Lett.*, 105:157801, Oct 2010.

[96] T. S. Ingebrigtsen, T. B. Schrøder, and J. C. Dyre. Isomorphs in model molecular liquids. *J. Phys. Chem. B*, 116:1018–1034, 2012.

[97] J. D. Weeks, R. L. B. Selinger, and J. Q. Broughton. Self-consistent treatment of repulsive and attractive forces in nonuniform liquids. *Phys. Rev. Lett.*, 75:2694–2697, 1995.

[98] F.W. Starr, S. Sastry, J. F. Douglas, and S. Glotzer. What do we learn from the local geometry of glass-forming liquids? *Phys. Rev. Lett.*, 89:125501, 2002.

[99] T. S. Jain and J. J. de Pablo. Role of local structure on motions on the potential energy landscape for a model supercooled polymer. *J. Chem. Phys.*, 122:174515, 2005.

[100] R. A. Riggleman, J. F. Douglas, and J. J. de Pablo. Tuning polymer melt fragility with antiplasticizer additives. *J. Chem. Phys.*, 126:234903, 2007.

[101] G. J. Papakonstantopoulos, R. A. Riggleman, J.-L. Barrat, and J. J. de Pablo. Molecular plasticity of polymeric glasses in the elastic regime. *Phys. Rev. E*, 77:041502, 2008.

[102] N. Tokita, M. Hirabayashi, C. Azuma, and T. Dotera. Voronoi space division of a polymer: Topological effects, free volume, and surface end segregation. *J. Chem. Phys.*, 120:496–505, 2004.

[103] A. A. Veldhorst, L. Bøhling, J. C. Dyre, and T. B. Schrøder. Isomorphs in the phase diagram of a model liquid without inverse power law repulsion. *Eur. Phys. J. B*, 85:21, 2012.

[104] D. Coslovich and C.M. Roland. Heterogeneous slow dynamics and the interaction potential of glass-forming liquids. *J. Non-Cryst. Solids*, 357:397 – 400, 2011.

[105] A. S. Clarke and H. Jonsson. Structural changes accompanying densification of random hard-sphere packings. *Phys. Rev. E*, 47:3975–3984, 1993.

[106] Z. Shi, P. G. Debenedetti, F. H. Stillinger, and P. Ginart. Structure, dynamics, and thermodynamics of a family of potentials with tunable softness. *J. Chem. Phys.*, 135:084513, 2011.

[107] J.-P. Ryckaert, G. Ciccotti, and H. J.C Berendsen. Numerical integration of the cartesian equations of motion of a system with constraints: molecular dynamics of n-alkanes. *J. Comp. Phys.*, 23:327 – 341, 1977.

[108] D. V. Hinkley. On the ratio of two correlated normal random variables. *Biometrika*, 56:635–639, 1969.

[109] K. Mpoukouvalas and G. Floudas. Phase diagram of poly(methyl-*p*-tolyl-siloxane): A temperature- and pressure-dependent dielectric spectroscopy investigation. *Phys. Rev. E*, 68:031801, 2003.

[110] M. Paluch, R. Casalini, and C. M. Roland. Relative contributions of thermal energy and free volume to the temperature dependence of structural relaxation in fragile glass-forming liquids. *Phys. Rev. B*, 66:092202, 2002.

[111] M. L. Ferrer, C. L., B. G. Demirjian, D. Kivelson, C. Alba-Simionesco, and G. Tarjus. Supercooled liquids and the glass transition: Temperature as the control variable. *J. Chem. Phys.*, 109:8010–8015, 1998.

[112] A. Tølle. Neutron scattering studies of the model glass former ortho -terphenyl. *Rep. Prog. Phys.*, 64:1473, 2001.

[113] C. Dreyfus, A. Aouadi, J. Gapinski, M. Matos-Lopes, W. Steffen, A. Patkowski, and R. M. Pick. Temperature and pressure study of brillouin transverse modes in the organic glass-forming liquid orthoterphenyl. *Phys. Rev. E*, 68:011204, 2003.

[114] S. Pawlus, R. Casalini, C. M. Roland, M. Paluch, S. J. Rzoska, and J. Ziolo. Temperature and volume effects on the change of dynamics in propylene carbonate. *Phys. Rev. E*, 70:061501, 2004.

[115] R. Casalini and C. M. Roland. Thermodynamical scaling of the glass transition dynamics. *Phys. Rev. E*, 69:062501, 2004.

[116] C. Alba-Simionesco, A. Cailliaux, A. Alegría, and G. Tarjus. Scaling out the density dependence of the Îś relaxation in glass-forming polymers. *EPL*, 68:58, 2004.

[117] C. Dreyfus, A. Le Grand, J. Gapinski, W. Steffen, and A. Patkowski. Scaling the α-relaxation time of supercooled fragile organic liquids. *Eur. Phys. J. B*, 42:309–319, 2004.

[118] A. Reiser, G. Kasper, and S. Hunklinger. Pressure-induced isothermal glass transition of small organic molecules. *Phys. Rev. B*, 72:094204, 2005.

[119] R. Casalini and C. M. Roland. Scaling of the supercooled dynamics and its relation to the pressure dependences of the dynamic crossover and the fragility of glass formers. *Phys. Rev. B*, 71:014210, 2005.

[120] C. M. Roland, S. Bair, and R. Casalini. Thermodynamic scaling of the viscosity of van der waals, h-bonded, and ionic liquids. *J. Chem. Phys.*, 125:124508, 2006.

[121] E. R. Lopez, A. S. Pensado, M. J. P. Comunas, A. A. H. Padua, J. Fernandez, and K. R. Harris. Density scaling of the transport properties of molecular and ionic liquids. *J. Chem. Phys.*, 134:144507, 2011.

[122] M. Paluch, S. Haracz, A. Grzybowski, M. Mierzwa, J. Pionteck, A. Rivera-Calzada, and C. Leon. A relationship between intermolecular potential, thermodynamics, and dynamic scaling for a supercooled ionic liquid. *J. Phys. Chem. Lett.*, 1:987–992, 2010.

[123] C. M. Roland, R. Casalini, R. Bergman, and J. Mattsson. Role of hydrogen bonds in the supercooled dynamics of glass-forming liquids at high pressures. *Phys. Rev. B*, 77:012201, 2008.

[124] W. G. Hoover and M. Rossj. Statistical theories of melting. *Contemporary Physics*, 12:339–356, 1971.

[125] D. Coslovich and C. M. Roland. Thermodynamic scaling of diffusion in supercooled lennard-jones liquids. *J. Phys. Chem. B*, 112:1329–1332, 2008.

[126] D. Coslovich and C. M. Roland. Pressure-energy correlations and thermodynamic scaling in viscous lennard-jones liquids. *J. Chem. Phys.*, 130:014508, 2009.

[127] T. B. Schrøder, U. R. Pedersen, N. P. Bailey, S. Toxvaerd, and J. C. Dyre. Hidden scale invariance in molecular van der waals liquids: A simulation study. *Phys. Rev. E*, 80:041502, 2009.

[128] S. Sengupta, F. Vasconcelos, F. Affouard, and S. Sastry. Dependence of the fragility of a glass former on the softness of interparticle interactions. *J. Chem. Phys.*, 135:194503, 2011.

[129] G. Tarjus, D. Kivelson, S. Mossa, and C. Alba-Simionesco. Disentangling density and temperature effects in the viscous slowing down of glassforming liquids. *J. Chem. Phys.*, 120:6135–6141, 2004.

[130] R. Casalini, U. Mohanty, and C. M. Roland. Thermodynamic interpretation of the scaling of the dynamics of supercooled liquids. *J. Chem. Phys.*, 125:014505, 2006.

[131] R. Casalini and C.M. Roland. An equation for the description of volume and temperature dependences of the dynamics of supercooled liquids and polymer melts. *J. Non-Cryst. Solids*, 353:3936 – 3939, 2007.

[132] I. Avramov. Viscosity in disordered media. *J. Non-Cryst. Solids*, 351:3163 – 3173, 2005.

[133] H. Zhang, D. J. Srolovitz, J. F. Douglas, and J. A. Warren. Grain boundaries exhibit the dynamics of glass-forming liquids. *Proc. Natl. Acad. Sci.*, 106:7735–7740, 2009.

[134] M. C. C. Ribeiro, T. Scopigno, and G. Ruocco. Computer simulation study of thermodynamic scaling of dynamics of 2ca(no[sub 3])[sub 2] [center-dot] 3kno[sub 3]. *J. Chem. Phys.*, 135:164510, 2011.

[135] D. Fragiadakis and C. M. Roland. On the density scaling of liquid dynamics. *J. Chem. Phys.*, 134:044504, 2011.

[136] R. Casalini, C. M. Roland, and S. Capaccioli. Effect of chain length on fragility and thermodynamic scaling of the local segmental dynamics in poly(methylmethacrylate). *J. Chem. Phys.*, 126:184903, 2007.

[137] R. Casalini and C. M. Roland. Scaling of the segmental relaxation times of polymers and its relation to the thermal expansivity. *Coll. Pol. & Science*, 283:107–110, 2004.

[138] J. Budzien, J. D. McCoy, and D. B. Adolf. General relationships between the mobility of a chain fluid and various computed scalar metrics. *J. Chem. Phys.*, 121:10291–10298, 2004.

[139] W. Doster, S. Cusack, and W. Petry. Dynamical transition of myoglobin revealed by inelastic neutron scattering. *Nature*, 337(754), 1989.

[140] G. Zaccai. How soft is a protein? a protein dynamics force constant measured by neutron scattering. *Science*, 288:1604–1607, 2000.

[141] M. Wyart. Correlations between vibrational entropy and dynamics in liquids. *Phys. Rev. Lett.*, 104:095901, 2010.

[142] A. Heuer. Exploring the potential energy landscape of glass-forming systems: from inherent structures via metabasins to macroscopic transport. *J. Phys.: Condens. Matter*, 20:373101, 2008.

[143] H. Fan, C. Hartshorn, T. Buchheit, D. Tallant, R. Assink, R. Simpson, D. J. Kissel, D. J. Lacks, S. Torquato, and C. J. Brinker. Modulus–density scaling behaviour and framework architecture of nanoporous self-assembled silicas. *Nat. Mat.*, 6:418, 2007.

[144] D. S. Corti, P. G. Debenedetti, S. Sastry, and F. H. Stillinger. Constraints, metastability, and inherent structures in liquids. *Phys. Rev. E*, 55:5522, 1997.

[145] S. Sastry, P. G. Debenedetti, and F. H. Stillinger. Statistical geometry of particle packings. ii. "weak spots" in liquids. *Phys. Rev. E*, 56:5533, 1997.

[146] D. Gundermann, U. R. Pedersen, T. Hecksher, N. P. Bailey, B. Jakobsen, T. Christensen, N. B. Olsen, T. B. Schroder, D. Fragiadakis, R. Casalini, M. C. Roland, J. C. Dyre, and K. Niss. Predicting the density-scaling exponent of a glass-forming liquid from prigogine-defay ratio measurements. *Nat Phys*, 7:816–821, 2011.

[147] S. Capaccioli. Personal communication.

[148] C. M. Roland and R. Casalini. Comment on: "disentangling density and temperature effects in the viscous slowing down of glass forming liquids" [j. chem. phys. [bold 120], 6135 (2004)]. *J. Chem. Phys.*, 121:11503–11504, 2004.

[149] C. M. Roland and R. Casalini. Dynamics of poly(cyclohexyl methacrylate):âĂĽ neat and in blends with poly(Îś-methylstyrene). *Macromolecules*, 40:3631–3639, 2007.

[150] C. M. Roland, M. J. Schroeder abd J. J. Fontanella, and K. L. Ngai. Evolution of the dynamics in 1, 4-polyisoprene from a nearly constant loss to a johari-goldstein β-relaxation to the α-relaxation. *Macromolecules*, 37:2630–2635, 2004.

[151] M. Paluch, C. M. Roland, and S. Pawlus. Temperature and pressure dependence of the α-relaxation in polymethylphenylsiloxane. *J. Chem. Phys.*, 116:10932, 2002.

[152] M. Paluch, S. Pawlus, and C. M. Roland. Pressure and temperature dependence of the α-relaxation in poly(methyltolylsiloxane). *Macromolecules*, 35:7338–7342, 2002.

[153] R. Casalini and C. M. Roland. Temperature and density effects on the local segmental and global chain dynamics of poly(oxybutylene). *Macromolecules*, 38(5):1779–1788, 2005.

[154] C. M. Roland, T. Psurek, S. Pawlus, and M. Paluch. Segmental- and normal-mode dielectric relaxation of poly(propylene glycol) under pressure. *J. Polym. Sci., Part B: Polym. Phys.*, 41:3047–3052, 2003.

[155] C. M. Roland and R. Casalini. Temperature and volume effects on local segmental relaxation in poly(vinyl acetate). *Macromolecules*, 36:1361–1367, 2003.

[156] R. Casalini and C. M. Roland. Dynamic properties of polyvinylmethylether near the glass transition. *J. Chem. Phys.*, 119:4052–4059, 2003.

[157] K. Kaminski, S. Maslanka, J. Ziolo, M. Paluch, K. J. McGrath, and C. M. Roland. Dielectric relaxation of α-tocopherol acetate (vitamin e). *Phys. Rev. E*, 75:011903, 2007.

[158] M. H. Cohen and D. Turnbull. Molecular transport in liquids and glasses. *J. Chem. Phys.*, 31:1164–1169, 1959.

[159] G. S. Grest and M. H. Cohen. Liquids, glasses, and the glass transition: A free-volume approach. *Adv. Chem. Phys.*, 48:455–525, 1981.

[160] J. H. Gibbs and E. A. DiMarzio. Nature of the glass transition and the glassy state. *J. Chem. Phys.*, 28:373–383, 1958.

[161] G. Adam and J. H. Gibbs. On the temperature dependence of cooperative relaxation properties in glass-forming liquids. *J. Chem. Phys.*, 43:139–146, 1965.

[162] T. R. Kirkpatrick, D. Thirumalai, and P. G. Wolynes. Scaling concepts for the dynamics of viscous liquids near an ideal glassy state. *Phys. Rev. A*, 40:1045–1054, 1989.

[163] X. Xia and P. G. Wolynes. Fragilities of liquids predicted from the random first order transition theory of glasses. *Proc. Natl. Acad. Sci.*, 97:2990–2994, 2000.

[164] G. Tarjus, S. A. Kivelson, Z. Nussinov, and P. Viot. The frustration-based approach of supercooled liquids and the glass transition: a review and critical assessment. *J. Phys.: Condens. Matter*, 17:R1143, 2005.

[165] W. Gøtze and L. Sjogren. Relaxation processes in supercooled liquids. *Rep. Prog. Phys.*, 55:241, 1992.

[166] S. P. Das. Mode-coupling theory and the glass transition in supercooled liquids. *Rev. Mod. Phys.*, 76:785–851, 2004.

[167] J. P. Garrahan and D. Chandler. Geometrical explanation and scaling of dynamical heterogeneities in glass forming systems. *Phys. Rev. Lett.*, 89:035704, 2002.

[168] F. Ritort and P. Sollich. Glassy dynamics of kinetically constrained models. *Adv. in Physics*, 52:219, 2003.

[169] A. Tobolsky, R. E. Powell, and H. Eyring. Elastic-viscous properties of matter. In R. E. Burk and O. Grummit, editors, *Frontiers in Chemistry*, volume 1, pages 125–190, New York, 1943. Interscience.

[170] H. A. Kramers. Brownian motion in a field of force and the diffusion model of chemical reactions. *Physica*, 7:284 – 304, 1940.

[171] S. V. Nemilov. Kinetics of elementary processes in the condensed state. ii. shear relaxation and the equation of state for solids. *Russ. J. Phys. Chem.*, 42:726–729, 1968.

[172] H. Eyring. Viscosity, plasticity, and diffusion as examples of absolute reaction rates. *J. Chem. Phys.*, 4:283–291, 1936.

[173] S. Dushman. Theory of unimolecular reaction velocities. *Journal of the Franklin Institute*, 189:515 – 518, 1920.

[174] J. C. Dyre, N. B. Olsen, and T. Christensen. Local elastic expansion model for viscous-flow activation energies of glass-forming molecular liquids. *Phys. Rev. B*, 53:2171–2174, 1996.

[175] J. C. Dyre. Source of non-arrhenius average relaxation time in glass-forming liquids. *J. Non-Cryst. Solids*, 235:142 – 149, 1998.

[176] B. Zhang, H. Y. Bai, R. J. Wang, Y. Wu, and W. H. Wang. Shear modulus as a dominant parameter in glass transitions: Ultrasonic measurement of the temperature dependence of elastic properties of glasses. *Phys. Rev. B*, 76(1):012201, Jul 2007.

[177] J. Mattsson, H. M. Wyss, A. Fernandez-Nieves, K. Miyazaki, Z. Hu, D. R. Reichman, and D. A. Weitz. Soft colloids make strong glasses. *Nature (London)*, 462:83–86, 2009.

[178] D. H. Torchinsky, J. A. Johnson, and K. A. Nelson. A direct test of the correlation between elastic parameters and fragility of ten glass formers and their relationship to elastic models of the glass transition. *J. Chem. Phys.*, 130:064502, 2009.

[179] M. C. C. Ribeiro. The shoving model for the glass-former $LiCl \cdot 6H_2O$: A molecular dynamics simulation study. *Journal of Non-Crystalline Solids*, 355:1659 – 1662, 2009.

[180] V. A. Khonik, Yu. P. Mitrofanov, S. A. Lyakhov, A. N. Vasiliev, S. V. Khonik, and D. A. Khoviv. Relationship between the shear modulus g , activation energy, and shear viscosity η in metallic glasses below and above t_g : Direct in situ measurements of g and η. *Phys. Rev. B*, 79(13):132204, Apr 2009.

[181] Ben Xu and Gregory B. McKenna. Evaluation of the dyre shoving model using dynamic data near the glass temperature. *J. Chem. Phys.*, 134(12):124902, 2011.

[182] M. L. Lind, G. Duan, and W. L. Johnson. Isoconfigurational elastic constants and liquid fragility of a bulk metallic glass forming alloy. *Phys. Rev. Lett.*, 97:015501, 2006.

[183] M. D. Demetriou, J. S. Harmon, M. Tao, G. Duan, K. Samwer, and W. L. Johnson. Cooperative shear model for the rheology of glass-forming metallic liquids. *Phys. Rev. Lett.*, 97:065502, 2006.

[184] S.V. Khonik, A.V. Granato, D. M. Joncich, A. Pompe, and V. A. Khonik. Evidence of distributed interstitialcy-like relaxation of the shear modulus due to structural relaxation of metallic glasses. *Phys. Rev. Lett.*, 100:065501, 2008.

[185] Yu. P. Mitrofanov, V. A. Khonik, A. V. Granato, D. M. Joncich, and S. V. Khonik. Relaxation of the shear modulus of a metallic glass near the glass transition. *J. Appl. Phys.*, 109:073518, 2011.

[186] J. Yang and K. S. Schweizer. Glassy dynamics and mechanical response in dense fluids of soft repulsive spheres. ii. shear modulus, relaxation-elasticity connections, and rheology. *J.Chem.Phys.*, 134:204909, 2011.

[187] U. Buchenau. An asymmetry model for the highly viscous flow. *J. Chem. Phys.*, 131(7):074501, 2009.

[188] U. Buchenau. A thermodynamic treatment of the glass transition. arXiv:1203.3555v2.

[189] R. Zwanzig and R.D. Mountain. High-frequency elastic moduli of simple fluids. *J. Chem. Phys.*, 43:4464 – 4471, 1965.

[190] S. R. Williams. Broken-ergodicity and the emergence of solid behaviour in amorphous materials. *J. Chem. Phys.*, 135:131102, 2011.

[191] M. Allen. Atomic and molecular representations of molecular hydrodynamic variables. *Mol. Phys.*, 52:705–716, 1984.

[192] D. N. Perera and P. Harrowell. Relaxation dynamics and their spatial distribution in a two-dimensional glass-forming mixture. *J. Chem. Phys.*, 111:5441–5454, 1999.

[193] H. Yoshino and M. Mézard. Emergence of rigidity at the structural glass transition: A first-principles computation. *Phys. Rev. Lett.*, 105:015504, 2010.

[194] S. Suchira, S. K. Kumar, and P. Keblinski. Analysis of uncertainties in polymer viscoelastic properties obtained from equilibrium computer simulations. *J. Chem. Phys.*, 124:144909, 2006.

[195] M. Vladkov and J.-L. Barrat. Linear and nonlinear viscoelasticity of a model unentangled polymer melt: Molecular dynamics and rouse modes analysis. *Macromol. Theory Simul.*, 15:252–262, 2006.

[196] D. C. Wallace. *Thermodynamics of Crystals*. Wiley, New York, 1972.

[197] K. Yoshimoto, T. S. Jain, K. Van Workum, P. F. Nealey, and J. J. de Pablo. Mechanical heterogeneities in model polymer glasses at small length scales. *Phys. Rev. Lett.*, 93:175501, 2004.

[198] C. E. Maloney and A. Lemaître. Amorphous systems in athermal, quasistatic shear. *Phys. Rev. E*, 74:016118, 2006.

[199] M Tsamados, A. Tanguy, C. Goldenberg, and J.-L. Barrat. Local elasticity map and plasticity in a model lennard-jones glass. *Phys. Rev. E*, 80:026112, 2009.

[200] A. J. C. Ladd, W. E. Alley, and B. J. Alder. Structural relaxation in dense hard-sphere fluids. *J. Stat. Physics*, 48:1147–1156, 1987.

[201] T. B. Schrøder, S. Sastry, J. C. Dyre, and S. C. Glotzer. Crossover to potential energy landscape dominated dynamics in a model glass-forming liquid. *J. Chem. Phys.*, 112:9834, 2000.

[202] T. Geszti. Pre-vitrification by viscosity feedback. *J.Phys.C: Solid State Phys.*, 16:5805, 1983.

[203] U. Balucani, R. Vallauri, and T. Gaskell. Stress autocorrelation function in liquid rubidium. *Phys. Rev. A*, 37:3386–3392, 1988.

[204] R. A. LaViolette and F. H. Stillinger. Multidimensional geometric aspects of the solid-liquid transition in simple substances. *J. Chem. Phys.*, 83:4079–4085, 1985.

[205] G. A. Appignanesi, J. A. RodrÄśguez Fris, R. A. Montani, and W. Kob. Democratic particle motion for metabasin transitions in simple glass formers. *Phys. Rev. Lett.*, 96:057801, 2006.

[206] J. D. Ferry, L. D. Jr. Grandine, and E. R. Fitzgerald. The relaxation distribution function of polyisobutylene in the transition from rubber-like to glass-like behavior. *J. Appl. Phys.*, 24:911–916, 1953.

[207] R. H. Doremus. Viscosity of silica. *J. Appl. Phys.*, 92:7619–7629, 2002.

[208] A. Polian, D. Vo-Thanh, and P. Richet. Elastic properties of $a - SiO_2$ up to 2300k from brillouin scattering measurements. *Europhys. Lett.*, 57:375–381, 2002.

[209] K. M. Bernatz, I. Echeverría, S. L. Simon, and D. J. Plazek. Viscoelastic properties of boron dioxide. *J. Non-Cryst. Solids*, 289:9–16, 2001.

[210] M. Grimsditch, R. Bhadra, and L.M. Torell. Shear waves through the glass-liquid transformation. *Phys. Rev. Lett.*, 62:2616–2619, 1989.

[211] H. Z. Cummins, J. Hernandez, W. M. Du, and G. Li. Comment on "anomalies in the scaling of the dielectric α-relaxation". *Phys. Rev. Lett.*, 73:2935–2935, 1994.

[212] F. Scarponi, L. Comez, D. Fioretto, and L. Palmieri. Brillouin light scattering from transverse and longitudinal acoustic waves in glycerol. *Phys. Rev. B*, 70:054203, 2004.

[213] A. J. Barlow, J. Lamb, A. J. Matheson, P. R. K. L. Padmini, and J. Richter. Viscous behaviour of supercooled liquids. *Proc. R. Soc. London Ser. A*, 292:322–342, 1966.

[214] A. J. Barlow, J. Lamb, A. J. Matheson, P. R. K. L. Padmini, and J. Richter. Viscoelastic relaxation of supercooled liquids. i. *Proc. R. Soc. London Ser. A*, 298:467–480, 1967.

[215] C. Dreyfus, A. Aouadi, J. Gapinski, M. Matos-Lopes, W. Steffen, A. Patkowski, and R. M. Pick. Temperature and pressure study of brillouin transverse modes in the organic glass-forming liquid orthoterphenyl. *Phys. Rev. E*, 68:011204, 2003.

[216] V. F. Kozhevnikov, W. B. Payne, J. K. Olson, A. Allen, and P.C. Taylor. Sound velocity in liquid and glassy selenium. *J. Non-Cryst. Solids*, 353:3254–3259, 2007.

[217] H. Shintani and H. Tanaka. Frustration on the way to crystallization in glass. *Nat Phys*, 2:200–206, 2006.

[218] C. Patrick Royall, S. R. Williams, T. Ohtsuka, and H. Tanaka. Direct observation of a local structural mechanism for dynamic arrest. *Nat Mater*, 7:556–561, 2008.

[219] M. Asai, M. Shibayama, and Y. Koike. Common origin of dynamics heterogeneity and cooperatively rearranging region in polymer melts. *Macromolecules*, 44:6615–6624, 2011.

[220] U. Buchenau, Yu. M. Galperin, V. L. Gurevich, D. A. Parshin, M. A. Ramos, and H. R. Schober. Interaction of soft modes and sound waves in glasses. *Phys. Rev. B*, 46:2798–2808, 1992.

[221] J. C. Dyre and N. B. Olsen. Landscape equivalent of the shoving model. *Phys. Rev. E*, 69:042501, 2004.

[222] H. C. Andersen. Molecular dynamics simulations at constant pressure and/or temperature. *J. Chem. Phys.*, 72:2384–2393, 1980.

[223] S. Nosé. A unified formulation of the constant temperature molecular dynamics methods. *J. Chem. Phys.*, 81:511–519, 1984.

[224] M. E. Tuckerman, B. J. Berne, and G. J. Martyna. Reversible multiple time scale molecular dynamics. *J. Chem. Phys.*, 97:1990–2001, 1992.

[225] H. F. Trotter. On the product of semi-groups of operators. *Proc. Am. Math. Soc.*, 10:545–551, 1959.

[226] M. E. Tuckerman, B. J. Berne, and G. J. Martyna. Molecular dynamics algorithm for multiple time scales: Systems with long range forces. *J. Chem. Phys.*, 94:6811–6815, 1991.

[227] F. H. Stillinger. A topographic view of supercooled liquids and glass formation. *Science*, 267:1935–1939, 1995.

[228] W. H. Press, S. A. Teukolsky, W. T. Vetterling, and B. P. Flannery. *Numerical Recipes in C*. Cambridge University Press, 1992.

[229] C. Chakravarty, P. G. Debenedetti, and F. H. Stillinger. Generating inherent structures of liquids: Comparison of local minimization algorithms. *J. Chem. Phys.*, 123:206101, 2005.

[230] J. D. Ferry. *Viscoelastic Properties of Polymers*. Wiley, New York, 1980.

[231] T. P. Lodge, N. A. Rotstein, and S. Prager. Dynamics of entangled polymer liquids: Do linear chains reptate. *Adv. Chem. Phys.*, 79:1, 1990.

[232] W. Paul, G. D. Smith, D. Y. Yoon, B. Farago, S. Rathgeber, A. Zirkel, and D. Richter L. Willner. Chain motion in an unentangled polyethylene melt: A critical test of the rouse model by molecular dynamics simulations and neutron spin echo spectroscopy. *Phys. Rev. Lett.*, 80:2346, 1998.

[233] G. D. Smith, W. Paul Paul, M. Monkenbusch, and D. Richter. On the non-gaussianity of chain motion in unentangled polymer melts. *J. Chem. Phys.*, 114:4285–4288, 2001.

[234] M. Doxastakis, D. N. Theodorou, G. Fytas, F. Kremer, and R. Faller. Chain and local dynamics of polyisoprene as probed by experiments and computer simulations. *J. Chem. Phys.*, 119:6883, 2003.

[235] D. S. Pearson, L. J. Fetters, W. W. Greassley, G. Ver Strate, and E. von Meerwall. Viscosity and self-diffusion coefficent of hydrogenated polybutadine. *Macromolecules*, 27:711, 1994.

[236] M. Guenza. Cooperative dynamics in unentangled polymer fluids. *Phys. Rev. Lett*, 88:025901, 2002.

[237] K. Binder, J. Baschnagel, and W. Paul. Glass transition of polymer melts: test of theoretical concepts by computer simulation. *Progr. Polymer Sci.*, 28(1):115 – 172, 2003.

[238] J. Bennemann, J. Baschnagel, W. Paul, and K. Binder. Molecular-dynamics simulation of a glassy polymer melt: Rouse model and cage effect. *Comput. Theor. Polym. Sci.*, 9:217, 1999.

[239] C. Bennemann, W. Paul, J. Baschnagel, and K. Binder. Investigating the influence of different thermodynamic paths on the structural relaxation in a glass-forming polymer melt. *J. Phys.: Condens. Matter*, 11(10):2179–2192, 1999.

[240] V. A. Harmandaris, M. Doxastakis, V. G. Mavrantzas, and D. N. Theodorou. Detailed molecular dynamics simulation of the self-diffusion of n-alkane and cis-1,4 polyisoprene oligomer melts. *J. Chem. Phys.*, 116(1):436–446, 2002.

[241] J. T. Padding and W. J. Briels. Uncrossability constraints in mesoscopic polymer melt simulations: Non-rouse behavior of $C_{120}H_{242}$. *J. Chem. Phys.*, 115:2846–2859, 2001.

[242] P. H. Verdier. Monte carlo studies of lattice-model polymer chains. I. correlation functions in the statistical-bead model. *J. Chem. Phys.*, 45:2118, 1966.

[243] Y.-H. Lin. *Polymer Viscoelasticity*. World Scientific Publishing Co. Pte. Ltd, Singapore, 2003.

Now I wish to conclude by thanking all the people who made it possible for me to reach this point.
First I want to thank my supervisor prof. Leporini for his important support and guidance throughout this work.
Special thanks to Dr. Simone Capaccioli for the several stimulating discussions.
I warmly thank Alistar Ottochian for his valuable advice and help. Furthermore I want to thank Sebastiano Bernini for his company and help during the last year.
I gratefully thank Maurizio Davini, Federico Quaglierini, Andrea Valassina and Roberta Amaranti for the computational resources.
Thanks to prof. Pegoraro, prof. Foffi, prof. Monaco, prof. Rolla, Dr. Cristiano De Michele, Francesco Varrato and Paolo Pancani.
Thanks to Giulia and Silvia, many things would not be possible for me without your love and support.
Thanks to my father Angelo and my brother Alessandro, to my family, to friends and to all those people who supported me during this time.

Francesco
Pisa, May 2012